Theory of Momentum-Resolved Crystal Excitations in the Electron Microscope

Andrew W. Rossi

A dissertation submitted in partial fulfillment of the
requirements for the degree of

Doctor of Philosophy

University of Washington

2026

Reading Committee:

Prof. David J. Masiello, Chair

Prof. David S. Ginger

Prof. Daniel R. Gamelin

Program Authorized to Offer Degree:
Department of Chemistry

University of Washington

Abstract

Theory of Momentum-Resolved Crystal Excitations in the Electron Microscope

Andrew W. Rossi

Chair of the Supervisory Committee:
Prof. David J. Masiello
Department of Chemistry

As atomic and nanoscale materials continue to advance and reveal novel physical properties, the development of reliable and precise characterization techniques has become increasingly crucial. Motivated by recent experimental advances in electron energy loss spectroscopy (EELS) performed inside electron microscopes, this dissertation presents a general theoretical framework to describe the momentum-resolved inelastic electron scattering of wide-field electrons from two-dimensional materials, spanning from atomic crystals to nanophotonic arrays. The formalism incorporates fully-retarded electromagnetic interactions, which are required to accurately model nanophotonic material responses. By accounting for the energy–momentum dependence of the probing electron's polarization and relativistic kinematics, the theory establishes selection rules for scattering processes within and beyond the first Brillouin zone, reveals optically dark transitions outside the light cone, and illustrates the roles of electron velocity and scattering geometry. Building on this theory and recent advances in structuring the transverse phase of electron beams, pinwheel free electron states carrying well-defined pseudoangular momentum (PAM) are also introduced. These beams enable direct detection of chiral phonons, a long-standing challenge for conventional characterization techniques. Taken together, this work establishes a pathway for tailoring the polarization and symmetry of free electron probes to selectively couple to targeted material excitations, enabling precise investigation of emergent material properties.

TABLE OF CONTENTS

LIST OF FIGURES

Figure Number Page

GLOSSARY

2D: Two-dimensional

EELS: Electron energy loss spectroscopy

TEM: Transmission electron microscope

STEM: Scanning transmission electron microscope

OAM: Orbital angular momentum

PAM: Psuedoangular momentum

q-EELS: Momentum-resolved electron energy loss spectroscopy

HREELS: High resolution electron energy loss spectroscopy

LSP: Localized surface plasmon

LPP: Lattice plasmon polariton

NN: Nearest-neighbor

NN: Next-nearest-neighbor

ACKNOWLEDGMENTS

I am grateful to my advisor, Prof. David Masiello, for his support, insightful guidance, and mentorship throughout the years. I especially appreciate his encouragement and the opportunities he provided for me to grow and develop as a researcher. I am also thankful to Prof. John Herbert at The Ohio State University for welcoming me into his group and mentoring me during my time as an undergraduate researcher. I sincerely thank Dr. Marc Bourgeois for his mentorship and generosity, as well as Dr. Elliot Beutler and Dr. Claire West for their valuable insights. I am grateful to my lab mates—Siamak Khorasani, Dr. C. Praise Anayanyu, Matthieu Chalifour, Dr. Austin Nixon, Xiaofei (Betty) Guo, Kevin Moser, Caleb Walton, Dr. Aniruddha (Ronnie) Bhattacharya, and Dr. Vishal Tiwari—for their friendship and camaraderie over the years.

Finally, I am deeply thankful for the unwavering support of my family and friends. I am especially grateful to Thomas Kaminsky for his patience in listening to my many rants when projects were not going as planned. I would also like to extend my gratitude to my grandparents, my parents—Amy and Anthony—and my siblings—Anthony, Jacquelyn, Alec, and Aidan—for their constant support and belief in me, without which I would not be here.

LIST OF PUBLICATIONS

1. Rossi, A. W., Bourgeois, M. R., Masiello, D. J. (2026). Free electron nanospectroscopy of truly chiral phonons with OAM-structured electron beams. *In preparation.*

2. O'Hara, A., Plotkin-Swing, B., Rossi, A. W., Bourgeois, M. R., Dellby, N., Idrobo, J. C., Krivanek, O. L., Masiello, D. J., Lovejoy, T. C., Pantelides, S. T. (2026). High-temperature phonons in h-BN: momentum-resolved vibrational spectroscopy and theory. *In preparation.*

3. Hershey, M., Liu, H., Guo, X., Rossi, A. W., Bourgeois, M. R., Clark, B. D., Gage, T. E., Arslan, I. Masiello, D. J., Swearer, D. F. (2025). Probing plasmonic near-fields in oxide-modified aluminum nanocubes using photon-induced near-field electron microscopy. *ACS Photonics*, 12, 11, 6002–6010. [1]

4. Bourgeois, M. R., Rossi, A. W., Masiello, D. J. (2025). Strategy for direct detection of chiral phonons with phase-structured free electrons. *Phys. Rev. Lett.*, 134, 026902. [2]

5. Rossi, A. W., Bourgeois, M. R., Walton, C., Masiello, D. J. (2024). Probing the polarization of low-energy excitations in 2D materials from atomic crystals to nanophotonic arrays using momentum-resolved electron energy loss spectroscopy. *Nano Lett.*, 24 (25), 7748-7756. [3]

6. Kumar, V., Rossi, A. W., Lawson, Z. R., Neal, R. D., Hachtel, J. A., Neretina, S., Masiello, D. J., Camden, J. P. (2023). Infrared near-field spectroscopy of gold nanotriangle fabry-pérot resonances. *J. Phys. Chem. C*, 127(14), 6777-6784. [4]

7. Bourgeois, M. R., Rossi, A. W., Khorasani, S., Masiello, D. J. (2022). Optical control

over thermal distributions in topologically trivial and non-trivial plasmon lattices. *ACS Photonics*, 9(11), 3656-3667. [5]

8. Garfinkel, D. A., Iyer, V., Seils, R., Pakeltis, G., Bourgeois, M. R., Rossi, A. W., Klein, C., Lawrie, B. J., Masiello, D. J., Rack, P. D. (2022). Visualizing electric and magnetic field coupling in Au-nanorod trimer structures via stimulated electron energy gain and cathodoluminescence spectroscopy: implications for meta-atom imaging. *ACS Appl. Nano Mater.*, 5(2), 1798-1807. [6]

9. Bourgeois, M. R., Rossi, A. W., Chalifour, M., Cherqui, C., Masiello, D. J. (2021). Lattice Kerker effect with plasmonic oligomers. *J. Phys. Chem. C*, 125(34), 18817-18826. [7]

Chapter 1

INTRODUCTION

1.1 Background and Motivation

Over the last few decades, periodic materials — such as atomic crystalline solids, photonic crystals, and engineered metamaterials — have garnered significant attention owing to their unique quantum [2, 8, 9], optical [7, 10–13], electronic [14–17], magnetic [18, 19], and thermal [5, 20] properties. These materials have becomes both platforms for studying fundamental physical phenomena as well as for developing advanced technologies in optoelectronics [15, 21–23], sensing [24], communications [25], and quantum information [26]. Unlike amorphous materials, periodic materials are characterized by structures and physical properties that repeat in space according to well-defined lattice vectors. This direct space periodicity naturally leads to a complementary description in reciprocal, or momentum, space, where the physical properties of the material can be reduced to those of a single fundamental region known as the Brillouin zone. The connection between direct and reciprocal space is formalized by Bloch's theorem, which provides the theoretical basis for describing waves and particles in periodic media in terms of crystal momentum [27]. In momentum space, the eigenfrequencies of a periodic material organize into continuous bands as a function of crystal Bloch momentum, giving rise to the band structure, which serves as a central framework for understanding and predicting properties of periodic materials.

This dissertation focuses on two representative classes of periodic materials: atomic crystals and plasmonic lattices, which in the low energy regime, support phonons and lattice plasmon polaritons (LPPs), respectively. Phonons, arising from the collective oscillations of atoms in a crystal lattice about their equilibrium positions, typically have excitation energies in the mid- to far-infrared part of the electromagnetic spectrum. In contrast, LPPs exhibit excitation energies spanning the visible to near-infrared range and originate from the electromagnetic coupling between localized surface plasmons (LSPs) of individual nanoparticles and the photonic modes supported by the underlying lattice structure [28]. LSP resonances, emerging from the collective oscillation of conduction band electrons, strongly depend on the material composition and nanoparticle size and morphology, while the photonic lattice modes are completely dictated by the lattice geometry.

As demonstrated in Figure 1.1, plasmonic lattices with the same underlying symmetries as naturally occurring two-dimensional (2D) atomic crystals can be nanoengineered using techniques such as electron-beam lithography [29]. Both 2D materials displayed in Figure 1.1 are manifestations of the honeycomb lattice, which is a non-Bravais lattice of hexagonal symmetry with two sites per unit cell. The unit cell of graphene contains two carbon atoms, while the plasmonic lattice unit cell is composed of two plasmonic nanoparticles. Despite sharing the same symmetry, these periodic materials span disparate spatial and momentum scales in addition to excitation energies. Typically, the characteristic length scale represented by the magnitude of the lattice vector a is on the Ångstrom scale for atomic crystals, while lattice constants for diffractively coupled plasmon lattices are hundreds of nanometers. These lattice constants lead to Brillouin zones on the order of 10 nm^{-1} and 10 μm^{-1} for atomic crystals and plasmonic lattices, respectively.

Despite the disparate spatial, momentum, and energy scales spanned by atomic crystals and plasmonic arrays, characterization techniques employing low-energy electrons, such as high-resolution electron energy-loss spectroscopy (HREELS) and EELS performed inside a scanning transmission electron microscope (STEM), are among the most powerful techniques for studying the material proprieties of these systems. Depending on the instrument and experimental parameters, these characterization techniques are capable of achieving a combination of high spatial, energy, polarization, linear momentum, orbital angular momentum (OAM), and psuedoangular momentum (PAM) resolution. Electron probes, owing to their distinct and tunable polarization properties, can also excite dark modes that are inaccessible to optical-based techniques. Furthermore, electrons, unlike photons, are not limited by the optical light cone, enabling access to momentum content that lies well beyond the first Brillouin zone. Although this dissertation primarily focuses on HREELS and momentum-resolved EELS (q-EELS) in a STEM or wide-field q-EELS in a TEM, other characterization techniques utilizing low-energy electrons, such as low energy electron diffraction

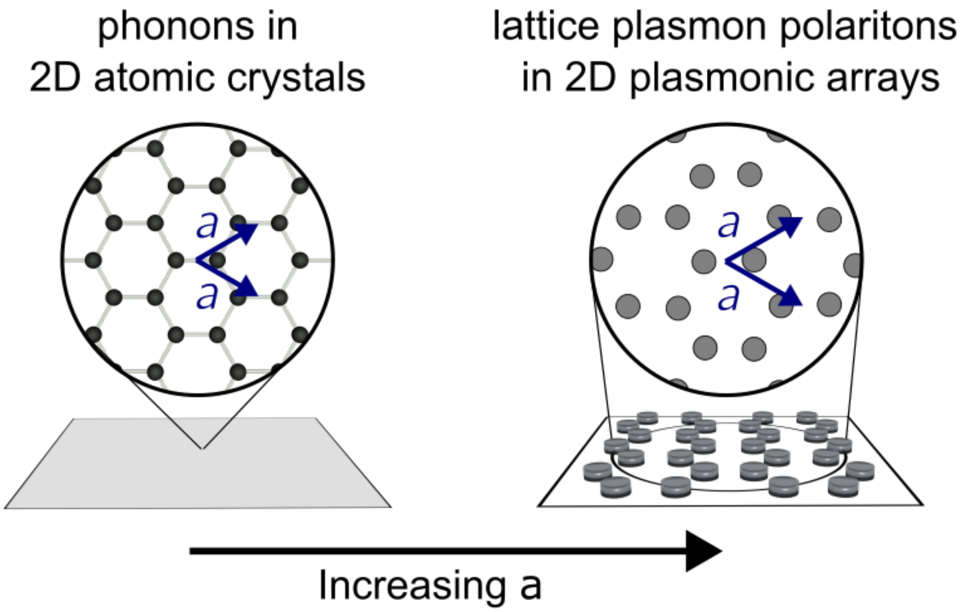

Figure 1.1: Graphene and a nanoengineered 2D honeycomb plasmonic lattice with lattice constant a.

(LEED) [30] and scanning tunneling microscopy (STM) [31, 32], have played a crucial role in elucidating a range of material properties.

Over the last decade, advances in aberration correction and monochromation inside a STEM have enabled the identification of single atomic defects [33, 34] as well as the mapping of individual vibrational modes [35–38] in atomic crystals. Although STEM-EELS offers atomic-scale spatial resolution, its reliance on momentum space integration limits its use as a probe for reciprocal space excitations. However, q-EELS performed inside a STEM or TEM overcomes this challenge by increasing the incident beam width, which at the expense of sacrificing spatial resolution, provides momentum resolution. The high momentum and energy resolution q-EELS has demonstrated the ability to characterize the dispersive responses of 2D materials [14, 38, 39, 39, 40]. Similarly, HREELS [41–50], adapted from its original role in surface science, has enabled the extraction of detailed excitation information in 2D materials with high energy and momentum resolution.

Like 2D atomic crystals, 2D plasmonic lattices have recently received significant attention, owing to their unique ability, among other things, to support tunable nanolasers [10–13], bound states in the continuum (BICs) [51–57], and exciton polaritons [58–63]. Investigating these phenomena is often challenging, however, as measurements require simultaneously high momentum, energy, and polarization resolution. While optical-based techniques are routinely and successfully employed to characterize these materials, they are fundamentally limited by photon polarization and by their inability to access momenta outside the of the light cone boundary. The use of q-EELS, which can overcome these challenges, has been limited to the study of photonic density of states in the vicinity of plasmonic thin film architectures [64] and crystal defects [65]. For studying LSPs in individual nanoparticles, STEM-EELS, with its high spatial and energy resolution, has played a crucial role [66–69]. Building on this success and motivated by the demonstrated capabilities of q-EELS and HREELS applied to atomic crystals, our recent theoretical work [3] highlights the strong potential of EELS for probing momentum-resolved excitations in plasmonic lattices.

In parallel, substantial progress has been made in shaping the transverse phase profile and OAM of free electrons using phase plates [70], holographic masks [71, 72], and shaped laser pulses [73]. These advances have enabled the pre- and post-selection of transverse electron phase profiles in low-loss inelastic electron scattering [74–80]. Beyond localized nanoscopic targets, this body of work presents the opportunity to probe momentum-resolved OAM excitations in periodic materials. Separately, our recent theoretical work introduces incident electron pinwheel states with well-defined PAM, the analog of OAM in periodic systems [2]. PAM-resolved probes offer the ability to distinguish the PAM of chiral phonons, which has remained an outstanding challenge using conventional characterization techniques.

1.2 Outline of Dissertation

This dissertation is organized into individual chapters. Chapter 2 outlines theoretical background relevant to the publications presented in Chapters 3–5. The theory chapter begins with Section 2.1, which provides an overview of a theoretical model to obtain the induced phonon dipole moments of 2D atomic crystals, which can readily be generalized for three-dimensional (3D) crystals. As outlined in Section 2.1.1, the first step is to construct and diagonalize the dynamical matrix to obtain the phonon eigenmodes and associated eigenfrequencies. While the force constants of the dynamical matrix in atomic crystals are typically obtained using density functional perturbation theory (DFPT), Section 2.1.2 considers two toy models including interactions up to nearest-neighbor (NN) and next-nearest-neighbor (NNN). Despite their simplicity, these models provide valuable qualitative insight into the phonon band structure and its dependence on the coupling parameters. Finally, Section 2.1.3 discusses how to compute the induced phonon dipole moments in reciprocal space for an arbitrary forcing electric field from the underlying eigenmodes and associated eigenfrequencies. Separately, Section 2.2 provides an overview of how to compute the induced dipole moments of LPP systems using the method of coupled electric dipoles.

Section 2.3 reviews an analytical derivation of the electric field inducing the dipoles in Sections 2.1.3 and 2.2. Specifically, this section considers the wide-field transition electric field associated with a probing electron transitioning between incoming and outgoing plane wave states. This section also includes plots illustrating the dependence of the polarization content of the transition electric field on parameters such as scattering geometry and electron speed. Section 2.3.1 reviews a derivation of the quasistatic transition electric field applicable to atomic crystals, for which electromagnetic retardation effects are negligible. Finally, Section 2.4 provides a derivation of the wide-field EEL observable known as the the double-differential cross section (DDCS), which is a general expression applicable to study phonons in atomic crystals and LPPs in plasmonic lattices in both reflection and transmission scattering geometries.

Before discussing crystal excitations in the electron microscope, Chapter 3 presents a specific photothermal application of plasmonic lattices. In this work [5], we theoretically demonstrate the ability to create LPP thermal gradients spanning from the nanoscale to hundreds of microns. Despite thermal diffusion, these steady-state temperature distributions are actively controllable using the frequency and angle of incidence of light. In addition, we exploit the proprieties of topologically non-trivial LPP dimer lattices to create lattice edge-localized thermal gradients. Taken together, this work introduces a new class of photothermal materials with actively tunable properties.

Chapter 4 presents recent work [3], in which we introduce a general theoretical framework for describing momentum-resolved EELS from 2D materials, spanning from atomic crystals to plasmonic arrays. While well established as a probe for atomic crystals, 2D plasmonic arrays present a distinctly new physical regime where incorporating electromagnetic retardation effects is indispensable. This fully-retarded theory elucidates selection rules for scattering processes within and beyond the first Brillouin zone, highlights the ability of q-EELS to excite optically dark transitions, and reveals how the polarization content of the probing electron varies with electron velocity and scattering geometry. By comparing infrared phonon excitations in graphene to optical-frequency LPP excitations in a plasmonic lattice, we demonstrate the general utility of wide-field EELS for probing excitations in 2D materials, while underscoring the ability to tailor its polarization content to selectively excite material modes of interest.

Building on this work, Chapter 5 introduces pinwheel free electron states with well-defined PAM capable of chiral phonon discrimination [2]. While chiral phonons with well-defined PAM underpin a variety of applications, their universal and direct detection has remained a challenge, as it requires a probe with simultaneously high linear momentum, PAM, energy, and spatial resolution. As we theoretically demonstrate, electron pinwheel states overcome the limitations of optical-based techniques, whose spatial and linear momentum resolution are fundamentally limited by the wavelength of the probing photons. This work paves the way for generating field vortices with engineered polarization textures designed to selectively couple to chiral material excitations of different symmetries.

Chapter 2

THEORETICAL BACKGROUND

2.1 *2D Atomic Crystal Phonon Model*

This section provides an overview of a theoretical model to obtain the induced phonon dipole moments of 2D atomic crystals. The first step is to construct and diagonalize the dynamical matrix, yielding a set of phonon eigenmodes and associated eigenfrequencies.

2.1.1 Dynamical Matrix

For a 2D atomic crystal comprised of N unit cells each containing s atomic sites, the positions of the unit cell centers are those of the corresponding Bravais lattice $\mathbf{x}_\mathbf{n} = n_1\mathbf{a}_1 + n_2\mathbf{a}_2$, where $\mathbf{a}_l$ with $l = 1, 2$ denotes the primitive lattice vectors, and $\mathbf{n} = (n_1, n_2)$ specifies each unit cell relative to an arbitrarily selected origin. The equilibrium positions of the atoms are given by $\mathbf{x}_{\mathbf{n}\kappa} = \mathbf{x}_\mathbf{n} + \mathbf{r}_\kappa$,where $\mathbf{r}_\kappa$ indicates the position of the κth atom within the unit cell with $\kappa \in \{1, ..., s\}$. In Figure 2.1, an example of a honeycomb lattice in direct space with the $\mathbf{n} = (0, 0)$ unit cell, $\mathbf{a}_l$, and $\mathbf{r}_\kappa$ labeled is shown. For a given atom, the instantaneous displacement vector away from equilibrium is given by $\mathbf{u}_{\mathbf{n}\kappa}$. Therefore, we can express the instantaneous positions of the atoms as $\mathbf{R}_{\mathbf{n}\kappa} = \mathbf{x}_{\mathbf{n}\kappa} + \mathbf{u}_{\mathbf{n}\kappa}$. Under the harmonic approximation, the potential energy of the lattice can be expressed as [81, 82]

$$V^{(2)} = \frac{1}{2}\sum_{\mathbf{n}\kappa}\sum_{\mathbf{n}'\kappa'} \mathbf{u}_{\mathbf{n}\kappa} \cdot \bar{\mathbf{\Phi}}_{\mathbf{n}\kappa;\mathbf{n}'\kappa'} \cdot \mathbf{u}_{\mathbf{n}'\kappa'}, \tag{2.1}$$

where the 3×3 force constant matrix $\bar{\mathbf{\Phi}}_{\mathbf{n}\kappa;\mathbf{n}'\kappa'}$ has elements $\Phi^{ij}_{\mathbf{n}\kappa;\mathbf{n}'\kappa'} = \partial^2\Phi/\partial u^i_{\mathbf{n}\kappa}\partial u^j_{\mathbf{n}'\kappa'}$ with $i, j = x, y, z$. In general, these coupling parameters are obtained from density functional perturbation theory (DFPT) as implemented in software packages such as VASP [83, 84] or Quantum Espresso [85, 86] or extracted from empirical data [87, 88]. The kinetic energy of the crystal is given by

$$T = \sum_{\mathbf{n}\kappa} \frac{\mathbf{p}^2_{\mathbf{n}\kappa}}{2M_\kappa}, \tag{2.2}$$

where $\mathbf{p}_{\mathbf{n}\kappa}$ is the atomic momentum and M_κ is the mass of the κth atom. The crystal dynamics can be described by a system of $3sN$ coupled equations

$$M_\kappa \ddot{\mathbf{u}}_{\mathbf{n}\kappa} = -\sum_{\mathbf{n}'\kappa'} \bar{\mathbf{\Phi}}_{\mathbf{n}\kappa;\mathbf{n}'\kappa'} \cdot \mathbf{u}_{\mathbf{n}'\kappa'}. \tag{2.3}$$

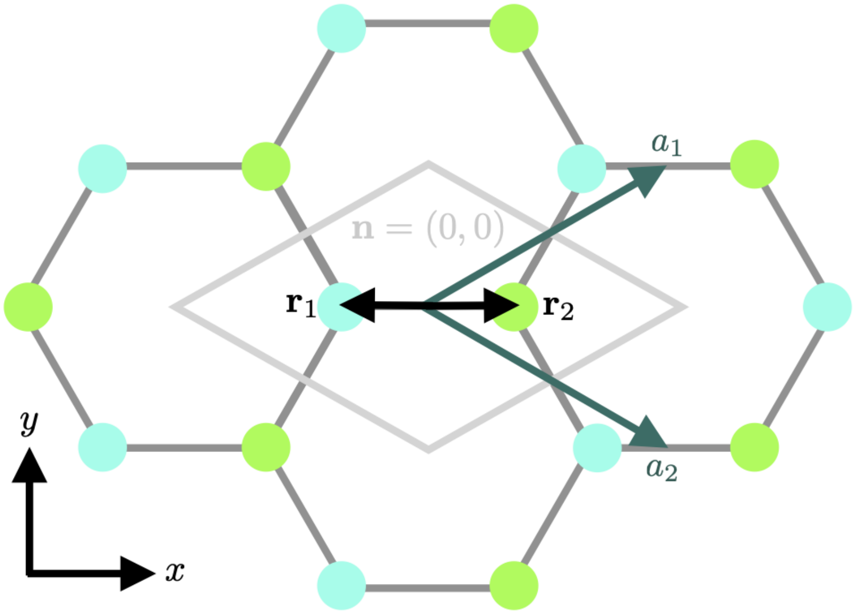

Figure 2.1: Honeycomb lattice in direct space.

To move into reciprocal space, we can apply periodic boundary conditions and perform a mass-weighted spatial Fourier transform and assume periodic time dependence with frequency ω, allowing us to write

$$\mathbf{u}_{\mathbf{n}\kappa} = \frac{1}{\sqrt{M_\kappa N}} \sum_{\mathbf{K}} \tilde{\mathbf{u}}_{\mathbf{K}\kappa} e^{i\mathbf{K}\cdot\mathbf{x}_\mathbf{n} - i\omega t}, \tag{2.4}$$

where $\mathbf{K}$ is the 2D Bloch vector. The reciprocal space equation of motion can then be expressed as

$$\omega^2 \tilde{\mathbf{u}}_{\mathbf{K}\kappa} = \sum_{\kappa'} \bar{\mathbf{D}}_{\kappa\kappa'}(\mathbf{K}) \cdot \tilde{\mathbf{u}}_{\mathbf{K}\kappa'}, \tag{2.5}$$

where $\bar{\mathbf{D}}_{\kappa\kappa'}(\mathbf{K})$ are 3×3 block matrices of the dynamical matrix $\bar{\bar{\mathbf{D}}}(\mathbf{K})$ given by

$$\bar{\mathbf{D}}_{\kappa\kappa'}(\mathbf{K}) = \frac{1}{\sqrt{M_\kappa M_{\kappa'}}} \sum_{\mathbf{n}'} \bar{\mathbf{\Phi}}_{\mathbf{n}\kappa;\mathbf{n}'\kappa'} e^{i\mathbf{K}\cdot(\mathbf{x}_{\mathbf{n}'} - \mathbf{x}_{\mathbf{n}})}. \tag{2.6}$$

Note that the 3×3 block matrices of the dynamical matrix can alternatively be defined as

$$\bar{\mathbf{B}}_{\kappa\kappa'}(\mathbf{K}) = \frac{1}{\sqrt{M_\kappa M_{\kappa'}}} \sum_{\mathbf{n}'} \bar{\mathbf{\Phi}}_{\mathbf{n}\kappa;\mathbf{n}'\kappa'} e^{i\mathbf{K}\cdot(\mathbf{x}_{\mathbf{n}'\kappa'} - \mathbf{x}_{\mathbf{n}\kappa})}, \tag{2.7}$$

where

$$\bar{\mathbf{D}}_{\kappa\kappa'}(\mathbf{K}) = e^{-i\mathbf{K}\cdot\mathbf{r}_{\kappa'}} \bar{\mathbf{B}}_{\kappa\kappa'}(\mathbf{K}) e^{i\mathbf{K}\cdot\mathbf{r}_\kappa} \tag{2.8}$$

when the mass-weighted spatial Fourier transform is defined as

$$\mathbf{u}_{\mathbf{n}\kappa} = \frac{1}{\sqrt{M_\kappa N}} \sum_{\mathbf{K}} \tilde{\mathbf{u}}_{\mathbf{K}\kappa} e^{i\mathbf{K}\cdot\mathbf{x}_{\mathbf{n}\kappa} - i\omega t}. \tag{2.9}$$

Although both conventions are equally valid, the Fourier transform of the forcing electric field introduced in Section 2.3 must be defined consistently.

In general, $\bar{\mathbf{D}}_{\kappa\kappa'}(\mathbf{K}) = \bar{\mathbf{F}}_{\kappa\kappa'}(\mathbf{K}) + \bar{\mathbf{C}}_{\kappa\kappa'}(\mathbf{K})$, where $\bar{\mathbf{F}}_{\kappa\kappa'}(\mathbf{K})$ and $\bar{\mathbf{C}}_{\kappa\kappa'}(\mathbf{K})$ represent covalent and ionic interactions between atomic sites κ and κ', respectively. Diagonalization of $\bar{\bar{\mathbf{D}}}(\mathbf{K})$ produces a set of $\lambda = 3s$ vibrational phonon eigenmodes $\{\boldsymbol{\xi}_\lambda\}$ and associated eigenfrequencies ω_λ^2, both of which depend implicitly on the Bloch vector $\mathbf{K}$. Note that if $\mathbf{K} = \mathbf{K}' + \mathbf{G}$, where $\mathbf{G}$ is a reciprocal lattice vector and $\mathbf{K}'$ lies within the first BZ, then $\bar{\mathbf{D}}_{\kappa\kappa'}(\mathbf{K}' + \mathbf{G}) = \bar{\mathbf{D}}_{\kappa\kappa'}(\mathbf{K}')$. In addition, $\bar{\mathbf{D}}_{\kappa\kappa'}(\mathbf{K}) = \bar{\mathbf{D}}_{\kappa'\kappa}(\mathbf{K})^*$ and $\bar{D}^{ij}_{\kappa\kappa'}(\mathbf{K}) = \bar{D}^{ji}_{\kappa\kappa'}(\mathbf{K})$.

2.1.2 Dynamical Matrix Models

Before proceeding further, this section reviews two simple dynamical matrix models: the nearest-neighbor (NN) and next-nearest-neighbor (NNN) models. Although these toy models are quite simple, they provide valuable qualitative insight into the phonon band structure and its dependence on the coupling parameters. As two examples that directly connect to 2D materials of interest, we investigate the honeycomb and Kagome lattices, which are non-Bravais lattices of hexagonal symmetry with 2 and 3 particles per unit cell, respectively. Examples of naturally occurring honeycomb atomic crystal lattices include graphene, silicine, hBN, and MoS_2, while AV_3Sb_5 (A = K, Rb, Cs) and FeSn are examples of kagome atomic crystals.

To construct the phonon band structure along the perimeter of the irreducible Brillouin zone, the eigenfrequencies at a given 2D Bloch vector $\mathbf{K}$ can be obtained by diagonalizing Eq. (2.7). In this section, we specialize to a dynamical matrix truncated at either NN or NNN interactions such that

$$\begin{aligned}\bar{\mathbf{B}}_{\kappa\kappa'}(\mathbf{K}) = \frac{1}{\sqrt{M_\kappa M_{\kappa'}}}\Bigg[&\sum_{\mathbf{n}'\in NN} D_{NN}\hat{\mathbf{X}}_{\mathbf{n}\kappa;\mathbf{n}'\kappa'}\hat{\mathbf{X}}_{\mathbf{n}\kappa;\mathbf{n}'\kappa'}\ e^{i\mathbf{K}\cdot\mathbf{X}_{\mathbf{n}\kappa;\mathbf{n}'\kappa'}} \\ &+\sum_{\mathbf{n}'\in NNN} D_{NNN}\hat{\mathbf{X}}_{\mathbf{n}\kappa;\mathbf{n}'\kappa'}\hat{\mathbf{X}}_{\mathbf{n}\kappa;\mathbf{n}'\kappa'}\ e^{i\mathbf{K}\cdot\mathbf{X}_{\mathbf{n}\kappa;\mathbf{n}'\kappa'}}\Bigg],\end{aligned} \tag{2.10}$$

where D_{NN} and D_{NNN} are the associated force constants and $\mathbf{X}_{\mathbf{n}\kappa;\mathbf{n}'\kappa'} = \mathbf{x}_{\mathbf{n}'\kappa'} - \mathbf{x}_{\mathbf{n}\kappa}$. For the kagome lattice, NN interactions are further partitioned into intracellular and intercellular represented by D_{NN} and D'_{NN}, respectively. To satisfy the acoustic sum rule [82], $\bar{\mathbf{\Phi}}_{\mathbf{n}\kappa;\mathbf{n}\kappa} = -\sum_{\mathbf{n}\kappa\neq\mathbf{n}'\kappa'} \bar{\mathbf{\Phi}}_{\mathbf{n}\kappa;\mathbf{n}'\kappa'}$. Therefore, the diagonal elements of the dynamical matrix (i.e., $\kappa = \kappa'$) are given by

$$\bar{\mathbf{B}}_{\kappa\kappa}(\mathbf{K}) = -\frac{1}{M_\kappa}\Bigg[\sum_{\mathbf{n}\kappa\neq\mathbf{n}'\kappa'\in NN} D_{NN}\hat{\mathbf{X}}_{\mathbf{n}\kappa;\mathbf{n}'\kappa'}\hat{\mathbf{X}}_{\mathbf{n}\kappa;\mathbf{n}'\kappa'} + \sum_{\mathbf{n}\kappa\neq\mathbf{n}'\kappa'\in NNN} D_{NNN}\hat{\mathbf{X}}_{\mathbf{n}\kappa;\mathbf{n}'\kappa'}\hat{\mathbf{X}}_{\mathbf{n}\kappa;\mathbf{n}'\kappa'}\Bigg]. \tag{2.11}$$

In Figure 2.2, the phonon band structures computed up to NN (blue) and NNN (red) interactions are displayed for both a symmetry-unbroken (left) and symmetry-broken (right) honeycomb lattice. The corresponding interactions for the $\kappa = 1$ atomic site within the central unit cell are shown in the direct space diagram along with the lattice vectors $\mathbf{a}_1 = [a\sqrt{3}/2, a/2]$ and $\mathbf{a}_2 = [a\sqrt{3}/2, -a/2]$, where a is the corresponding lattice vector magnitude. On the right, the Brillouin zone is depicted along with the three high symmetry reciprocal space points: $\mathbf{\Gamma} = [0, 0]$, $\mathbf{M} = [2\pi/(\sqrt{3}a), 0]$, and $\mathbf{K} = [2\pi/(\sqrt{3}a), 2\pi/(3a)]$. For honeycomb lattices, the lattice constant is related to the bond length via $a = \sqrt{3}a_0$, where a_0 is the atom-atom bond length.

For both the symmetry-unbroken and symmetry-broken honeycomb band structures displayed in Figure 2.2, $D_{NN} = 1$ and $D_{NNN} = 0.01$. Although the highest energy phonon band appears nearly dispersionless, increasing D_{NNN} will increase the extent of its dispersion. As evident, there are $ds = 4$ in-plane phonon bands, where $d = 2$ and $s = 2$ are the lattice dimensionality and number of sublattices, or sites per unit cell, respectively. The number of acoustic bands (i.e., where $\omega \to 0$ as $\Gamma \to 0$) is always equal to the dimensionality of the lattice, meaning there are $d = 2$ acoustic branches and two optical branches for a 2D honeycomb lattice. In models that include out-of-plane atomic displacements, there are $ds = 6$ phonon bands, three of which are acoustic.

The symmetry of the honeycomb lattice is broken by modifying the mass of one atomic site relative to the other. In the band structures shown in Figure 2.2, $M_1 = M_2$ in the symmetry-unbroken lattice, whereas $M_1 = 0.5M_2$ in the symmetry-broken case. When the symmetry of the lattice is broken leading to a symmetry reduction from C_6 to C_3, the degeneracy of the Dirac phonon mode at the K point is lifted. The topological and chiral features of this mode have been extensively explored in graphene and hBN in recent years [2, 9, 44]. Another important observation is the existence of a zero-energy floppy band in the underconstrained strictly NN model. It is well-known that this band is lifted to finite frequency when NNN interactions are included [89, 90].

In Figure 2.3, the phonon band structures computed up to NN (blue) and NNN (red) are displayed for both a symmetry-unbroken (left) and symmetry-broken (right) kagome lattice. The corresponding interactions for the $\kappa = 1$ atomic site within the central unit cell are shown in the direct space diagram along with the lattice vectors $\mathbf{a}_1 = [a, 0]$ and $\mathbf{a}_2 = [a/2, \sqrt{3}a/2]$, where a is the corresponding lattice vector magnitude. The solid (dashed) blue lines represent intracellular (intercellular) interactions. Similar to honeycomb lattices, the kagome lattice possesses hexagonal symmetry, resulting in the same BZ and three high symmetry reciprocal space points: $\boldsymbol{\Gamma} = [0, 0]$, $\mathbf{M} = [2\pi/(\sqrt{3}a), 0]$, and $\mathbf{K} = [2\pi/(\sqrt{3}a), 2\pi/(3a)]$. For kagome lattices, however, the lattice constant is related to the bond length via $a = 2a_0$, where a_0 is the atom-atom bond length.

As evident in Figure 2.3, there are $ds = 6$ in-plane phonon bands, where $d = 2$ and $s = 3$ for the kagome lattice. The symmetry of the honeycomb lattice is broken by modifying the the intracellular NN force constant D_{NN} relative to the intercellular D'_{NN}. In the specific kagome lattices shown in Figure 2.2, $D_{NN} = D'_{NN}$ in the symmetry-unbroken lattice, whereas $D_{NN} = 1.2D'_{NN}$ in the symmetry-broken case. For both lattices, $D_{NNN} = 0.01$ and $M_1 = M_2 = M_3 = 1$. Like the Honeycomb lattice, the degeneracy of the Dirac phonon mode at the K point is lifted when the symmetry of the kagome lattice is broken (i.e., when $D_{NN} \neq D'_{NN}$). The floppy mode along the $\Gamma - M$ direction in the NN model is also resolved

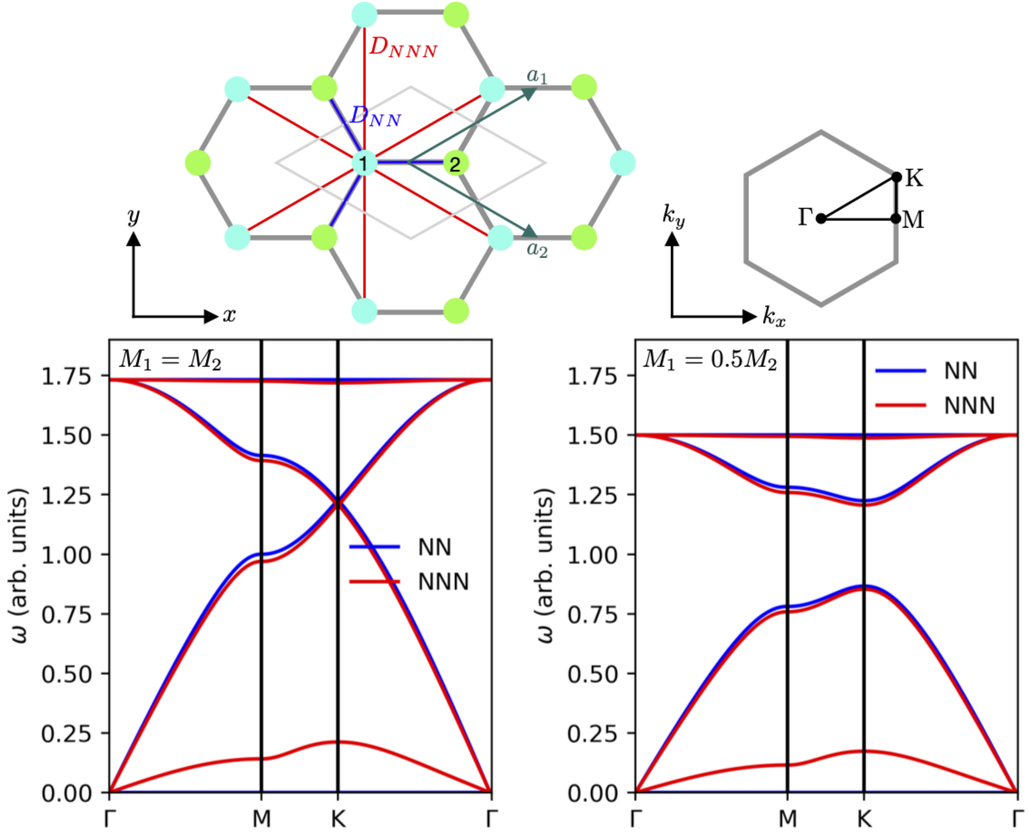

Figure 2.2: Phonon band structure for symmetry-unbroken (left) and symmetry-broken (right) honeycomb NN and NNN dynamical matrix models.

when NNN interactions are included.

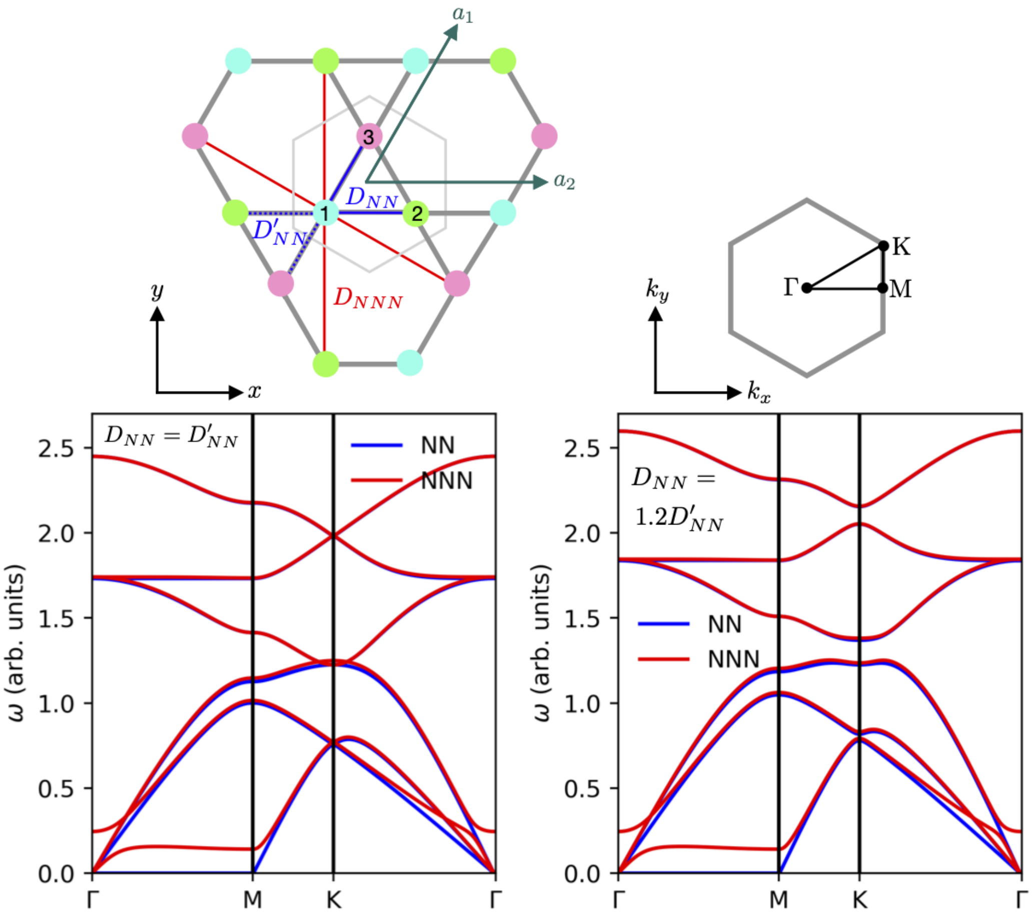

Figure 2.3: Phonon band structure for symmetry-unbroken (left) and symmetry-broken (right) kagome NN and NNN dynamical matrix models.

2.1.3 Induced Dipole Moments

Given phonon eigenmodes $\boldsymbol{\xi}_\lambda$ and associated eigenfrequencies ω_λ^2 obtained from diagonalization the dynamical matrix, this section outlines how to compute the induced phonon dipole moments for a 2D atomic crystal. To start, we add empirical damping and external forcing to Eq. (2.3), resulting in the following equation of motion [91]

$$M_\kappa \ddot{\mathbf{u}}_{\mathbf{n}\kappa} + M_\kappa \dot{\mathbf{u}}_{\mathbf{n}\kappa}\eta + \sum_{\mathbf{n}'\kappa'} \bar{\mathbf{\Phi}}_{\mathbf{n}\kappa;\mathbf{n}'\kappa'} \cdot \mathbf{u}_{\mathbf{n}'\kappa'} = e\bar{\mathbf{Z}}_\kappa \cdot \mathbf{E}^0_{fi,\mathbf{n}\kappa}, \tag{2.12}$$

where η is an empirical damping constant, $e\bar{\mathbf{Z}}_\kappa$ is the effective charge tensor of the κth atom, and $\mathbf{E}^0_{fi,\mathbf{n}\kappa}$ is the forcing electric field, here taken to be the vacuum transition electric field associated with an electron transitiong between incoming and outgoing plane wave states, which is formally derived in Sec. 2.3. As demonstrated in Ref. [3], this wide-field transition electric field is characteristic of q-EELS and HREELS experiments.

As before, we perform a spatial Fourier transform with momentum conservation requiring $\mathbf{K} = \mathbf{K}' + \mathbf{G} = \mathbf{q}_\parallel$, where $\mathbf{G}$ is a reciprocal lattice vector and $\mathbf{K}'$ lies within the first BZ:

$$\mathbf{u}_{\mathbf{n}\kappa} = \frac{1}{N} \sum_{\mathbf{q}_\parallel} \mathbf{u}_{\mathbf{q}_\parallel \kappa} e^{i\mathbf{q}_\parallel \cdot \mathbf{x}_\mathbf{n} - i\omega t}, \tag{2.13}$$

which leads to the following equation of motion for the Bloch wave amplitudes

$$-\omega^2 M_\kappa \mathbf{u}_{\mathbf{q}_\parallel \kappa} - i\eta\omega M_\kappa \mathbf{u}_{\mathbf{q}_\parallel \kappa} + \sum_{\mathbf{n}'\kappa'} e^{i\mathbf{q}_\parallel \cdot (\mathbf{x}_{\mathbf{n}'} - \mathbf{x}_\mathbf{n})} \bar{\mathbf{\Phi}}_{\mathbf{n}\kappa;\mathbf{n}'\kappa'} \cdot \mathbf{u}_{\mathbf{q}_\parallel \kappa'} = e\bar{\mathbf{Z}}_\kappa(\mathbf{q}_\parallel) \cdot \mathbf{E}^0_{fi,\mathbf{q}_\parallel \kappa}. \tag{2.14}$$

After multiplying both sides by $1/\sqrt{M_\kappa}$ and multiplying the second term by $\sqrt{M_{\kappa'}}/\sqrt{M_{\kappa'}}$, this becomes

$$-\omega^2 \tilde{\mathbf{u}}_{\mathbf{q}_\parallel \kappa} - i\eta\omega \tilde{\mathbf{u}}_{\mathbf{q}_\parallel \kappa} + \frac{1}{\sqrt{M_\kappa M_{\kappa'}}} \sum_{\mathbf{n}'\kappa'} e^{i\mathbf{q}_\parallel \cdot (\mathbf{x}_{\mathbf{n}'} - \mathbf{x}_\mathbf{n})} \bar{\mathbf{\Phi}}_{\mathbf{n}\kappa;\mathbf{n}'\kappa'} \cdot \mathbf{u}_{\mathbf{q}_\parallel \kappa'} = M_\kappa^{-1/2} e\bar{\mathbf{Z}}_\kappa(\mathbf{q}_\parallel) \cdot \mathbf{E}^0_{fi,\mathbf{q}_\parallel \kappa}, \tag{2.15}$$

or

$$-\omega^2 \tilde{\mathbf{u}}_{\mathbf{q}_\parallel \kappa} - i\eta\omega \tilde{\mathbf{u}}_{\mathbf{q}_\parallel \kappa} + \sum_{\kappa'} \bar{\mathbf{D}}_{\kappa\kappa'}(\mathbf{q}_\parallel) \cdot \tilde{\mathbf{u}}_{\mathbf{q}_\parallel \kappa'} = M_\kappa^{-1/2} e\bar{\mathbf{Z}}_\kappa(\mathbf{q}_\parallel) \cdot \mathbf{E}^0_{fi,\mathbf{q}_\parallel \kappa}. \tag{2.16}$$

where $\tilde{\mathbf{u}}_{\mathbf{q}_\parallel \kappa} = \sqrt{M_\kappa}\mathbf{u}_{\mathbf{q}_\parallel \kappa}$ are mass-weighted Bloch wave amplitudes.

The s versions of Eq. (2.16) can be organized into a single $(3s \times 3s)$ matrix equation

$$\left[(-\omega^2 - i\omega\eta)\bar{\bar{\mathbf{I}}} + \bar{\bar{\mathbf{D}}}(\mathbf{q}_\parallel)\right]\tilde{\mathbf{u}}_{\mathbf{q}_\parallel} = \bar{\bar{\mathbf{Q}}}\bar{\bar{\mathbf{M}}}^{-\frac{1}{2}}\mathbf{E}^0_{\mathbf{q}_\parallel}, \tag{2.17}$$

where the double bars over matrices denote that a matrix is $(3s \times 3s)$ rather than (3×3), and vector quantities without a κ index also belong to this higher-dimensional space. The diagonal charge $\bar{\bar{\mathbf{Q}}}$ and mass $\bar{\bar{\mathbf{M}}}$ matrices are constructed as $\bar{\bar{\mathbf{Q}}} = \sum_\kappa \bar{\bar{\mathbf{I}}}_{\kappa\kappa} Z_\kappa e$ and $\bar{\bar{\mathbf{M}}} =$

$\sum_\kappa \bar{\bar{\mathbf{I}}}_{\kappa\kappa} M_\kappa$, where $\bar{\bar{\mathbf{I}}}_{\kappa\kappa}$ is a matrix of zeros except for a (3×3) identity matrix $\bar{\mathbf{I}}$ in the κth diagonal block.

By inverting Eq. (2.17), the induced dipole moment vector can be expressed as

$$\begin{aligned} \mathbf{p}_{\mathbf{q}_\parallel} &= \bar{\bar{\mathbf{Q}}}\mathbf{u}_{\mathbf{q}_\parallel} \\ &= \bar{\bar{\mathbf{Q}}}\bar{\bar{\mathbf{M}}}^{-\frac{1}{2}}\tilde{\mathbf{u}}_{\mathbf{q}_\parallel} \\ &= \bar{\bar{\mathbf{Q}}}^2\bar{\bar{\mathbf{M}}}^{-1}\left[(-\omega^2 - i\omega\eta)\bar{\bar{\mathbf{I}}} + \bar{\bar{\mathbf{D}}}(\mathbf{q}_\parallel)\right]^{-1}\mathbf{E}^0_{\mathbf{q}_\parallel}. \end{aligned} \tag{2.18}$$

After inserting a resolution of the identity $\sum_\lambda \boldsymbol{\xi}^*_\lambda \boldsymbol{\xi}_\lambda$ and using the eigen equation $\bar{\bar{\mathbf{D}}}(\mathbf{q}_\parallel)\cdot\boldsymbol{\xi}_\lambda = \omega^2_\lambda \boldsymbol{\xi}_\lambda$, we can write

$$\mathbf{p}_{\mathbf{q}_\parallel\kappa} = e\bar{\mathbf{Z}}_\kappa(\mathbf{q}_\parallel)\cdot M^{-1/2}\sum_\lambda \frac{F_\lambda(\mathbf{q}_\parallel)}{\omega^2_\lambda - \omega(\omega + i\eta)}\boldsymbol{\xi}_{\lambda\kappa} \tag{2.19}$$

where $\mathbf{p}_{\mathbf{q}_\parallel\kappa} = e\bar{\mathbf{Z}}_\kappa(\mathbf{q}_\parallel)M_\kappa^{-1/2}\tilde{\mathbf{u}}_{\mathbf{q}_\parallel\kappa}$, $F_\lambda(\mathbf{q}_\parallel) = \sum_\kappa \boldsymbol{\xi}^*_{\lambda\kappa}\cdot M_\kappa^{-1/2}\cdot e\bar{\mathbf{Z}}_\kappa(\mathbf{q}_\parallel)\cdot\mathbf{E}^0_{fi,\mathbf{q}_\parallel\kappa}$, and $e\bar{\mathbf{Z}}_\kappa(\mathbf{q}_\parallel)$ is the $\mathbf{q}$-dependent Born effective charge matrix with elements given by [39, 92–94]

$$Z_{\kappa,ij} = Z_{\text{ion}}\delta_{ij} + Z^*_{\kappa,ij}, \tag{2.20}$$

where the second term is computed as

$$Z^*_{\kappa,ij} = \frac{\partial P_i}{\partial u_{\kappa,j}} = \frac{A}{(2\pi)^2}\int_{\text{BZ}} d^2\mathbf{K}\;\Omega_{K_i u_{\kappa,j}}(\mathbf{K}), \tag{2.21}$$

which establishes a direct connection to the Chern number and topology [94]. In Eq. (2.21), P_i is the ith component of the macroscopic polarization and $\Omega_{K_i u_{\kappa,j}}(\mathbf{K})$ is the Berry curvature.

2.2 Lattice Plasmon Polariton (LPP) Model

Within the coupled dipole approximation, the electromagnetic response of each particle is characterized by the induced electric dipole $\mathbf{p}_{\mathbf{n}\kappa}(\omega) = \bar{\boldsymbol{\alpha}}_\kappa(\omega)\mathbf{E}_{\mathbf{n}\kappa}(\omega)$, where $\bar{\boldsymbol{\alpha}}_\kappa(\omega)$ is the dipole polarizability tensor for sublattice κ. As in the case of phonons (Section 2.1.3), $\mathbf{x}_\mathbf{n}$ denotes the center of the real space unit cell indexed by n_1 and n_2, and $\mathbf{r}_\kappa$ is the displacement of site $\kappa \in \{1, ..., s\}$ relative to the center of the unit cell such that $\mathbf{x}_{\mathbf{n}\kappa} = \mathbf{x}_\mathbf{n} + \mathbf{r}_\kappa$. Most plasmonic noble metals including silver, gold, and copper are optically isotropic, so the anisotropy of a nanoparticle's dipolar response is primarily determined by its geometry. In the particle's principal axes, the electric dipole polarizability tensor is therefore diagonal. Spherical nanoparticles are isotropic, giving $\alpha_{xx}(\omega) = \alpha_{yy}(\omega) = \alpha_{zz}(\omega)$, where the polarizability can be written in terms of the dipolar Mie coefficient as $\alpha = 6\pi i a_1/k^3$. Anisotropic nanoparticles, such as disks, rods, and spheroids, likewise have a diagonal polarizability tensor in their principal axes, but with unequal components.

The total electric field at $\mathbf{x}_{\mathbf{n}\kappa}$ is $\mathbf{E}_{\mathbf{n}\kappa}(\omega)$, and is the sum of the incident $\mathbf{E}^0_{\mathbf{n}\kappa}$ and rescattered fields from the other other dipoles in the system, i.e.,

$$\bar{\boldsymbol{\alpha}}_\kappa^{-1}\cdot\mathbf{p}_{\mathbf{n}\kappa} = \mathbf{E}^0_{\mathbf{n}\kappa} + (-4\pi\omega^2)\sideset{}{'}\sum_{\mathbf{n}'\kappa'}\bar{\mathbf{G}}_0(\mathbf{x}_{\mathbf{n}\kappa},\mathbf{x}_{\mathbf{n}'\kappa'};\omega)\cdot\mathbf{p}_{\mathbf{n}'\kappa'}, \tag{2.22}$$

where the prime on the sum indicates the exclusion of the $\mathbf{n}' = \mathbf{n}$ term when $\kappa' = \kappa$. The free space Green's dyadic is given by $\bar{\mathbf{G}}_0(\mathbf{x},\mathbf{x}',\omega) = (-1/4\pi\omega^2)[(\omega/c)^2\bar{\mathbf{I}}+\nabla\nabla]e^{i(\omega/c)|\mathbf{x}-\mathbf{x}'|}/|\mathbf{x}-\mathbf{x}'|$. Considering Bloch wave excitations of the form $\boldsymbol{\Theta}_{\mathbf{n}\kappa} = \boldsymbol{\Theta}_{\mathbf{K}\kappa}e^{i\mathbf{K}\cdot\mathbf{x}_\mathbf{n}}e^{-i\omega t}$ with $\boldsymbol{\Theta}\in\{\mathbf{d},\mathbf{E}_0\}$, the coupled dipole equation of motion in Eq. 2.22 can be expressed in terms of the Bloch wave coefficients

$$\begin{aligned}\bar{\boldsymbol{\alpha}}_\kappa^{-1}\cdot\mathbf{p}_{\mathbf{K}\kappa}e^{i\mathbf{K}\cdot\mathbf{x}_\mathbf{n}} &= \mathbf{E}^0_{\mathbf{K}\kappa}e^{i\mathbf{K}\cdot\mathbf{x}_\mathbf{n}} + \sideset{}{'}\sum_{\mathbf{n}'\kappa'}\bar{\mathbf{G}}_0(\mathbf{x}_{\mathbf{n}\kappa},\mathbf{x}_{\mathbf{n}'\kappa'};\omega)\cdot\mathbf{p}_{\mathbf{K}\kappa'}e^{i\mathbf{K}\cdot\mathbf{x}_{\mathbf{n}'}}\\ &= \mathbf{E}^0_{\mathbf{K}\kappa}e^{i\mathbf{K}\cdot\mathbf{x}_\mathbf{n}} + \sideset{}{'}\sum_{\mathbf{n}'}\bar{\mathbf{G}}_0(\mathbf{x}_{\mathbf{n}\kappa},\mathbf{x}_{\mathbf{n}'\kappa})\cdot\mathbf{p}_{\mathbf{K}\kappa}e^{i\mathbf{K}\cdot\mathbf{x}_{\mathbf{n}'}}\\ &+ \sum_{\kappa'\neq\kappa}\sum_{\mathbf{n}'}\bar{\mathbf{G}}_0(\mathbf{x}_{\mathbf{n}\kappa},\mathbf{x}_{\mathbf{n}'\kappa'})\cdot\mathbf{p}_{\mathbf{K}\kappa'}e^{i\mathbf{K}\cdot\mathbf{x}_{\mathbf{n}'}},\end{aligned} \tag{2.23}$$

which can be rewritten as

$$\left[\bar{\boldsymbol{\alpha}}_\kappa^{-1} - \sideset{}{'}\sum_{\mathbf{n}'}\bar{\mathbf{G}}_0(\mathbf{x}_{\mathbf{n}\kappa},\mathbf{x}_{\mathbf{n}'\kappa})e^{i\mathbf{K}\cdot(\mathbf{x}_{\mathbf{n}'}-\mathbf{x}_\mathbf{n})}\right]\cdot\mathbf{p}_{\mathbf{K}\kappa} - \sum_{\kappa'\neq\kappa}\sum_{\mathbf{n}'}\bar{\mathbf{G}}_0(\mathbf{x}_{\mathbf{n}\kappa},\mathbf{x}_{\mathbf{n}'\kappa'})e^{i\mathbf{K}\cdot(\mathbf{x}_{\mathbf{n}'}-\mathbf{x}_\mathbf{n})}\cdot\mathbf{p}_{\mathbf{K}\kappa'} = \mathbf{E}^0_{\mathbf{K}\kappa}. \tag{2.24}$$

By defining the $(3s\times 1)$ vector $\mathbf{p}_\mathbf{K}$ by vertically stacking the s (3×1) $\mathbf{p}_{\mathbf{K}\kappa}$ vectors, the previous set of s coupled equations can be expressed as the single matrix equation

$$\bar{\bar{\boldsymbol{\Pi}}}^{-1}_\mathbf{K}(\omega)\mathbf{p}_\mathbf{K} = \mathbf{E}^0_\mathbf{K}, \tag{2.25}$$

where $\mathbf{E}^0_\mathbf{K}$ is the $(3s\times 1)$ incident field vector, and the inverse of the $(3s\times 3s)$ LPP response matrix is

$$\bar{\bar{\mathbf{\Pi}}}_{\mathbf{K}}^{-1}(\omega) = \begin{pmatrix} \bar{\boldsymbol{\alpha}}_1^{-1} - \bar{\mathbf{S}}_{11}(\mathbf{K},\omega) & -\bar{\mathbf{S}}_{12}(\mathbf{K},\omega) & \dots & -\bar{\mathbf{S}}_{1s}(\mathbf{K},\omega) \\ -\bar{\mathbf{S}}_{21}(\mathbf{K},\omega) & \bar{\boldsymbol{\alpha}}_2^{-1} - \bar{\mathbf{S}}_{22}(\mathbf{K},\omega) & & \vdots \\ \vdots & & \ddots & \\ -\bar{\mathbf{S}}_{s1}(\mathbf{K},\omega) & \dots & & \bar{\boldsymbol{\alpha}}_s^{-1} - \bar{\mathbf{S}}_{ss}(\mathbf{K},\omega) \end{pmatrix}. \tag{2.26}$$

The lattice $\bar{\mathbf{S}}_{\kappa\kappa}$ and interaction $\bar{\mathbf{S}}_{\kappa\kappa'}$ sum tensors, defined by

$$\begin{aligned} \bar{\mathbf{S}}_{\kappa\kappa}(\mathbf{K},\omega) &= \sum_{\mathbf{n}'}{}' \bar{\mathbf{G}}_0(\mathbf{x}_{\mathbf{n}\kappa}, \mathbf{x}_{\mathbf{n}'\kappa}; \omega) e^{i\mathbf{K}\cdot(\mathbf{x}_{\mathbf{n}'}-\mathbf{x}_{\mathbf{n}})} \\ \bar{\mathbf{S}}_{\kappa\kappa'}(\mathbf{K},\omega) &= \sum_{\mathbf{n}'} \bar{\mathbf{G}}_0(\mathbf{x}_{\mathbf{n}\kappa}, \mathbf{x}_{\mathbf{n}'\kappa'}; \omega) e^{i\mathbf{K}\cdot(\mathbf{x}_{\mathbf{n}'}-\mathbf{x}_{\mathbf{n}})}, \end{aligned} \tag{2.27}$$

account for intra- and inter-sublattice electromagnetic coupling, respectively. With these definitions, it is clear that $\bar{\mathbf{S}}_{\kappa\kappa'}(\mathbf{K}'+\mathbf{G},\omega) = \bar{\mathbf{S}}_{\kappa\kappa'}(\mathbf{K}',\omega)$, for $\kappa = \kappa'$ and $\kappa \neq \kappa'$, for $\mathbf{K}'$ within the first BZ and arbitrary reciprocal lattice vector $\mathbf{G}$. As an important consequence of this property, $\bar{\bar{\mathbf{\Pi}}}_{\mathbf{K}'+\mathbf{G}}(\omega) = \bar{\bar{\mathbf{\Pi}}}_{\mathbf{K}'}(\omega)$. The dispersive LPP quasinormal Bloch modes occur at $(\mathbf{K}',\omega)$ points where $\det\big[\bar{\bar{\mathbf{\Pi}}}_{\mathbf{K}'}^{-1}(\omega)\big] = 0$.

2.3 Wide-Field Transition Electric Field

In general, the transition current density associated with transitions between initial and final free electron states is given by [95]

$$\mathbf{J}_{fi}(\mathbf{x}) = \frac{i\hbar e}{2m}[\psi_f^*(\mathbf{x})\boldsymbol{\nabla}\psi_i^*(\mathbf{x}) - \psi_i(\mathbf{x})\boldsymbol{\nabla}\psi_f^*(\mathbf{x})] \tag{2.28}$$

with $\mathbf{J}_{fi}(\mathbf{x},t) = \mathbf{J}_{fi}(\mathbf{x})e^{-i(\varepsilon_i-\varepsilon_f)t}$. For a probing electron transitioning between incoming $\psi_i(\mathbf{x}) = L^{-3/2}e^{i\mathbf{k}_i\cdot\mathbf{x}}$ and outgoing $\psi_f(\mathbf{x}) = L^{-3/2}e^{i\mathbf{k}_f\cdot\mathbf{x}}$ plane wave states, the transition current density becomes [79, 80]

$$\mathbf{J}_{fi}(\mathbf{x}) = -(e\hbar/2mL^3)(2\mathbf{k}_i - \mathbf{q})e^{i\mathbf{q}\cdot\mathbf{x}}, \tag{2.29}$$

where $\mathbf{q} = \mathbf{k}_i - \mathbf{k}_f$ is the recoil wave vector and L is the box quantization length.

For a source represented by transition current density $\mathbf{J}_{fi}(\mathbf{x})$, the corresponding vacuum transition electric field is readily given by

$$\mathbf{E}_{fi}^0(\mathbf{x},\omega) = -4\pi i\omega \int d\mathbf{x}'\, \bar{\mathbf{G}}_0(\mathbf{x},\mathbf{x}',\omega)\cdot(L/v_i)\mathbf{J}_{fi}(\mathbf{x}') \tag{2.30}$$

with free space Green's dyadic $\bar{\mathbf{G}}_0(\mathbf{x}, \mathbf{x}', \omega) = (-1/4\pi\omega^2)[(\omega/c)^2\bar{\mathbf{I}} + \nabla\nabla]e^{i(\omega/c)|\mathbf{x}-\mathbf{x}'|}/|\mathbf{x}-\mathbf{x}'|$. Therefore, using the transition current density given by Eq. (2.29), we can obtain an analytical form for the wide-field transition electric field in direct space:

$$\begin{aligned}
\mathbf{E}^0_{fi}(\mathbf{x}, \omega) &= -4\pi i\omega\left(\frac{-1}{4\pi\omega^2}\right)\int d\mathbf{x}'\left[\left(\frac{\omega}{c}\right)^2\bar{\mathbf{I}} + \nabla\nabla\right]\frac{e^{i\frac{\omega}{c}|\mathbf{x}-\mathbf{x}'|}}{|\mathbf{x}-\mathbf{x}'|}\cdot\left(\frac{L}{v_i}\right)\mathbf{J}_{fi}(\mathbf{x}') \\
&= -\frac{ei\hbar}{2mL^2\omega v_i}\left[\left(\frac{\omega}{c}\right)^2\bar{\mathbf{I}} + \nabla\nabla\right]\cdot\left[2\mathbf{k}_i - \mathbf{q}\right]\int d\mathbf{x}'\frac{e^{i\frac{\omega}{c}|\mathbf{x}-\mathbf{x}'|}}{|\mathbf{x}-\mathbf{x}'|}e^{i\mathbf{q}\cdot\mathbf{x}'} \\
&= \frac{2i\pi\hbar e}{mv_iL^2\omega}\frac{e^{i\mathbf{q}\cdot\mathbf{x}}}{\left(\frac{\omega}{c}\right)^2 - q^2}\left[\left(\frac{\omega}{c}\right)^2\bar{\mathbf{I}} - \mathbf{q}\mathbf{q}\right]\cdot\left[2\mathbf{k}_i - \mathbf{q}\right] \\
&= \frac{2\pi ie\gamma_i}{k_iL^2\omega}\frac{(\omega/c)^2\bar{\mathbf{I}} - \mathbf{q}\mathbf{q}}{(\omega/c)^2 - q^2}\cdot(2\mathbf{k}_i - \mathbf{q})e^{i\mathbf{q}\cdot\mathbf{x}},
\end{aligned} \tag{2.31}$$

where $k_i = (\gamma_i m v_i)/\hbar$ and the Fourier transform of the scalar Green's function is given by $\int d\mathbf{x}'\,\frac{e^{i\frac{\omega}{c}|\mathbf{x}'-\mathbf{x}|}}{|\mathbf{x}'-\mathbf{x}|}\,e^{\pm i\mathbf{q}\cdot\mathbf{x}'} = -\frac{4\pi}{\frac{\omega^2}{c^2}-q^2}\,e^{\pm i\mathbf{q}\cdot\mathbf{x}}$. For periodic crystal excitations, we can write the transition electric at the site of each particle $\mathbf{x}_{\mathbf{n}\kappa}$ as [3]

$$\mathbf{E}^0_{fi,\mathbf{n}\kappa} = \frac{2\pi ie\gamma_i}{k_iL^2\omega}\frac{(\omega/c)^2\bar{\mathbf{I}} - \mathbf{q}\mathbf{q}}{(\omega/c)^2 - q^2}\cdot(2\mathbf{k}_i - \mathbf{q})e^{i\mathbf{q}\cdot\mathbf{x}_{\mathbf{n}\kappa}}. \tag{2.32}$$

In reciprocal space, the transition electric field becomes

$$\begin{aligned}
\mathbf{E}^0_{fi,\mathbf{K}\kappa} &= \frac{1}{N}\sum_{\mathbf{n}\kappa}e^{-i\mathbf{K}\cdot\mathbf{x}_\mathbf{n}}\,\mathbf{E}^0_{fi,\mathbf{n}\kappa} \\
&= \frac{2ie\pi\gamma_i}{k_iL^2\omega}\frac{1}{N}\sum_{\mathbf{n}\kappa}e^{-i\mathbf{K}\cdot\mathbf{x}_\mathbf{n}}\frac{(\omega/c)^2\bar{\mathbf{I}} - \mathbf{q}\mathbf{q}}{(\omega/c)^2 - q^2}\cdot(2\mathbf{k}_i - \mathbf{q})e^{i\mathbf{q}\cdot\mathbf{x}_{\mathbf{n}\kappa}} \\
&= \frac{2ie\pi\gamma_i}{k_iL^2\omega}\frac{(\omega/c)^2\bar{\mathbf{I}} - \mathbf{q}\mathbf{q}}{(\omega/c)^2 - q^2}\cdot(2\mathbf{k}_i - \mathbf{q})e^{i\mathbf{q}\cdot\mathbf{r}_\kappa}\delta_{\mathbf{q}\mathbf{K}},
\end{aligned} \tag{2.33}$$

or equivalently

$$\mathbf{E}^0_{fi,\mathbf{q}\kappa} = \frac{2ie\pi\gamma_i}{k_iL^2\omega}\frac{(\omega/c)^2\bar{\mathbf{I}} - \mathbf{q}\mathbf{q}}{(\omega/c)^2 - q^2}\cdot(2\mathbf{k}_i - \mathbf{q})e^{i\mathbf{q}\cdot\mathbf{r}_\kappa}. \tag{2.34}$$

When computing phonon induced dipole moments in Sec. 2.1.3, the discrete Fourier transform employed in the first line of Eq. (2.33) must be consistent with that used to derive the dynamical matrix. Eq. (2.33) is consistent with the dynamical matrix convention shown in Eq. (2.6) rather than Eq. (2.7), which differ by a factor of $e^{i\mathbf{q}\cdot\mathbf{r}_\kappa}$.

Having derived a formal expression for the vacuum transition electric field in reciprocal space, we now turn to the relativistic kinematic relations required to evaluate it explicitly in CGS units. In either the transmission or reflection geometry, the wave vector of the incident electron plane is given by $\mathbf{k}_i = k_i[\sin\theta_i \cos\phi_i, \sin\theta_i \sin\phi_i, \cos\theta_i]$, where $k_i = \gamma_i m v_i/\hbar$ with Lorentz factor $\gamma_i = [1-(v_i/c)^2]^{-1/2}$. In q-EELS experiments performed in the transmission geometry, the wave vector of the incident electron is typically normal to the sample plane (i.e., $\theta_i = 0°$), while HREELS experiments performed in the reflection geometry are typically conducted at near-grazing angles of incidence (i.e., $\theta_i \approx 80°$). The speed of the incident electron also varies between experiments, ranging from $v_i = 0.01c$ in HREELS experiments to $v_i \geq 0.3c$ in q-EELS.

For a given loss energy E_{if}, we can compute the Lorentz factor and wave vector magnitude of the outgoing plane wave state as $\gamma_f = \gamma_i - E_{if}/(mc^2)$, and $k_f = \gamma_f m v_f/\hbar$, respectively, where v_f is computed from the Lorentz factor $\gamma_f = [1-(v_f/c)^2]^{-1/2}$. Finally, we can construct the recoil wave vector $\mathbf{q} = \mathbf{k}_i - \mathbf{k}_f$, where the components of $\mathbf{k}_i$ are given above. The in-plane components of $\mathbf{q}$ (i.e., q_x and q_y), are independent variables corresponding to excitation of the target at specific in-plane Bloch vector $\mathbf{K}$. The only remaining variable to compute is $k_{f,z} = \pm\sqrt{k_f^2 - k_{f,x}^2 - k_{f,x}^2}$, where the sign of $k_{f,z}$ is determined by the scattering geometry. Once $\mathbf{q}$ is constructed, the Fourier coefficient of the transition electric field given by Eq. (2.34) can readily be computed.

To illustrate the selection rules at play in q-EELS and HREELS experiments, the components of the reciprocal-space vacuum transition electric field given by Eq. (2.34) computed across the first few Brillouin zones of graphene and a honeycomb plasmonic array are plotted in Figure 2.4. Since the Brillouin zones of the two materials span markedly different characteristic momentum scales, the polarization content of the probing transition electric field differs. Figures 2.4a,c display the normalized magnitude of the in-plane $\mathbf{E}^0_{fi} \cdot \hat{\mathbf{x}}$ (red) and out-of-plane $\mathbf{E}^0_{fi} \cdot \hat{\mathbf{z}}$ (blue) components of the electron's vacuum transition field at a loss energy of $E_{if} = 100$ meV versus $\mathbf{q}_{\|}$ along $\Gamma_0 - \mathrm{M}_1$ for graphene in transmission and reflection geometries. Solid and dotted lines represent the field components in the fully-retarded and quasistatic regimes, respectively. Except in the immediate vicinity of Γ_0, the transition electric field is predominantly in-plane polarized in Figure 2.4a. As evident in the inset, excitation via free space light is strongly limited in the IR by the light cone boundary. In contrast to transmission, the transition electric field in the reflection geometry evolves from being predominantly out-of-plane polarized in the first Brillouin zone to mostly in-plane polarized in the second Brillouin zone, as shown in Fig. 2.4b. Figures 2.4a,b also show that the fully-retarded transition electric field reduces to the quasistatic limit, as electromagnetic retardation effects are negligible for atomic crystals.

Sharing the same hexagonal lattice structure as graphene but with a lattice constant of $a = \sqrt{3}a_0$ where $a_0 = 460$ nm, Figure 2.4c,d show the normalized components of the electron's vacuum transition field at a loss energy of $E_{if} = 3$ eV versus $\mathbf{q}_{\|}$ along $\Gamma_0 - \mathrm{M}_2$ for a honeycomb plasmonic lattice in transmission and reflection geometries. Because the Brillouin zone of the honeycomb plasmonic lattice is orders of magnitude smaller than that of graphene, the polarization content of the transition electric field corresponds to that in the immediate vicinity of Γ_0 in Figure 2.4a,b. As a result, the transition electric field in the first Brillouin zone is predominantly out-of-plane polarized in the transmission geometry, the exact opposite of free space propagating light. In Figure 2.4c, it is evident that the electron probe, unlike free space light which is limited by the light cone boundary, can access momentum content lying well-beyond the first Brillouin zone. In addition, Figure 2.4c highlights the need to incorporate electromagnetic retardation effects when modeling the inelastic scattering of wide-field electron beams from plasmonic lattices, unlike in atomic crystals. In the reflection geometry, the transition electric field is entirely out-of-plane polarized from $\Gamma_0 - \mathrm{M}_2$, as shown in Figure 2.4d.

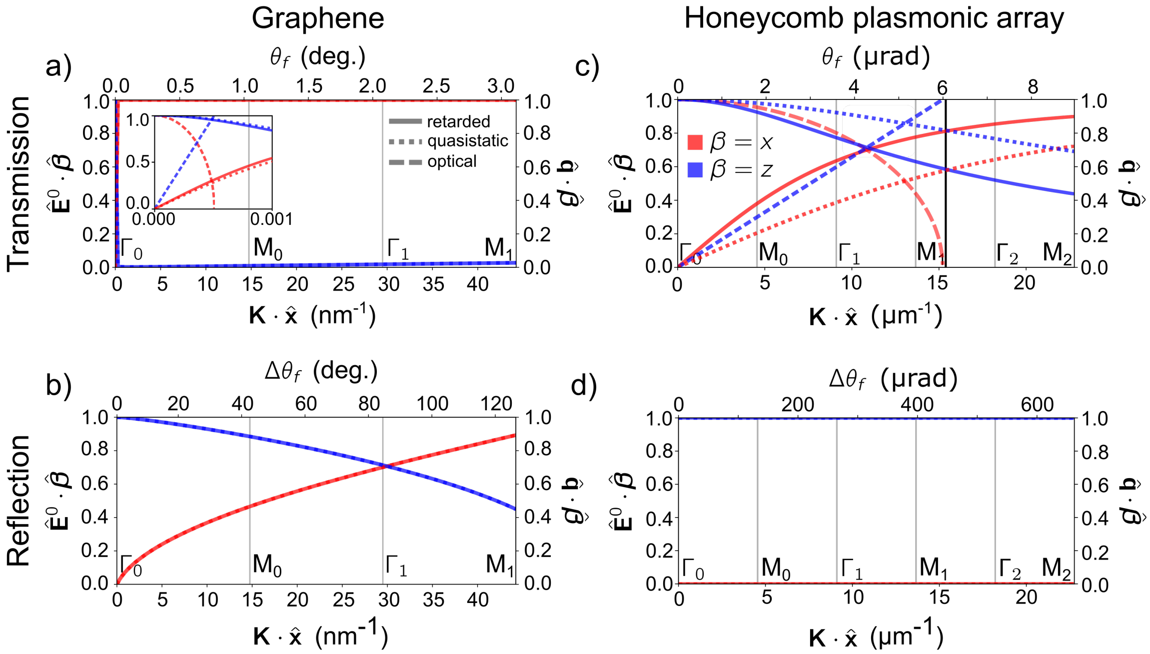

Figure 2.4: Components of the reciprocal space vacuum transition electric field computed across the Brillouin zones of graphene and a honeycomb plasmonic array. (a) and (b) show the normalized magnitude of the in-plane $\mathbf{E}^0_{fi} \cdot \hat{\mathbf{x}}$ (red) and out-of-plane $\mathbf{E}^0_{fi} \cdot \hat{\mathbf{z}}$ (blue) components of the electron's vacuum transition field at a loss energy of $E_{if} = 100$ meV versus $\mathbf{q}_{\|}$ along $\Gamma_0 - \mathrm{M}_1$ for graphene in transmission (a) and reflection (b) geometries. (c) and (d) show the normalized components of the electron's vacuum transition field at a loss energy of $E_{if} = 3$ eV versus $\mathbf{q}_{\|}$ along $\Gamma_0 - \mathrm{M}_2$ for a honeycomb plasmonic lattice with $a = 460\sqrt{3}$ nm in transmission (c) and reflection (d) geometries. Solid and dotted lines represent the field components in the fully-retarded and quasistatic regimes, respectively, while the dashed lines indicate the components of free space plane wave light $\mathbf{E}^0 = E_0\hat{\boldsymbol{\epsilon}}(\mathbf{k})$. In panels (a) and (c), $\theta_i = 0°$, and $\theta_i = 80°$ and $\theta_i = 45°$ in panels (b) and (d). Both panels (b) and (d) were computed with $v_i = 0.01c$, while $v_i = 0.3$ and $v_i = 0.7c$ in panels (a) and (d).

In Figure 2.5, the polarization content of the electron's vacuum transition field at different electron speeds v_i computed from $\Gamma_0 - \mathrm{M}_2$ for a honeycomb plasmonic array with the same dimensions as Figure 2.4 is shown. The loss energy and wave vector of the incident electron are fixed at $E_{if} = 3$ eV and $\theta_i = 0°$, respectively. As evident in Figure 2.5, the polarization content of the transition electric field is strongly dependent on the electron speed. The electron speed, like the scattering geometry, is a tunable experimental parameter that allows selective coupling to material modes of interest.

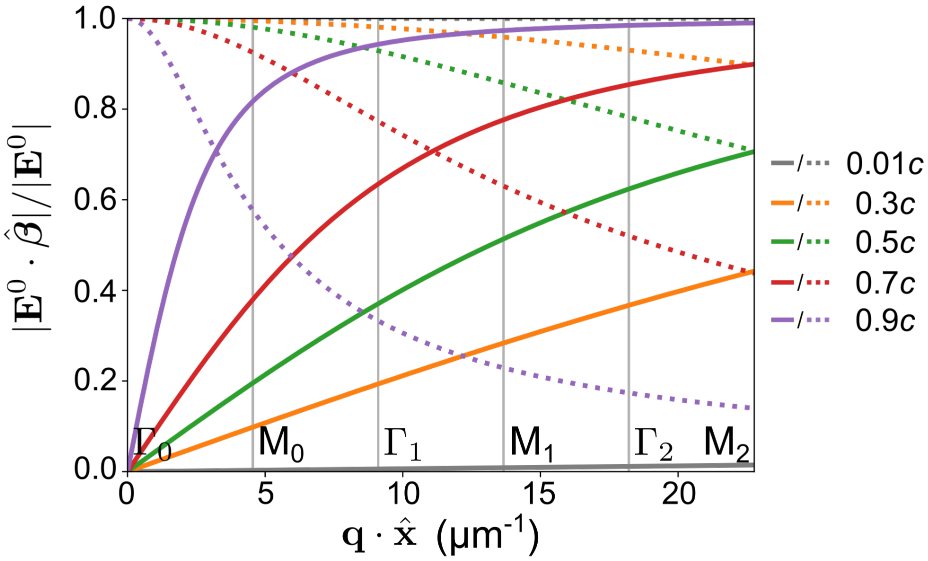

Figure 2.5: Dispersion of the electron's vacuum transition field at different electron speeds v_i computed from $\Gamma_0 - \mathrm{M}_2$ for a honeycomb plasmonic array. The normalized magnitude of the in-plane $\mathbf{E}^0_{fi} \cdot \hat{\mathbf{x}}$ (solid) and out-of-plane $\mathbf{E}^0_{fi} \cdot \hat{\mathbf{z}}$ (dotted) components are plotted as a function of $\mathbf{q} \cdot \hat{\mathbf{x}}$ at loss energy $E_{if} = 3$ eV in the transmission geometry. The incident wave vector is fixed at $\theta_i = 0°$, and the M point is defined with $a = 460\sqrt{3}$ nm.

2.3.1 Quasistatic Transition Electric Field

As mentioned above, electromagnetic retardation effects are negligible for atomic crystals, like graphene. Therefore, the inelastic electron scattering from atomic crystals can be treated in the quasistatic limit. This section reviews how to compute the quasistatic analog of the transition electric field given by Eq. (2.34), which can also be obtained from Eq. (2.34) in the limit $c \to \infty$. In the quasistatic limit, the transition electric field is obtained from the transition charge density $\rho_{fi}(\mathbf{x}) = -e\,\psi_f^*(\mathbf{x})\,\psi_i(\mathbf{x})$ by way of the scalar potential. The scalar potential in reciprocal space is given by

$$\begin{aligned}
\phi_{fi}^0(\mathbf{K},\omega) &= (L/v_i)\int d\mathbf{x}e^{-i\mathbf{K}\cdot\mathbf{x}}\int d\mathbf{x}' G_0(\mathbf{x},\mathbf{x}')\rho_{fi}(\mathbf{x}',\omega) \\
&= (L/v_i)\int d\mathbf{x}e^{-i\mathbf{K}\cdot\mathbf{x}}\int d\mathbf{x}'\frac{1}{|\mathbf{x}-\mathbf{x}'|}\rho_{fi}(\mathbf{x}',\omega) \\
&= (L/v_i)\int d\mathbf{x}'\left[\int d\mathbf{x}e^{-i\mathbf{K}\cdot\mathbf{x}}\frac{1}{|\mathbf{x}-\mathbf{x}'|}\right]\rho_{fi}(\mathbf{x}',\omega) \\
&= (L/v_i)\int d\mathbf{x}'\left[\frac{4\pi e^{-i\mathbf{K}\cdot\mathbf{x}'}}{k^2}\right]\rho_{fi}(\mathbf{x}',\omega) \\
&= \frac{4\pi}{k^2}\frac{L}{v_i}\,\rho_{fi}(\mathbf{K},\omega),
\end{aligned} \tag{2.35}$$

where $G_0(\mathbf{x},\mathbf{x}') = \frac{1}{|\mathbf{x}-\mathbf{x}'|}$ is the electrostatic Green's function. The quasistatic transition electric field in reciprocal space is related to the scalar potential via

$$\begin{aligned}
\mathbf{E}_{fi}^0(\mathbf{K},\omega) &= \int d\mathbf{x}\,\mathbf{E}_{fi}^0(\mathbf{x},\omega)e^{-i\mathbf{K}\cdot\mathbf{x}} \\
&= -\int d\mathbf{x}\left[\nabla\phi_{fi}^0(\mathbf{x},\omega)\right]e^{-i\mathbf{K}\cdot\mathbf{x}} \\
&= \int d\mathbf{x}\,\phi_{fi}^0(\mathbf{x},\omega)\left[\nabla e^{-i\mathbf{K}\cdot\mathbf{x}}\right] \\
&= (-i\mathbf{K})\int d\mathbf{x}\,\phi_{fi}^0(\mathbf{x},\omega)e^{-i\mathbf{K}\cdot\mathbf{x}} \\
&= (-i\mathbf{K})\phi_{fi}^0(\mathbf{K},\omega),
\end{aligned} \tag{2.36}$$

Therefore, the quasistatic transition electric field, in general, can be written as

$$\mathbf{E}_{fi}^0(\mathbf{K},\omega) = (-i\mathbf{K})\frac{4\pi}{k^2}\frac{L}{v_i}\,\rho_{fi}(\mathbf{K},\omega), \tag{2.37}$$

or for periodic crystal excitations, the transition electric at the site of each particle $\mathbf{x}_{\mathbf{n}\kappa}$ is given by

$$\mathbf{E}_{fi,\mathbf{K}}^0 = (-i\mathbf{K})\frac{4\pi}{k^2}\frac{L}{v_i}\,\rho_{fi,\mathbf{K}}. \tag{2.38}$$

For a probing electron transitioning between incoming $\psi_i(\mathbf{x}) = L^{-3/2}e^{i\mathbf{k}_i\cdot\mathbf{x}}$ and outgoing $\psi_f(\mathbf{x}) = L^{-3/2}e^{i\mathbf{k}_f\cdot\mathbf{x}}$ plane wave states, the transition current density is given by $\rho_{fi}(\mathbf{x}) =$

$-eL^{-3}e^{i\mathbf{q}\cdot\mathbf{x}}$, or $\rho_{fi,\mathbf{x}_{\mathbf{n}\kappa}} = -eL^{-3}e^{i\mathbf{q}\cdot\mathbf{x}_{\mathbf{n}\kappa}}$. In reciprocal space, this becomes

$$\begin{aligned}\rho_{fi,\mathbf{K}\kappa} &= \frac{1}{N}\sum_{\mathbf{n}\kappa} e^{-i\mathbf{K}\cdot\mathbf{x}_{\mathbf{n}}}\,\rho_{fi,\mathbf{n}\kappa} \\ &= -\frac{e}{NL^3}\sum_{\mathbf{n}\kappa} e^{-i\mathbf{K}\cdot\mathbf{x}_{\mathbf{n}}}\,e^{i\mathbf{q}\cdot\mathbf{x}_{\mathbf{n}\kappa}} \\ &= -\frac{e}{L^3}e^{i\mathbf{q}\cdot\mathbf{r}_\kappa}\delta_{\mathbf{q}\mathbf{K}}.\end{aligned} \tag{2.39}$$

Inserting Eq. 2.39 into Eq. 2.38, we can write the quasistatic transition electric field as

$$\mathbf{E}^0_{fi,\mathbf{K}} = \frac{4\pi ie}{L^3}\frac{L}{v_i}\frac{\mathbf{K}}{K^2}e^{i\mathbf{q}\cdot\mathbf{r}_\kappa}\delta_{\mathbf{q}\mathbf{K}}, \tag{2.40}$$

or equivalently,

$$\mathbf{E}^0_{fi,\mathbf{q}} = \frac{4\pi ie}{L^3}\frac{L}{v_i}\frac{\mathbf{q}}{q^2}e^{i\mathbf{q}\cdot\mathbf{r}_\kappa}. \tag{2.41}$$

This is the quasistatic version of Eq. (2.34). The procedure outlined in this section is general, and it is the starting point for obtaining the transition electric field associated with more sophisticated phase-structured incident electron beams in the quasistatic limit, such as electron pinwheel [2] or Bessel beams.

2.4 Wide-Field EEL Observable: The Double-Differential Cross Section

To derive the double-differential cross section (DDCS), we must first compute the frequency-resolved EEL transition rate in reciprocal space. In previous work, it was shown that the state- and frequency-resolved EEL transition rate stemming from Fermi's Golden rule can be written as [80, 96]

$$w_{fi}(\omega) = -\frac{8\pi}{\hbar}\int d\mathbf{x}\,d\mathbf{x}'\,\mathrm{Im}[\mathbf{J}^*_{fi}(\mathbf{x})\cdot\bar{\mathbf{G}}(\mathbf{x},\mathbf{x}',\omega)\cdot\mathbf{J}_{fi}(\mathbf{x}')]\delta(\omega-\varepsilon_{if}), \tag{2.42}$$

where $\bar{\mathbf{G}}(\mathbf{x},\mathbf{x}',\omega) = -4\pi\omega^2\sum_{\mathbf{n}\kappa}\sum_{\mathbf{n}'\kappa'}\bar{\mathbf{G}}_0(\mathbf{x},\mathbf{x}_{\mathbf{n}\kappa},\omega)\cdot\bar{\mathbf{\Pi}}(\mathbf{x}_{\mathbf{n}\kappa},\mathbf{x}_{\mathbf{n}'\kappa'},\omega)\cdot\bar{\mathbf{G}}_0(\mathbf{x}_{\mathbf{n}'\kappa'},\mathbf{x}',\omega)$ is the target's induced Green's function with $\bar{\mathbf{\Pi}}(\mathbf{x}_{\mathbf{n}\kappa},\mathbf{x}_{\mathbf{n}'\kappa'},\omega) = [\bar{\boldsymbol{\alpha}}^{-1}(\omega)-(-4\pi\omega^2)\bar{\mathbf{G}}_0(\mathbf{x}_{\mathbf{n}\kappa},\mathbf{x}_{\mathbf{n}'\kappa'},\omega)]^{-1}$.

In reciprocal space, the EEL transition rate becomes

$$\begin{aligned}
\omega_{fi}(\omega) &= -\frac{8\pi}{\hbar}\int d\mathbf{x}\,d\mathbf{x}'\mathrm{Im}[\mathbf{J}^*_{fi}(\mathbf{x})\cdot\bar{\mathbf{G}}(\mathbf{x},\mathbf{x}',\omega)\cdot\mathbf{J}_{fi}(\mathbf{x}')]\delta(\omega-\varepsilon_{if}) \\
&= \frac{-8\pi}{\hbar}\mathrm{Im}\Bigg\{\,\Bigg[(-4\pi\omega^2)\int d\mathbf{x}\,\mathbf{J}^*_{fi}(\mathbf{x})\cdot\sum_{\mathbf{n}\kappa}\bar{\mathbf{G}}_0(\mathbf{x},\mathbf{x}_{\mathbf{n}\kappa},\omega)\cdot\Bigg[\sum_{\mathbf{n}'\kappa'}\bar{\boldsymbol{\Pi}}(\mathbf{x}_{\mathbf{n}\kappa},\mathbf{x}_{\mathbf{n}'\kappa'},\omega) \\
&\quad\cdot\int d\mathbf{x}'\,\bar{\mathbf{G}}_0(\mathbf{x}_{\mathbf{n}'\kappa'},\mathbf{x}',\omega)\cdot\mathbf{J}_{fi}(\mathbf{x}')\Bigg]\delta(\omega-\varepsilon_{if}) \\
&= \frac{2}{\hbar}\left(\frac{v_i}{L}\right)^2\mathrm{Im}\Bigg\{\,\sum_{\mathbf{n}\kappa}\mathbf{E}^{0*}_{fi,\mathbf{n}\kappa}\cdot\Bigg[\sum_{\mathbf{n}'\kappa'}\bar{\boldsymbol{\Pi}}(\mathbf{x}_{\mathbf{n}\kappa},\mathbf{x}_{\mathbf{n}'\kappa'},\omega)\cdot\mathbf{E}^{0}_{fi,\mathbf{n}'\kappa'}\Bigg]\Bigg\}\delta(\omega-\varepsilon_{if}) \\
&= \frac{2}{\hbar}\left(\frac{v_i}{L}\right)^2\mathrm{Im}\Bigg\{\,\sum_{\mathbf{n}\kappa}\mathbf{E}^{0*}_{fi,\mathbf{n}\kappa}\cdot\mathbf{p}_{\mathbf{n}\kappa}\Bigg\}\delta(\omega-\varepsilon_{if}) \\
&= \frac{2}{\hbar}\left(\frac{v_i}{L}\right)^2\mathrm{Im}\Bigg\{\,\sum_{\mathbf{n}\kappa}\sum_{\mathbf{K}}\mathbf{E}^{0*}_{fi,\mathbf{K}\kappa}e^{-i\mathbf{K}\cdot\mathbf{x}_{\mathbf{n}}}\cdot\sum_{\mathbf{K}'}\mathbf{p}_{\mathbf{K}'\kappa}e^{i\mathbf{K}'\cdot\mathbf{x}_{\mathbf{n}}}\Bigg\}\delta(\omega-\varepsilon_{if}) \\
&= \frac{2}{\hbar}\left(\frac{v_i}{L}\right)^2\mathrm{Im}\Bigg\{\,\sum_{\kappa}\sum_{\mathbf{K}}\sum_{\mathbf{K}'}\mathbf{E}^{0*}_{fi,\mathbf{K}\kappa}\cdot\mathbf{p}_{\mathbf{K}'\kappa}\sum_{\mathbf{n}}e^{i(\mathbf{K}'-\mathbf{K})\cdot\mathbf{x}_{\mathbf{n}}}\Bigg\}\delta(\omega-\varepsilon_{if}) \\
&= \frac{2}{\hbar}\left(\frac{v_i}{L}\right)^2\mathrm{Im}\Bigg\{\,\sum_{\kappa}\sum_{\mathbf{K}}\sum_{\mathbf{K}'}\mathbf{E}^{0*}_{fi,\mathbf{K}\kappa}\cdot\mathbf{p}_{\mathbf{K}'\kappa}N\delta_{\mathbf{K},\mathbf{K}'}\Bigg\}\delta(\omega-\varepsilon_{if}) \\
&= N\frac{2}{\hbar}\left(\frac{v_i}{L}\right)^2\mathrm{Im}\Bigg\{\,\sum_{\kappa}\sum_{\mathbf{K}}\mathbf{E}^{0*}_{fi,\mathbf{K}\kappa}\cdot\mathbf{p}_{\mathbf{K}\kappa}\Bigg\}\delta(\omega-\varepsilon_{if}),
\end{aligned} \tag{2.43}$$

where $\mathbf{E}^{0*}_{fi,\mathbf{n}\kappa}$ is given by Eq. (2.30) and $\mathbf{p}_{\mathbf{n}\kappa} = \sum_{\mathbf{n}'\kappa'}\bar{\boldsymbol{\Pi}}(\mathbf{x}_{\mathbf{n}\kappa},\mathbf{x}_{\mathbf{n}'\kappa'},\omega)\cdot\mathbf{E}^{0}_{fi,\mathbf{n}'\kappa'}$ is the induced dipole moment of the κth atom in direct space. The inverse Fourier transforms are given by $\mathbf{E}^{0*}_{fi,\mathbf{n}\kappa} = \sum_{\mathbf{K}}\mathbf{E}^{0*}_{fi,\mathbf{K}\kappa}e^{-i\mathbf{K}\cdot\mathbf{x}_{\mathbf{n}}}$ and $\mathbf{p}_{\mathbf{n}\kappa} = \sum_{\mathbf{K}}\mathbf{p}_{\mathbf{K}\kappa}e^{-i\mathbf{K}\cdot\mathbf{x}_{\mathbf{n}}}$. The explicit functional form of $\mathbf{E}^{0*}_{fi,\mathbf{K}\kappa}$ is given in Sec. 2.3, and explicit functional forms of $\mathbf{p}_{\mathbf{K}\kappa}$ for phonons in atomic crystals and LPPs in plasmonic lattices are given in Sec. 2.1.3 and Sec. 2.2, respectively.

For transitions between plane wave electron states, the relevant observable is the scattering cross section. The cross section is obtained by summing over final electron states and dividing by the incoming plane wave flux $\hbar k_i/mL^3$. In the limit $\sum_{\mathbf{k}_f}\to(L/2\pi)^3\int d\mathbf{k}_f$, the total frequency-resolved scattering cross section becomes [80]

$$\sigma(\omega) = \frac{mL^3}{\hbar k_i}\left(\frac{L}{2\pi}\right)^3\int d\Omega_f\,k_f^2\,dk_f\,w_{fi}(\omega). \tag{2.44}$$

After integration over frequency, we can write the angle-resolved scattering cross section as

$$\begin{aligned}\frac{\partial\sigma}{\partial\Omega_f} &= \frac{mL^3}{\hbar k_i}\left(\frac{L}{2\pi}\right)^3\int d\omega\, k_f^2\, dk_f\, w_{fi}(\omega)\\ &= -\frac{mL^3}{\hbar k_i}\left(\frac{L}{2\pi}\right)^3\int d\omega\, dE_{if}\left(\frac{m}{\hbar^2 k_f}\right)k_f^2 w_{fi}(\omega),\end{aligned} \tag{2.45}$$

where $dE_{if} = -(\hbar^2/m)k_f dk_f$ and $\Omega_f = \sin\theta_f d\theta_f d\phi_f$. Finally, by making use of Eq. (2.43), we can write the DDCS as

$$\begin{aligned}\frac{\partial^2\sigma}{\partial E_{if}\partial\Omega_f} &= -\frac{m^2L^3}{\hbar^3}\left(\frac{L}{2\pi}\right)^3\left(\frac{k_f}{k_i}\right)\int d\omega\, w_{fi}(\omega)\\ &= -\frac{2m^2L^3}{\hbar^4}\left(\frac{L}{2\pi}\right)^3\left(\frac{k_f}{k_i}\right)\left(\frac{v_i}{L}\right)^2\mathrm{Im}\left\{\sum_{\kappa}\sum_{\mathbf{K}}\mathbf{E}^{0*}_{fi,\mathbf{K}\kappa}\cdot\mathbf{p}_{\mathbf{K}\kappa}\right\}\\ &= -\frac{1}{\pi}\left(\frac{mv_iL^2}{2\pi\hbar^2}\right)^2\left(\frac{k_f}{k_i}\right)\mathrm{Im}\left\{\sum_{\kappa}\mathbf{E}^{0*}_{fi,\mathbf{q}\kappa}\cdot\mathbf{p}_{\mathbf{q}\kappa}\right\},\end{aligned} \tag{2.46}$$

where, based on Eq. (2.33), $\mathbf{E}^0_{fi,\mathbf{K}\kappa} = \delta_{\mathbf{qK}}\mathbf{E}^0_{fi,\mathbf{q}\kappa}$. The DDCS computed along $\Gamma-$M for both phonons in graphene and LPPs in a honeycomb plasmon array are presented in Chapter 4, and in Chapter 5, the DDCS computed along $\Gamma-$ K for phonons in hBN is shown. In the quasistatic limit appropriate to atomic crystals, Eq. (2.19) can be inserted into Eq. (2.43) to obtain the following expression for the state- and frequency-resolved EEL transition rate

$$w_{fi}^{\mathrm{loss}} = N\frac{2}{\hbar}\left(\frac{v_i}{L}\right)^2\mathrm{Im}\sum_{\lambda}\sum_{\mathbf{K}}\frac{|F_\lambda(\mathbf{K})|^2}{\omega_\lambda^2-\omega_{if}(\omega_{if}+i\eta)}, \tag{2.47}$$

where $F_\lambda(\mathbf{K}) = \sum_\kappa \boldsymbol{\xi}^*_{\lambda\kappa}\cdot M_\kappa^{-1/2}\cdot e\bar{\mathbf{Z}}_\kappa(\mathbf{K})\cdot\mathbf{E}^0_{fi,\mathbf{K}\kappa}$. In the case of a probing electron transitioning between incoming and outgoing plane wave states, the quasistatic transition electric field $\mathbf{E}^0_{fi,\mathbf{K}\kappa}$ is given by Eq. (2.40). For more sophisticated incident beams, such as electron pinwheel [2] and Bessel beams, Eq. (2.47) can likewise be used to compute the EEL transition rate by simply replacing $\mathbf{E}^0_{fi,\mathbf{K}\kappa}$.

Chapter 3

OPTICAL CONTROL OVER THERMAL DISTRIBUTIONS IN TOPOLOGICALLY TRIVIAL AND NON-TRIVIAL PLASMON LATTICES.

- Bourgeois, M. R., Rossi, A. W., Khorasani, S., Masiello, D. J. (2022). Optical control over thermal distributions in topologically trivial and non-trivial plasmon lattices. *ACS Photonics*, 9(11), 3656-3667.

3.1 Abstract

Emergent from the discrete spatial periodicity of plasmonic arrays, surface lattice resonances (SLRs) are characterized as dispersive, high quality polaritonic modes that can be selectively excited at specific points in their photonic band structure by plane-wave light of varying frequency, polarization, and angle of incidence. Room temperature Bose-Einstein condensation of exciton polaritons, lasing, and nonlinear matter-wave physics have all found origins in SLR systems, but to date little attention has been paid to their thermal behavior. Here, we combine analytical theory and numerical simulation to investigate the photothermal properties of SLRs in periodic 1D and 2D arrays of plasmonic nanoparticles coupled to each other and to the electromagnetic far-field via transverse radiation. Specifically, we demonstrate how to create steady-state SLR thermal gradients spanning from the nanoscale to hundreds of microns that are actively controllable using light in spite of heat diffusion. We also demonstrate the surprising ability to localize thermal gradients at the lattice edges in topologically non-trivial SLR dimer lattices, thereby establishing a class of extraordinary thermal responses that are unconventional in ordinary materials. This work exposes a new direction in thermoplasmonics that has only just now begun to be explored.

3.2 Introduction

The ability to control heat flow and thus temperature at both nano- ($\lesssim 100$ nm) and micron- ($\sim 1-100$ μm) scale dimensions has important implications for a host of applications, including photothermal catalysis[97–100], heat-assisted magnetic recording for improved data storage [101, 102], thermal encoding of encrypted data [103–105], bolometry [106, 107], photothermal cancer therapy [108, 109], and photothermal biosensors for COVID-19 [110], among many others [111, 112]. In each of these applications, photothermal control is derived from the interaction of light with noble metal nanoparticles (NPs) through excitation of their localized surface plasmon (LSP) resonances characterized by strong optical extinction. Of this extinction, the nonradiative component ultimately leads to both NP and local environment heating due to thermal diffusion [113]. Photothermal conversion via LSP decay has been studied in detail at the single NP level [114, 115] as well as in assemblies of near-field-coupled NPs, demonstrating temperature increases beyond those found in individual particles [116–118]. Further ability to create and detect modified thermal profiles where heat is preferentially deposited into specific NPs within a nano-scale assembly using far-field optical excitation has also been predicted [119] and experimentally characterized [120, 121].

In 2013, Baffou et al. [20] showed that 2D periodic arrays of plasmonic NPs optically excited at the single particle LSP energy exhibit distinct spatial thermal profiles resulting from the interplay between heating via single particle absorption and from thermal coupling between all particles in the array. Yet it is well-known that periodic arrays of plasmonic NPs can host surface lattice resonances (SLRs) arising from hybridization of the diffractive photonic modes inherited from the array periodicity [122] with the LSPs supported by each NP in the array [28, 123, 124]. The prospects of SLR-based systems for photothermal applications is intriguing. On the one hand, optimization of such systems favors larger NP sizes to enable scattering-induced particle-particle coupling, which decreases the proportion of nonradiative decay to the overall LSP decay rate. At the same time, however, collective diffractive coupling at the center and edges of the Brillouin zone creates standing waves within the lattice leading to strongly-enhanced absorption at the SLR energies [124]. Furthermore, non-Bravais lattices with > 1 NP per unit cell [11, 125–128] open the possibility for modes exhibiting hierarchical excitation and thermal spatial profiles on both the unit cell and array length scales. Careful tuning of intra- and inter-unit-cell interactions in non-Bravais NP arrays can also, under suitable conditions, lead to the existence of topologically protected hybrid modes that are strongly localized to the array edges [129, 130], which could potentially be exploited to achieve thermal profiles that are similarly biased towards the array edges.

Using analytical theory and numerical calculations, in this article we investigate steady-state photothermal heating in diffractively coupled Bravais and non-Bravais plasmonic NP arrays and show how the illumination conditions can be used to actively tune thermal profiles at both nano- ($\lesssim 100$ nm) and micron- ($\sim 1 - 100$ μm) scales. Particular attention is paid to array band structures arising from discrete translational symmetry to understand the role played by strong electromagnetic coupling during optical absorption. Nanoscale control over thermal gradients within each unit cell is also demonstrated by leveraging symmetry-dependent optical selection rules for homodimer and heterodimer non-Bravais unit cells. Finally, we raise the intriguing prospect of exploiting topologically protected edge modes to localize photothermal heating to finite array edges. Importantly, we employ a realistic treatment of material losses and long-range particle-particle coupling inherent to LSP-based systems. Taken together, this work outlines a practical set of structure-function relationships relevant to designing realistic plasmonic lattice systems for chemical, biological, medical, engineering, and technological applications.

3.3 Photothermal Properties of 1D Bravais and Non-Bravais Plasmonic Lattices

3.3.1 Bravais Arrays

The emergence of SLRs in plasmonic arrays requires NPs that are large enough to scatter appreciably, thereby providing a mechanism to lock light into the lattice plane and induce long-range dipole-dipole coupling spanning the entire lattice domain. Yet plasmonic NPs also absorb optical energy, ultimately dissipating it to heat and causing a temperature rise within the lattice and its surrounding environment. By balancing these two

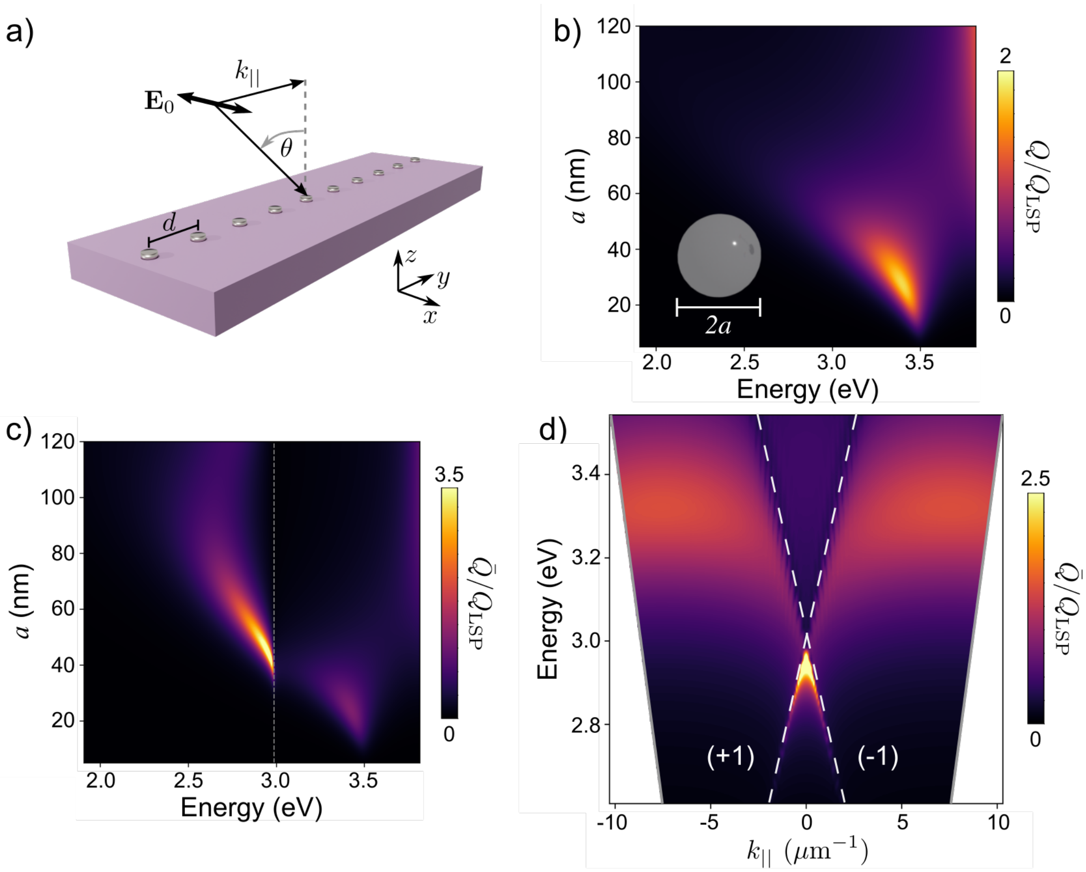

Figure 3.1: Electromagnetic absorption by 1D monomer array. (a) Array scheme indicating $x-$polarized incident radiation propagating along the $y-$direction. (b) Normalized heat power absorption Q/Q_{LSP} spectra for individual Ag nanospheres as a function of radius a. (c) Normalized per-particle heat power absorption $\bar{Q}/Q_{\mathrm{LSP}}$ spectra for a 1D array of NPs with periodicity $d = 415$ nm as a function of radius a. The vertical dashed gray line marks the position of the Γ point Rayleigh anomaly near 3.0 eV. (d) $\bar{Q}/Q_{\mathrm{LSP}}$ for a 1D array of 90 nm diameter Ag nanospheres with periodicity $d = 415$ nm as a function of the Bloch vector $k_{\|}$. All heat power spectra are normalized by the heat power absorbed by an $a = 45$ nm Ag sphere at the dipolar LSP energy Q_{LSP} at the same incident field intensity. Color bar maxima values in panels (c) and (d) were selected for overall plot visibility and are not the maximum values attained in the plotted domains. The maximum $\bar{Q}(k_{\|} = 0, \omega)/Q_{\mathrm{LSP}}$ value in both panels is ~ 4.1.

contributions—scattering and absorption—here we demonstrate the ability to create and manipulate long-range thermal gradients in SLR arrays that are actively controllable in steady-state through variation of the parameters of the incident light field (i.e., frequency, direction, and polarization), despite the effects of heat diffusion.

Figure 3.1a illustrates a 1D plasmonic NP lattice composed of a periodic array of Ag nanospheres, each modeled as an electric dipole absorber/scatterer with dipole moment $\mathbf{p}_i$ coupled to all other nanosphere dipoles $\mathbf{p}_j$ via the relay tensor

$$\overleftrightarrow{\mathbf{G}}(\mathbf{r}_i,\mathbf{r}_j,\omega)=\frac{e^{ikR_{ij}}}{R_{ij}}\left[\left(1+\frac{i}{kR_{ij}}-\frac{1}{(kR_{ij})^2}\right)\overleftrightarrow{\mathbf{I}}+\left(-1-\frac{3i}{kR_{ij}}+\frac{3}{(kR_{ij})^2}\right)\hat{\mathbf{R}}_{ij}\hat{\mathbf{R}}_{ij}\right], \tag{3.1}$$

where $\mathbf{R}_{ij}=\hat{\mathbf{R}}_{ij}R_{ij}$ is the vector connecting dipoles i and j separated by the distance $R_{ij}=|\mathbf{r}_i-\mathbf{r}_j|$ and $k=\omega\sqrt{\varepsilon}/c=2\pi\sqrt{\varepsilon}/\lambda$ with background refractive index $\sqrt{\varepsilon}$. Though we retain this ε-dependence in all equations, we use a background medium refractive index of unity in all following calculations. In matrix form, the coupled dipole equations for an N dipole system can be organized into the linear system of equations [131, 132]

$$\overleftrightarrow{\mathbf{A}}(\omega)\mathbf{P}(\omega)=\mathbf{E}_0(\omega) \tag{3.2}$$

with $3N\times 3N$ matrix $\overleftrightarrow{\mathbf{A}}(\omega)$ consisting of 3×3 matrix blocks $\overleftrightarrow{\mathbf{A}}_{ij}(\omega)=\alpha^{-1}(\omega)\overleftrightarrow{\mathbb{I}}_{ij}-\overleftrightarrow{\mathbb{G}}_{ij}(\omega)$ connecting NPs i and j. Here, $\alpha^{-1}(\omega)\overleftrightarrow{\mathbb{I}}_{ij}=\overleftrightarrow{\alpha}^{-1}(\omega)\delta_{ij}=\alpha^{-1}(\omega)\overleftrightarrow{\mathbf{I}}\delta_{ij}$ is a function of the isotropic dipole polarizability $\alpha(\omega)=i(3/2k^3)a_1(\omega)$ derived from the $\ell=1$ Mie scattering coefficient $a_1(\omega)$. The purely off-diagonal interaction matrix $\overleftrightarrow{\mathbb{G}}_{ij}(\omega)=(k^2/\varepsilon)\overleftrightarrow{\mathbf{G}}(\mathbf{r}_i,\mathbf{r}_j,\omega)(1-\delta_{ij})$ accounts for dipole-dipole coupling, and $\mathbf{P}(\omega)$ and $\mathbf{E}_0(\omega)$ are $3N\times 1$ column vectors containing the Cartesian components of the N induced dipole moments $\mathbf{p}_i(\omega)$ and excitation field values $\mathbf{E}_0(\mathbf{r}_i,\omega)$, respectively, at positions $\mathbf{r}_1,\ldots,\mathbf{r}_N$.

We first consider an isolated Ag nanosphere with dipolar absorption cross section $\sigma_{\mathrm{abs}}(\omega)=(4\pi k/\sqrt{\varepsilon})\mathrm{Im}\,\alpha(\omega)-(8\pi k^4/3\varepsilon^2)|\alpha(\omega)|^2$, which dictates the heat power $Q(\omega)=\sigma_{\mathrm{abs}}(\omega)I_0=\sigma_{\mathrm{abs}}(\omega)(c\sqrt{\varepsilon}/8\pi)|\mathbf{E}_0(\mathbf{r},\omega)|^2$ absorbed under incident plane wave intensity I_0. Figure 3.1b shows normalized heat power absorption Q/Q_{LSP} spectra as a function of the NP radius a, where Q_{LSP} is the maximum heat power absorbed for an $a=45$ nm NP under identical I_0. Note that this ratio of heat powers is proportional to $\sigma_{\mathrm{abs}}(\omega)$ and does not depend on I_0. Due to the onset of dynamic depolarization and radiation damping arising from a significant scattering contribution [133], we see that Q/Q_{LSP} increases initially for small radii, reaches a maximum at the LSP resonance energy for $a \sim 25$ nm and then begins to diminish. This behavior is well-known and underlies conventional design principles for photothermal systems, which seek to optimize the single-particle heat power.

In the case of periodic lattices, the absorption cross section and heat power inherit the energy-momentum dispersion dictated by the lattice's discrete translation symmetry. In the infinite lattice limit under plane wave illumination, the magnitudes of the induced dipole moments at each site are all equal but may adopt different directions and phase relationships determined by the coupled dipole equations in reciprocal space [28]

$$\mathbf{p}(k_{\|},\omega) = \left[\overleftrightarrow{\alpha}^{-1}(\omega) - \overleftrightarrow{\mathbf{S}}(k_{\|},\omega)\right]^{-1} \cdot \mathbf{E}_0(k_{\|},\omega), \tag{3.3}$$

which are derived from Eq. (3.2) together with the Bloch ansatz $\mathbf{p}_j = \mathbf{p}(k_{\|})e^{ik_{\|}jd}$. Here $k_{\|}$ is the Bloch wave vector contained within the first Brillouin zone and $\overleftrightarrow{\mathbf{S}}(k_{\|},\omega) = (k^2/\varepsilon)\sum_{j\neq 0}\overleftrightarrow{\mathbf{G}}(\mathbf{r}_0,\mathbf{r}_j,\omega)e^{ik_{\|}jd}$ is the field propagator tensor accounting for diffractive coupling between dipoles. Although this formalism is identical to that used in Ref. [134], the field propagator in the present case is a poorly-convergent infinite series and special care is required to ensure convergence [135]. The total field at the position of each dipole is then $\mathbf{E}(k_{\|},\omega) = \overleftrightarrow{\alpha}^{-1}(\omega)\cdot\left[\overleftrightarrow{\alpha}^{-1}(\omega) - \overleftrightarrow{\mathbf{S}}(k_{\|},\omega)\right]^{-1}\cdot\mathbf{E}_0(\omega)$, resulting in the field enhancement

$$\left[\frac{E(k_{\|},\omega)}{E_0}\right]_{\beta} = \frac{1}{1-\alpha_{\beta\beta}(\omega)S_{\beta\beta}(k_{\|},\omega)} \tag{3.4}$$

for an incident field polarized along the $\hat{\boldsymbol{\beta}}$-direction ($\beta = x, y, z$) in a 1D array where the orthogonally-polarized lattice modes decouple. Field enhancement maxima occur for real-valued frequencies nearby the complex poles of Eq. (3.4) dictated by the condition $\alpha_{\beta\beta}^{-1}(\omega) = S_{\beta\beta}(k_{\|},\omega)$ for $\omega \in \mathbb{C}$, which alters the spectral position of the maximum heat power absorbed relative to that of a single sphere. We capture this effect by defining an array-modified per-particle absorption cross section $\bar{\sigma}_{\mathrm{abs}}(k_{\|},\omega) = \sigma_{\mathrm{abs}}(\omega)(|\mathbf{E}(k_{\|},\omega)|^2/|\mathbf{E}_0(k_{\|},\omega)|^2)$ such that the per-particle heat power $\bar{Q}(k_{\|},\omega) = \bar{\sigma}_{\mathrm{abs}}(k_{\|},\omega)(c\sqrt{\varepsilon}/8\pi)|\mathbf{E}_0(k_{\|},\omega)|^2$ in analogy to the single particle heat power $Q(\omega)$.

Figure 3.1c presents $\bar{Q}(k_{\|} = 0,\omega)/Q_{\mathrm{LSP}}$ as a function of a and $\hbar\omega$ for a $d = 415$ nm periodicity 1D Ag NP array excited by a plane wave at normal incidence with polarization perpendicular to the periodicity direction as shown in Figure 3.1a. The longitudinally polarized lattice dispersion (SI) exhibits weaker coupling of the LSPs to the photonic modes since the far-field radiation lobes of each induced dipole are oriented perpendicular to the array axis, inhibiting long-range coupling [7, 28]. The vertical dashed gray line in Figure 3.1c denotes the energy associated with the Rayleigh anomaly hc/d marking the onset of the SLR. Critically, for NP radii well-beyond that which optimize the single-particle absorption in Figure 3.1b, long-range diffractive coupling enabled by strong scattering contributes to enhanced absorption at the SLR mode energy. This behavior contrasts sharply from previous work on photothermal heating in NP arrays [20, 116], which considered smaller radii NPs optimized for single-particle absorption and precluded observation of robust SLR modes. Indeed, strongly-enhanced photothermal conversion based on SLR modes has been recently demonstrated experimentally under normally incident excitation [136]. The dependence of $\bar{Q}(k_{\|},\omega)/Q_{\text{LSP}}$ on the incident Bloch wave vector $k_{\|}$ for a 415 nm periodicity 1D array of 90 nm diameter Ag nanospheres is shown in Figure 3.1d, demonstrating the ability to modulate photothermal heat absorption via the angle of incidence of the excitation field.

Based upon the method of coupled dipoles [28, 123, 137], these calculations incorporate both scattering and absorption processes in the self-consistent determination of the lattice's optical responses. Thus, properties derived from absorption such as the temperature of the lattice can be calculated from knowledge of the heat power dissipated in each nanosphere. For a finite system of point heat sources $Q_i(\omega) = \sigma_{\text{abs}}(\omega)(c\sqrt{\varepsilon}/8\pi)|\mathbf{E}_{\text{tot}}(\mathbf{r}_i,\omega)|^2$, the superposition principle can be invoked to write the total temperature at a given point $\mathbf{r}$ as a sum over discrete sources, each contributing a factor of $\Delta T(\mathbf{r},\omega) = Q_i(\omega)/4\pi\kappa(\mathbf{r}-\mathbf{r}_i)$, where κ is the thermal conductivity of the surrounding medium and $\mathbf{E}_{\text{tot}}(\mathbf{r}_i,\omega)$ is the total field (incident plus induced) at the position of the ith dipole. All thermal calculations in this work employ the incident plane wave intensity $I_0 = 10^8$ W/m^2 and a thermal conductivity $\kappa = 6\times10^{-10}$ W·nm^{-1}·K^{-1} similar to water. For non-vanishing source radii within the uniform temperature approximation [20, 138], the internal temperature increase of nanosphere i due to nanosphere j is found by spatially averaging the thermal field due to the nanosphere at $\mathbf{r}_j$ over the volume of the nanosphere at $\mathbf{r}_i$. The total internal temperature increase of nanosphere i is then

$$\Delta T(\mathbf{r}_i, \omega) = \frac{Q_i(\omega)}{4\pi\kappa a} + \sum_{j\neq i} \frac{Q_j(\omega)}{4\pi\kappa|\mathbf{r}_i - \mathbf{r}_j|}, \tag{3.5}$$

where the first and second terms account for direct optical absorption ΔT_{opt} and thermal coupling ΔT_{th} contributions to the total internal temperature, respectively. Naturally, the ratio of these two terms at a common frequency

$$\xi_i = \frac{\Delta T_{\text{opt}}}{\Delta T_{\text{th}}} = \left(\frac{a}{Q_i}\sum_{j\neq i}\frac{Q_j}{|\mathbf{r}_i - \mathbf{r}_j|}\right)^{-1} \tag{3.6}$$

defines a unitless quantity of interest with $\xi \gg 1$ and $\xi \ll 1$ characterizing qualitatively different temperature profiles [20]. Specifically, the temperature increase is highly-localized in the vicinity of the particles for $\xi \gg 1$, while there is significant ΔT in regions between particles for $\xi \ll 1$. Baffou showed [20] that the value of this ratio of thermal contributions in the central unit cell of a finite array of N monomer unit cells can be analytically approximated as

$$\begin{aligned} \xi_{1\text{D}} &= \left[\frac{2a}{d}\sum_{i=1}^{(N-1)/2}\frac{1}{i}\right]^{-1} \\ &\approx \frac{d}{2a\log N} \end{aligned} \tag{3.7}$$

when $Q_i = Q$ for all $i = 1, \dots, N$ in Eq. (3.6). While this is expected to be a good approximation for systems of small particles with negligible scattering-induced particle-particle coupling, one may anticipate $Q_i \neq Q_j$ for all i, j in finite arrays with strong particle-particle coupling. On the other hand, the Bloch ansatz ensures $Q_i = Q_j = \bar{Q}$ for all i, j in the infinite lattice limit, but this necessitates $N \to \infty$ and causes $\xi_{1\text{D}} \to 0$ in Eq. (3.7), signaling a breakdown of the model arising from the infinite total heat delivered to the unbounded system. Together these observations motivate the examination of ξ_i in realistic finite lattice systems supporting SLRs.

To explore how the ratio of ΔT_{opt} to ΔT_{th} evolves for finite arrays, we consider an 83 μm array composed of 201 unit cells with 90 nm diameter Ag NPs and $d = 415$ nm periodicity. Figure 3.2a shows the ξ_0 evolution as the number of NPs illuminated in the array center at the SLR energy (~ 2.95 eV) is varied at normal incidence. The ratio ξ_0 is calculated

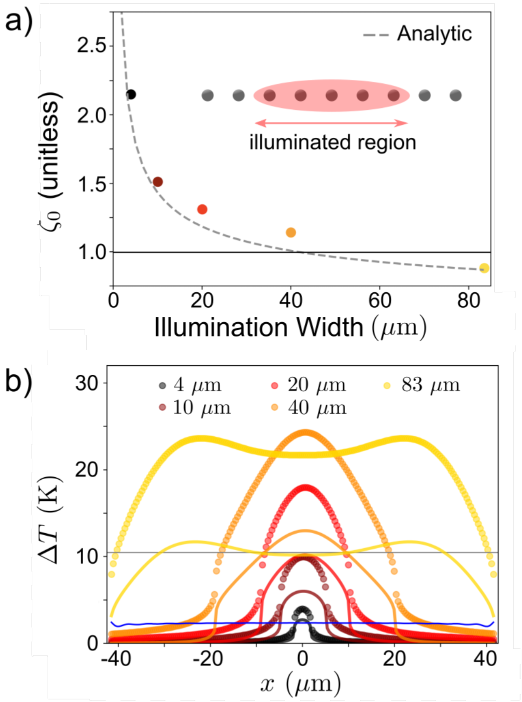

Figure 3.2: Direct optical and thermal coupling contributions to photothermal heating in finite 1D arrays. (a) ξ_0 as the width of the illuminated region at the center of an 83 μm finite array of the type considered in Figure 3.1a is varied. The dashed gray line is the analytic approximation in Eq. (3.7). (b) Total ΔT (bullets) and ΔT_{opt} contribution (lines) for $k_{\parallel} = 0$ excitation at the SLR energy near 2.95 eV as a function of illumination width. The horizontal gray line indicates the value of ΔT_{opt} in the infinite lattice limit, while the blue line shows ΔT for full illumination of the finite array at the single LSP energy near 3.3 eV. The incident laser intensity is $I_0 = 10^8$ W/m^2.

using the site space coupled dipole method (Eq. (3.2)) to evaluate Eq. (3.6) explicitly for $i = 0$ (colored bullets) and compared against the approximate expression Eq. (3.7) (dashed gray) with N determined by the illumination width and the array periodicity d. Figure 3.2a demonstrates that $\xi_0 \sim 1$ for the SLR system considered and that the contribution of $\Delta T_{\rm th}$ to the total ΔT does increase for the particle in the center of a partially-illuminated finite array as the illumination width increases. It is also evident that the approximate expression in Eq. (3.7) accurately predicts ξ_0 for the finite, partially-illuminated system. Nevertheless, Eq. (3.7) is of limited practical utility as it only reports on the temperature increase contributions for the unit cell at the center of the array.

Figure 3.2b presents the total ΔT (bullets) and associated $\Delta T_{\rm opt}$ (lines) contribution at each particle site for $k_{\|} = 0$ excitation at the SLR energy as a function of illumination width (color coded). The trace and bullet colors in panel (b) indicate the illumination width and match the bullet colors used in panel (a). The horizontal dashed gray line marks the value of $\Delta T_{\rm opt}$ in the infinite lattice limit obtained using the reciprocal space coupled dipole equations to evaluate $\bar{Q}(k_{\|} = 0, \omega)$ at the SLR frequency. The nearly-horizontal blue line indicates ΔT at each NP when excited at the single-NP LSP energy. As one might expect, the gray line is $\sim 4\times$ larger than the blue line since $\bar{Q}/Q_{\rm LSP} \sim 4$ in Figure 3.1c,d. Inspection of Figure 3.2b shows that direct optical absorption heating dominates for small illumination regions. When the illumination width reaches 20 μm in this system, $\Delta T_{\rm opt}$ has reached the infinite lattice limit at the central unit cell, but rapidly falls off away from the array center. As the illuminated width continues to increase, $\Delta T_{\rm opt}$ remains approximately equal to the infinite lattice limit at the center of the array, but the number of unit cells away from array center attaining this value also increases. Ultimately, it is this saturation of $\Delta T_{\rm opt}$ along with the increase of the number of heated sites that increases $\Delta T_{\rm th}$ and decreases ξ_0 in Figure 3.2a as the illumination width grows.

3.3.2 Non-Bravais Dimer Arrays

Further control over the photothermal conversion process can be achieved through the introduction of additional degrees of freedom associated with the unit cell design. The non-

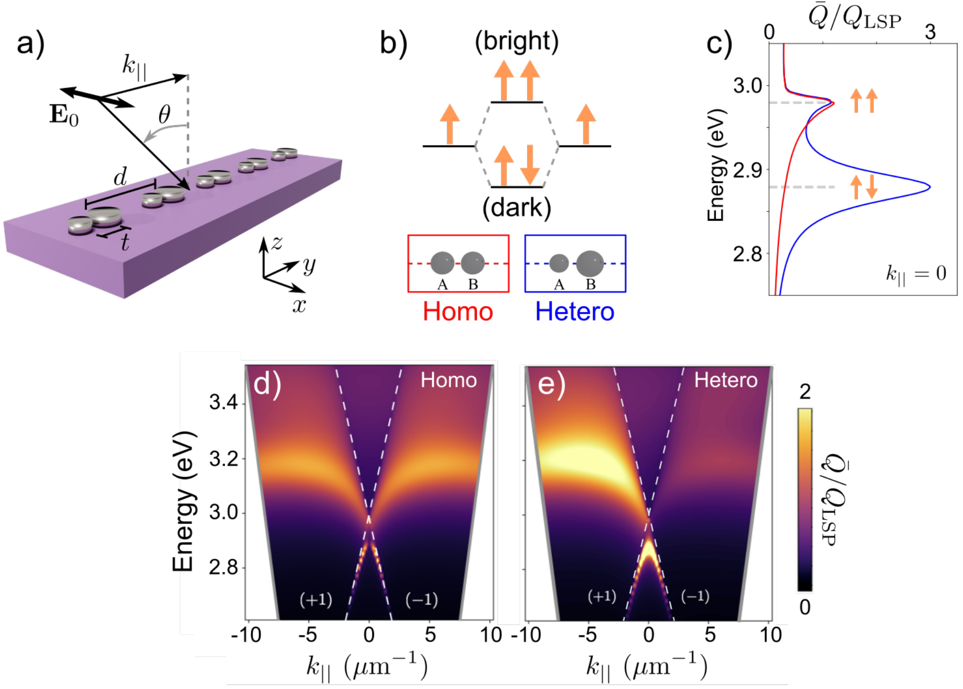

Figure 3.3: Non-Bravais dimer arrays with homo- and heterodimer unit cells. (a) Scheme of 1D dimer array with unit cell and dimer spacings d and t, respectively, excited by a transversely-polarized plane wave. (b) Energy ordering of hybridized transverse dipoles on sites A and B within each unit cell. (c) Normalized per-NP heat power absorption $\bar{Q}/Q_{\rm LSP}$ spectra for the 1D array at the Γ point for homo- (red) and heterodimer (blue) unit cells. (d) and (e) show $\bar{Q}/Q_{\rm LSP}$ as function of $k_{\|}$ for arrays with homo- and heterodimer unit cells, respectively. In panels (c)-(e), $d = 415$ nm and $t = 120$ nm. The particle radii are $a_A = a_B = 45$ nm for the homodimer structure, while $a_A = 40$ nm and $a_B = 50$ nm for the heterodimer structure.

Bravais dimer lattice, for example, involves two sublattices (labeled A and B) with both intra- and inter-sublattice couplings between the plasmonic dipoles on each NP, which are governed by distances t and d, respectively; see Figure 3.3a. In site space, the coupled dipole equations remain of the same form as those presented in Eq. (3.2) except for the case of the heterodimer unit cell where dipoles on each sublattice have different Mie polarizabilities depending upon the radius and dielectric composition of each nanosphere. It is because of their differing polarizabilities that the heterodimer lattice hybridization (Figures 3.3b) produces two optically bright SLRs, while only the in-phase LSP mode forms a bright SLR in the case of the homodimer lattice. This difference is highlighted in Figure 3.3c, which shows $\bar{Q}(k_{\|} = 0, \omega)/Q_{\mathrm{LSP}}$ spectra at the Γ point for the homodimer (red) and heterodimer (blue) lattices of Ag nanospheres with $d = 415$ nm and $t = 120$ nm. The radii of the spherical NPs are $a_A = a_B = 45$ nm for the homodimer, while $a_A = 40$ nm and $a_B = 45$ nm for the heterodimer. Figures 3.3d,e display the band dispersion of the homodimer and heterodimer lattices excited by transversely-polarized plane waves. The asymmetry in incident angle (or equivalently $k_{\|}$) in the dispersion of the heterodimer lattice is again due to the intrinsic asymmetry of the unit cell itself, which will be exploited below to control the temperature profile on the $\lesssim 100$ nm scale.

Based on these SLR absorption spectra, Figure 3.4a shows the computed thermal profiles induced by normal incidence plane wave excitation at varying energies corresponding to spectral features in Figures 3.3d for the homodimer lattice at $k_{\|} = 0$. When excited near the isolated dimer LSP resonance (3.27 eV), sites A and B have the same temperature ($\Delta T_{\mathrm{A}} = \Delta T_{\mathrm{B}}$); however, in moving across the lattice, the temperature profile changes, with dimers in the middle of the array hotter than those at the edges. Alternatively, at the lattice's diffractive Γ point resonances (2.98 eV and 2.88 eV), our calculations indicate significant and controllable temperature differences not only within each unit cell ($\Delta T_{\mathrm{A}} \neq \Delta T_{\mathrm{B}}$), but also across the entire lattice (e.g., there are regions where $\Delta T_{\mathrm{A}} > \Delta T_{\mathrm{B}}$ and others with $\Delta T_{\mathrm{A}} < \Delta T_{\mathrm{B}}$). Similar trends are noted in the heterodimer case (Figure 3.4b), although here we find that the temperature of one particle within the unit cell (either at site A or site B) consistently exceeds the other for nearly all positions across the lattice. Taken together, these results demonstrate the ability to harness dispersive SLR modes to create

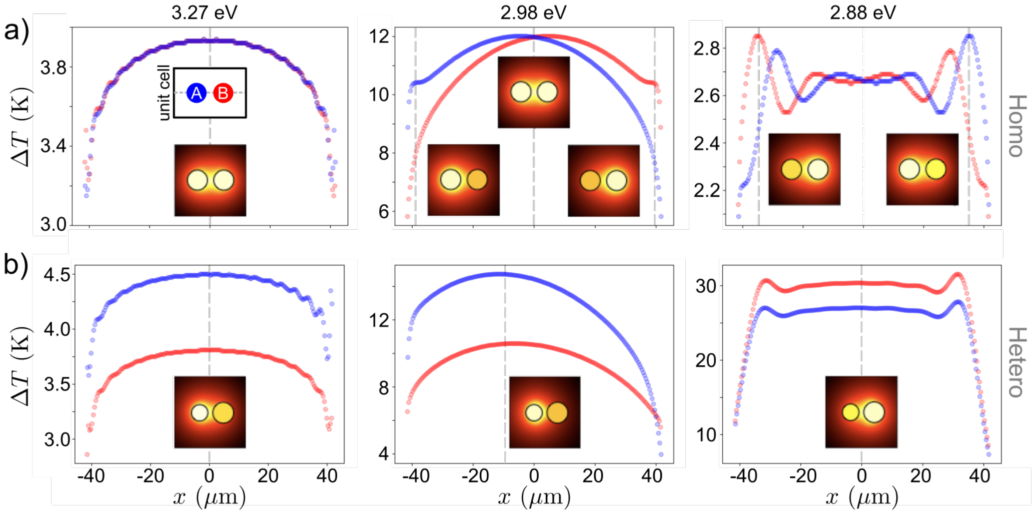

Figure 3.4: Spatial photothermal profiles for 1D non-Bravais dimer arrays. (a) and (b) show ΔT at each lattice site in the finite 83 μm array with homo- and heterodimer unit cells, respectively, of Figures 3.3(c)-(e) illuminated at $k_{\parallel} = 0$. Blue (red) markers indicate the internal temperature increase at the A (B) sites within each unit cell. Examples of the spatial profile of ΔT within specific unit cells at positions marked by vertical dashed gray lines are included. The incident laser intensity is $I_0 = 10^8$ W/m^2.

non-uniform thermal gradients spanning both intra-unit cell ($\lesssim$ 100 nm) and lattice ($\sim$ 100 μm) distances that are actively controllable via changes in the incident angle, energy, and polarization state of light.

3.4 Photothermal Properties of Edge-Localized Modes in 1D and 2D Non-Bravais Homodimer Lattices

Beyond the SLR-enabled thermal profiles demonstrated in the preceding section, here we introduce an entirely new class of edge-localized temperature gradients created by tuning the homodimer lattice towards a topologically non-trivial regime. Considerable research effort has recently been expended to understand the topological properties that can emerge from arrays of plasmonic NPs [130, 139–147] operating in the visible and infrared regions of the electromagnetic spectrum. However, unlike the topological Hermitian model system of Su, Schrieffer, and Heeger (SSH) describing 1D periodic arrays with two sites (A and B) per unit cell and nearest-neighbor coupling [148], Hamiltonians describing plasmonic arrays are fundamentally non-Hermitian due to the radiative and nonradiative damping of each NP [149–151]. Additionally, frequency-dependent NP-NP interactions include vector-valued near, intermediate, and far-field components that go beyond the nearest neighbor scalar coupling assumed in the SSH Hamiltonian [28, 152]. Despite these added complexities, certain plasmonic lattices have been shown to possess topologically-protected edge modes exhibiting a bulk-edge correspondence [139, 151, 153], meaning that properties of the infinite bulk predict the existence (or lack thereof) of edge-localized states in any finite segment of the bulk.

Fundamental to the existence of topologically protected edge states are bulk topological invariants such as the complex-valued Zak phase for one-dimensional systems [154]

$$\gamma_\beta = i\int_{-\pi/d}^{\pi/d} \begin{bmatrix} \hat{\boldsymbol{\beta}}\cdot\mathbf{p}_A^L(k_\parallel) & \hat{\boldsymbol{\beta}}\cdot\mathbf{p}_B^L(k_\parallel) \end{bmatrix}^* \frac{d}{dk_\parallel} \begin{bmatrix} \mathbf{p}_A^R(k_\parallel)\cdot\hat{\boldsymbol{\beta}} \\ \mathbf{p}_B^R(k_\parallel)\cdot\hat{\boldsymbol{\beta}} \end{bmatrix} dk_\parallel, \tag{3.8}$$

here extended to accommodate uncoupled vector modes polarized along $\beta = x, y, z$ and constructed from components of the left $\mathbf{P}^L(k_\parallel, \omega)$ and right $\mathbf{P}^R(k_\parallel, \omega)$ reciprocal space eigenvectors. We consider a non-Bravais homodimer lattice involving two sublattices (A and B) with both intra- and inter-sublattice couplings between the plasmonic dipoles on each NP. Using the Bloch ansatz $\mathbf{p}_j^A = \mathbf{p}_A(k_\parallel)e^{ik_\parallel jd}$ and $\mathbf{p}_j^B = \mathbf{p}_B(k_\parallel)e^{ik_\parallel jd}$, the reciprocal space eigenproblem is

$$\begin{aligned}\overleftrightarrow{\mathcal{A}}(k_\parallel,\omega)\cdot\mathbf{P}(k_\parallel,\omega)=\mathbf{0}&=\begin{bmatrix}\overleftrightarrow{\alpha}^{-1}(\omega)-\overleftrightarrow{\mathbf{S}}(k_\parallel,\omega) & -\overleftrightarrow{\mathbf{T}}_{AB}(k_\parallel,\omega)\\ -\overleftrightarrow{\mathbf{T}}_{BA}(k_\parallel,\omega) & \overleftrightarrow{\alpha}^{-1}(\omega)-\overleftrightarrow{\mathbf{S}}(k_\parallel,\omega)\end{bmatrix}\begin{bmatrix}\mathbf{p}_A(k_\parallel)\\ \mathbf{p}_B(k_\parallel)\end{bmatrix}\\ &=\left(\begin{bmatrix}\overleftrightarrow{\alpha}^{-1}(\omega) & \mathbf{0}\\ \mathbf{0} & \overleftrightarrow{\alpha}^{-1}(\omega)\end{bmatrix}-\overleftrightarrow{\mathcal{G}}(k_\parallel,\omega)\right)\begin{bmatrix}\mathbf{p}_A(k_\parallel)\\ \mathbf{p}_B(k_\parallel)\end{bmatrix},\end{aligned} \tag{3.9}$$

where $\overleftrightarrow{\mathbf{S}}(k_\parallel,\omega)=(k^2/\varepsilon)\sum_{j\neq 0}\overleftrightarrow{\mathbf{G}}(jd,\omega)e^{ik_\parallel jd}$ and $\overleftrightarrow{\mathbf{T}}_{AB/BA}(k_\parallel,\omega)=(k^2/\varepsilon)\sum_j\overleftrightarrow{\mathbf{G}}(jd\pm t,\omega)e^{ik_\parallel jd}$ with $j\in\mathbb{Z}$ indexing the unit cells. Due to the large NP radii and transverse coupling, the $\overleftrightarrow{\alpha}^{-1}(\omega)$, $\overleftrightarrow{\mathbf{S}}(k_\parallel,\omega)$, and $\overleftrightarrow{\mathbf{T}}_{AB/BA}(k_\parallel,\omega)$ matrix elements are nonlinear, transcendental functions of the frequency ω and cannot be accurately linearized by evaluation at the quasistatic LSP resonance frequency ($\omega=\omega_{\mathrm{sp}}$) [155]. Details of how we solve this 6×6 nonlinear eigenproblem to obtain eigenenergies and eigenvectors are discussed in the Methods Section.

Ref. [156] shows that for a non-Hermition SSH model with nearest-neighbor coupling, the complex Zak phase can be expressed in the more compact form $\gamma_\beta=[\phi^\beta_{k_\parallel=\mathrm{X}}-\phi^\beta_{k_\parallel=-\mathrm{X}}]/2$, where $\phi^\beta_{k_\parallel}$ is the relative phase between induced dipole moment components on sublattice sites A and B for the right (or left) reciprocal space eigenvectors at Bloch vector $k_\parallel$. Although this simple method of evaluating γ_β is strictly valid only in the case of nearest-neighbor coupling, it has been used successfully to predict the existence of topologically protected edge-localized modes in longitudinally-coupled 1D plasmonic arrays involving small particles [139]. It must be pointed out, however, that although long-range dipolar coupling does not affect the quantization of the Zak phase, it does break the underlying chiral symmetry possessed by the corresponding nearest-neighbor coupling model, which underlies the existence of the bulk-boundary correspondence [139, 153]. Certain finite plasmonic arrays have been identified, for example, that do not possess gapless, edge-localized eigenvectors despite the corresponding bulk system having a Zak phase of π [153]. Nevertheless, leveraging topologically protected edge states to localize photothermal heating to array edges remains an intriguing prospect.

We now investigate the photothermal properties of a new 1D homodimer lattice with $d=250$ nm, $t=100$ nm, and 90 nm diameter Ag spheres at each site. These parameters are chosen to tune the bulk lattice into a non-trivial topological regime characterized by a complex Zak phase $\gamma_\perp = \pi$ ($\perp = x, z$ since both transverse modes are equivalent by symmetry) as computed using our nonlinear reciprocal space eigensolver. Figure 3.5a displays the normalized per-particle heat power absorbed $\bar{Q}/Q_{\mathrm{LSP}}$ as a function of $k_\parallel$ (underlying color map) of a lattice with 100 unit cells ($N = 200$ particles) having the same periodicity as the bulk under plane wave illumination. The optical polarization is again transverse to the lattice direction, thereby stimulating only the transversely coupled SLR modes associated with strong long-range interactions. The overlaid empty white circles indicate the real parts of the transverse eigenenergies determined using the reciprocal space eigensolver, while the red bullets on the $k_\parallel < 0$ region of Figure 3.5a show the real parts of the transverse eigenenergies calculated from diagonalization of the 10-unit cell finite lattice system, both in the absence of external forcing (Methods). To sort finite lattice eigenenergies in $k_\parallel$ (red bullets), their spatial mode frequencies are examined allowing us to overlay them on top of the $k_\parallel$−resolved absorption spectra (SI). Approximate reciprocal space eigenenergies obtained by linearizing the coupling tensors ($\overleftrightarrow{\mathbf{S}}$ and $\overleftrightarrow{\mathbf{T}}$) at $\omega = \omega_{\mathrm{sp}}$ in Eq. (3.9) are shown as blue bullets on the $k_\parallel > 0$ region of Figure 3.5a for comparison.

Figure 3.5b displays $\bar{Q}/Q_{\mathrm{LSP}}$ spectra for selected points in reciprocal space, where the dip at 2.99 eV (dashed gray line) at the X point denotes the presence of an SLR band gap where an edge-localized mode might be expected [139] in finite segments of the infinite system. However, despite the infinite system having $\gamma_\perp = \pi$, none of the finite system eigenvectors associated with the red bullets in Figure 3.5a are found to be localized to the array edges (SI), indicating this system is in the regime where the bulk-boundary correspondence breaks down [153]. This is, perhaps, not surprising, since strong intra-sublattice (i.e., A-A and B-B) coupling drives the breakdown of the bulk-boundary correspondence [130, 153, 157–161], while SLRs generally involve transverse modes associated with strong intra-sublattice coupling characterized by $\overleftrightarrow{\mathbf{S}}(k_\parallel, \omega)$ [28]. Nevertheless, Figure 3.5c illustrates the existence of edge-localized induced dipole moments in the optically excited system. The induced dipole moments $\mathbf{p}$ are normalized to the induced dipole moment $\mathbf{p}_0$ of a single 90 nm diameter Ag nanosphere excited at the same energy. Recall that since $\mathbf{p}_i = \overleftrightarrow{\alpha}(\omega) \cdot \mathbf{E}_i$ and $\Delta T_{\mathrm{opt}} \propto |\mathbf{E}_i|^2$, the induced dipole moment spatial distribution directly reports on the direct optical heat

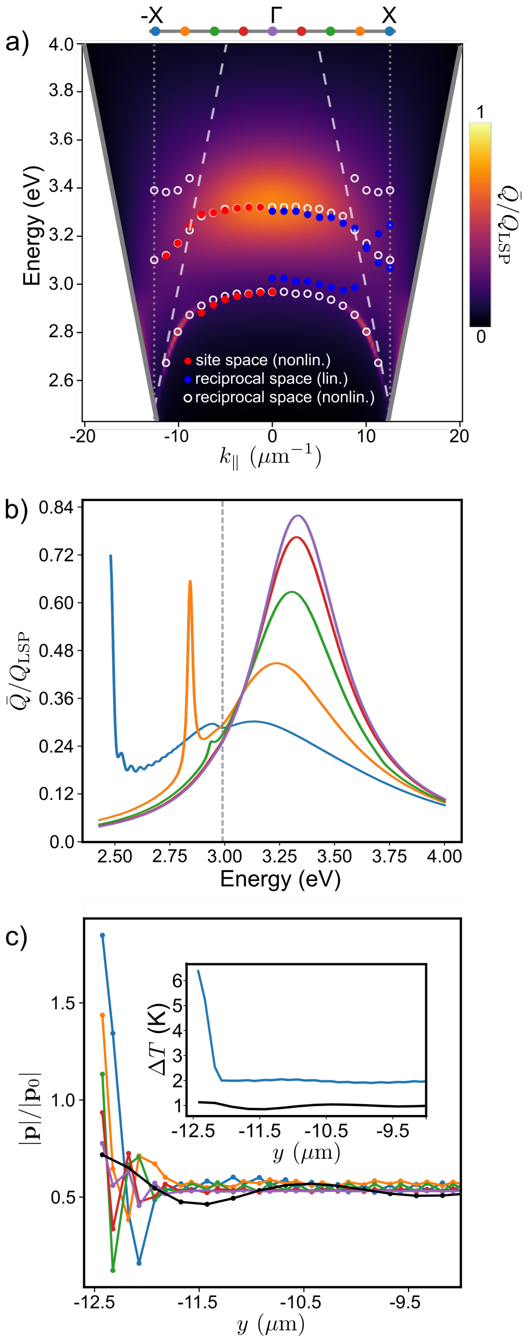

Figure 3.5: 1D homodimer array response. (a) Normalized per-particle heat power absorption $\bar{Q}/Q_{\rm LSP}$ spectra as a function of $k_\parallel$ for a 1D homodimer array composed of 90 nm diameter Ag nanospheres. The sublattice periodicity $d = 250$ nm and the dimer gap $t = 100$ nm. The red bullets represent the eigenenergies in site space, while the white and blue bullets depict the nonlinear and linearized eigenenergies of the infinite lattice, respectively. (b) $\bar{Q}/Q_{\rm LSP}$ spectra for selected points in reciprocal space. (c) Modulus of the induced plasmonic dipole moment on each nanosphere normalized to the induced dipole moment

power delivered to each lattice site. The black line represents the dipolar profile of a 100 unit cell (200 particle) monomer lattice, i.e., a 1D array of nanospheres equally spaced with periodicity $d = t = 250$ nm. We find that while all of the selected points in reciprocal space (colored bullets above Figure 3.3a) exhibit dipole moment distributions with some degree of edge localization, the X point profile (blue) clearly shows the strongest edge-localization. The persistence of edge-localization at other points in reciprocal space and at other energies is likely indicative of the non-Hermitian skin effect [157].

Leveraging such induced dipole moment spatial profiles has the potential to produce edge-localized thermal gradients independent of whether the observed edge-localized induced dipole moments are indicative of strict topologically-protection or not. While previous work has examined radiative heat transfer in plasmonic lattices tuned into the topological regime [162], we are not aware of any studies exploring the possibility of exploiting these systems to realize edge-localized temperature profiles. The inset of Figure 3.5c shows such a thermal profile, obtained by plane-wave excitation of the homodimer lattice at the X point at 2.99 eV (blue) in comparison to the monomer lattice (black) at the same point in the Brillouin zone. The edges of the homodimer lattice have a $3-$fold temperature increase relative to the approximately constant temperature within the lattice interior.

We next investigate the photothermal properties of a finite 2D homodimer lattice assembled by arranging side-by-side copies of the topologically non-trivial 1D homodimer arrays considered in Figure 3.5. Figure 3.6b shows the normalized per-particle heat power absorption $\bar{Q}/Q_{\mathrm{LSP}}$ spectra as a function of k_y for $x-$polarized plane wave illumination. The finite lattice is composed of 20 dimer unit cells oriented along the $y-$direction which are replicated 20 times along the $x-$direction. Thus the $x-$polarized excitation couples to the transversely polarized SLRs with respect to the dimer unit cell axis along $\hat{\mathbf{y}}$ and the edge localization of ΔT intrinsic to each 1D component is inherited by the 2D lattice. Figure 3.6c,d show the 2D polarizations induced at the X point at two different energies, 2.99 eV (red) and 3.13 eV (green). Each point is indicated by a bullet in Figure 3.6b. Panel (c) possesses stronger edge-localization of $|\mathbf{p}|/|\mathbf{p}_0| \propto \Delta T_{\mathrm{opt}}$ in comparison to panel (d). Panels (e) and (f), which include thermal coupling contributions ΔT_{th}, account for conductive heat flow from the surrounding NPs, leading to the largest ΔT_{th} contribution at the array center. Nevertheless

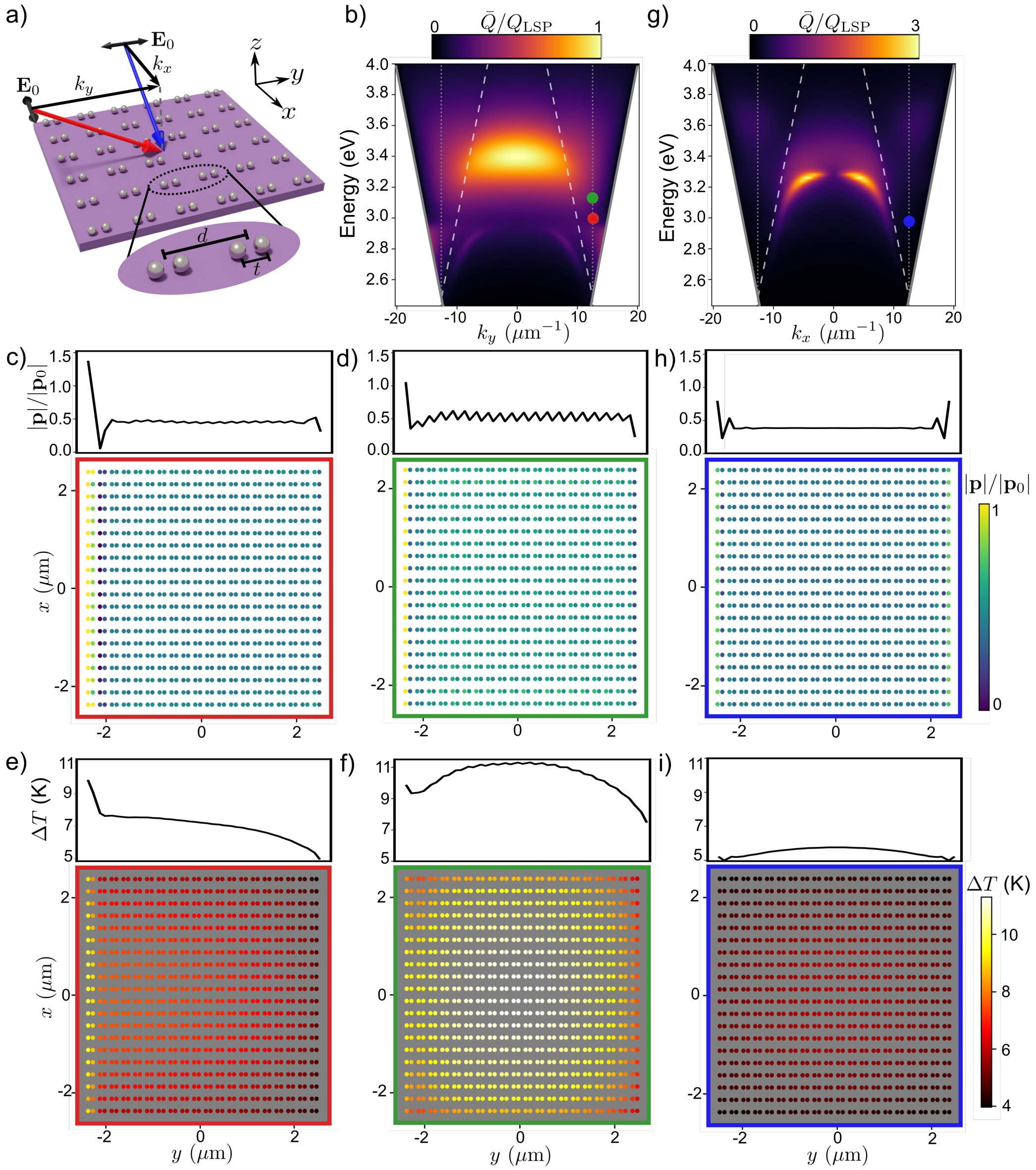

Figure 3.6: 2D homodimer unit cell array response. (a) Array scheme indicating the two excitation geometries considered. The 2D array is composed from replicas of the 1D array from Fig. 3.5 with $d_x = d_y = 250$ nm and $t_y = 100$ nm. (b) Normalized per-particle heat power absorption $\bar{Q}/Q_{\rm LSP}$ spectra as a function of k_y for a finite 20×20 unit cell patch of the 2D array. (c) and (d) show the magnitude of the induced dipole moment on each nanosphere normalized to the induced dipole moment of a single 90 nm Ag nanosphere at the points marked by red and green dots, respectively, in panel (b). (e) and (f) depict the internal temperature increase corresponding to the preceding induced dipole moment plots. (g) $\bar{Q}/Q_{\rm LSP}$ as a function of k_x for the 2D dimer array. (h) Normalized magnitude of the induced dipole moment on each nanosphere at the point marked in blue in panel (g). (i) Spatial map of the thermal profile corresponding to the induced dipole moment distribution

some degree of edge localization on the left lattice edge persists. By rotating the excitation field so that its in-plane wave vector projects entirely along the $x-$direction, Figure 3.6g shows $\bar{Q}/Q_{\mathrm{LSP}}$ as a function of k_x generated under $y-$polarized plane-wave illumination of the same 2D homodimer lattice. Under this excitation geometry, the longitudinally coupled dimer mode is excited within each unit cell, setting up diffractive SLR coupling along the x-direction. By exciting the lattice at the $k_x = \pi/d$ X point at 2.99 eV, Figure 3.6h shows a weakly edge-localized induced polarization, with a modest and spatially delocalized thermal profile (Figure 3.6i). Together, Figures 3.5 and 3.6 highlight the potential of exploiting topologically protected edge modes to spatially localize thermal profiles to finite 1D and 2D array edges, thus establishing a new class of thermal responses that differ significantly from our conventional experiences of heat flow and associated temperature rise.

3.5 Conclusion

Endowed with strong energy-momentum dispersion, broad spatial delocalization, and high quality factors, SLRs offer unexplored potential for transducing optical energy into tailored thermal gradient profiles that are robust in steady state, even in the presence of heat diffusion. Harnessing this potential, we combine analytical theory and numerical calculations to investigate the photothermal properties of SLRs in a variety of diffractively-coupled Bravais and non-Bravais plasmonic NP lattices and demonstrate the ability to exert control over their induced temperature field spanning from nano- to micron-scale dimensions by varying the energy, angle, and polarization of incident radiation. By examining the photonic band structure and associated eigenmodes of an infinite non-Bravais homodimer lattice tuned into its topologically non-trivial regime, we additionally present numerical evidence for the creation of thermal gradient profiles that are localized to the edges of a finite patch of the lattice, thus establishing a new class of thermal responses that differ significantly from our conventional experiences of heat flow and associated temperature rise.

Beyond changing the wavelength of incident light or the lattice periodicity to influence SLR response, other approaches can be implemented to control the thermal spatial distribution within each unit cell as well as across the entire lattice domain. For example, stretching/compressing the array or coupling light to higher-order multipoles in each NP

[163–165] represent two additional strategies of practical utility. Employing more complex non-Bravais unit cells such as plasmon oligomers[7, 166–168] represents another, indicating the high degree of tunability offered by plasmonic lattices for studying photothermal conversion. Leveraging these properties, we anticipate SLR arrays to provide a new platform for studying a variety of photothermal applications in the catalytic, energy, chemical, and biological sciences and engineering.

3.6 Methods

3.6.1 Numerical Solution of the Nonlinear Eigenvalue Problem

In the dipole limit, inspection of the coupled dipole equations shows that the complex-valued eigenfrequencies of the fully-coupled (i.e., each dipole i interacts with every other dipole j) finite 1D homodimer array are dictated by the condition $\det \overleftrightarrow{\mathbf{A}}(\omega_n) = 0$, where the ijth block of the $3N \times 3N$ site-space matrix $\overleftrightarrow{\mathbf{A}}(\omega)$ is given by

$$\overleftrightarrow{\mathbf{A}}_{ij}(\omega) = \alpha^{-1}(\omega)\overleftrightarrow{\mathbb{I}}_{ij} - \overleftrightarrow{\mathbb{G}}_{ij}(\omega) \tag{3.10}$$

for an N dipole system. The diagonal inverse polarizability matrix $\alpha^{-1}(\omega)\overleftrightarrow{\mathbb{I}}$ and purely off-diagonal particle-particle coupling matrix $\overleftrightarrow{\mathbb{G}}(\omega)$ are defined below Eq. (3.2) above. Written in this form, it is clear that the system possesses an eigenvalue $\alpha^{-1}(\omega_r)$ when a complex-valued frequency ω_r can be found such that $\det \overleftrightarrow{\mathbf{A}}(\omega_r) = 0$. In general, this constitutes a generalized nonlinear eigenproblem and it is difficult to locate such eigenfrequencies. Pocock et al. [139] addressed this challenge by employing a linearization approximation that eliminates the frequency dependence of $\overleftrightarrow{\mathbb{G}}(\omega)$ by fixing $\overleftrightarrow{\mathbb{G}}(\omega) = \overleftrightarrow{\mathbb{G}}(\omega_{\rm sp})$, where $\omega_{\rm sp}$ is the quasistatic LSP resonance frequency. This simplification, along with the use of the quasistatic polarizability extended to include the leading order scattering correction to $\alpha(\omega)$, both of which are suitable approximations given the small particle sizes and longitudinal coupling considered in that work, greatly simplifies the identification of eigenfrequencies. However, for the large particle radii and the scattering-mediated diffractive coupling considered in our work, the fully-retarded $\alpha(\omega)$ is determined from the $a_1(\omega)$ Mie scattering coefficient, which does not have a simple ω dependence, and the full frequency dependence of $\overleftrightarrow{\mathbb{G}}(\omega)$ must be retained.

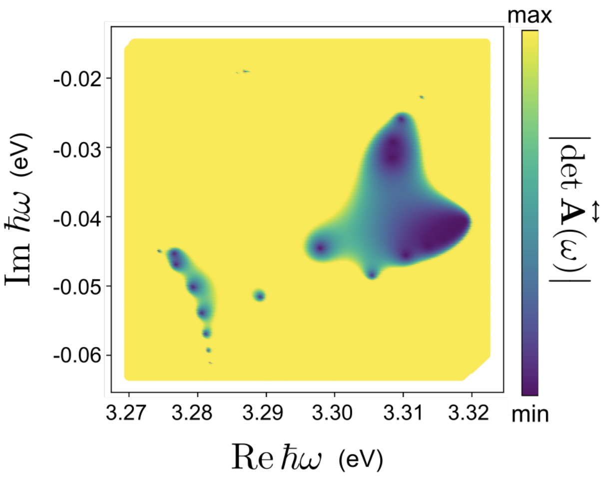

Figure 3.7: Contour plot of $|\det \overleftrightarrow{\mathbf{A}}(\omega)|$, defined in Eq. (3.10), as a function of the complex-valued energy $\hbar\omega$. The darkest points indicate locations of the eigenenergies $\hbar\omega_r$ where $\left|\det \overleftrightarrow{\mathbf{A}}(\omega_r)\right| \approx 0$.

We proceed, therefore, by searching numerically for the complex-valued eigenfrequencies ω_r that satisfy the eigenproblem by being roots of the function $f(\omega) = \left|\det \overleftrightarrow{\mathbf{A}}(\omega)\right|$. This converts the search for complex eigenfrequencies into a search for minima (i.e., roots) on the nonlinear $\left|\det \overleftrightarrow{\mathbf{A}}(\omega)\right|$ surface. Because the nonlinearity of the surface precludes the application of common minimization techniques such as gradient descent algorithms, we perform a grid search over finite domains of real and imaginary frequency space to identify minima of the $\left|\det \overleftrightarrow{\mathbf{A}}(\omega)\right|$ surface and the corresponding eigenfrequencies ω_r. Due to the need to evaluate the sphere polarizability inverse, and therefore the Ag dielectric function $\varepsilon(\omega)$ at complex frequencies, an analytic Drude model is used. Drude model parameters ($\varepsilon_\infty = 5$, $\hbar\gamma = 0.0387$ eV, and $\hbar\omega_p = 8.9$ eV) were taken from Ref. [169]. A representative example of such an eigenfrequency search is shown in Figure 3.7.

Eigenenergies $\hbar\omega_r$ located using this approach for a finite 10 unit cell portion of the $d = 250$ nm, $t = 100$ nm homodimer lattice are shown in Figure 3.5a superimposed over the absorption dispersion diagram. The red and blue bullets in Figure 3.5a are the values

$\mathrm{Re}\,\hbar\omega_r$ determined using $\overleftrightarrow{\mathbb{G}}(\omega_r)$ and $\overleftrightarrow{\mathbb{G}}(\omega_{\mathrm{sp}})$, respectively, during the minimization procedure. To find the eigenvector associated with each ω_r, the $\overleftrightarrow{\mathbb{G}}(\omega_r)$ matrix is constructed and diagonalized numerically, yielding a new set of eigenvalues $\{\lambda_n\}$. We select the eigenvector $\mathbf{P}_r(\omega_r)$ corresponding to the numerically-determined eigenvalue λ_n closest to $\alpha^{-1}(\omega_r)$. This procedure for calculating eigenvectors is appropriate because $[\alpha^{-1}(\omega)\mathbb{I}, \overleftrightarrow{\mathbb{G}}(\omega)] = 0$, which is the case for all monomer and homodimer lattices considered herein.

The same minimization procedure can be applied in reciprocal space to identify a set of eigenfrequencies and associated eigenvectors at each value of $k_\parallel$ for the infinite 1D homodimer array by locating ω_r such that $|\det \overleftrightarrow{\mathcal{A}}(k_\parallel, \omega_r)| = 0$. The reciprocal space coupling matrix in this case is $\overleftrightarrow{\mathcal{A}}(k_\parallel, \omega) = \alpha^{-1}(\omega)\overleftrightarrow{\mathbb{I}} - \overleftrightarrow{\mathcal{G}}(k_\parallel, \omega)$, where

$$\overleftrightarrow{\mathcal{G}}(k_\parallel, \omega) = \begin{bmatrix} \overleftrightarrow{\mathbf{S}}(k_\parallel, \omega) & \overleftrightarrow{\mathbf{T}}_{AB}(k_\parallel, \omega) \\ \overleftrightarrow{\mathbf{T}}_{BA}(k_\parallel, \omega) & \overleftrightarrow{\mathbf{S}}(k_\parallel, \omega) \end{bmatrix}. \tag{3.11}$$

The white open circles in Figure 3.5a show $\mathrm{Re}\,\hbar\omega_r$ versus $k_\parallel$ for the infinite 1D homodimer array calculated using this reciprocal space eigensolver approach and exhibit close agreement with the absorption spectra of the plane wave forced system displayed as the underlying color map. Reciprocal space eigenvectors $\mathbf{P}_r^T(k_\parallel, \omega_r) = \begin{bmatrix}\mathbf{p}_A^T(k_\parallel, \omega_r) & \mathbf{p}_B^T(k_\parallel, \omega_r)\end{bmatrix}$ can then be found using the same procedure used to find eigenvectors for the site space problem.

The reciprocal space eigenvectors are used to evaluate the Zak phase $\gamma_\beta = [\phi^\beta_{k_\parallel = \mathrm{X}} - \phi^\beta_{k_\parallel = -\mathrm{X}}]/2$, where $\phi^\beta_{k_\parallel}$ is the relative phase between the relevant induced dipole moment components on sublattice sites A and B for the right (or left) reciprocal space eigenvectors at Bloch vector $k_\parallel$. For example, γ_x for the transversely-polarized case is evaluated using

$$\phi^x_{k_\parallel} = \mathrm{Arg}\{\mathbf{p}_A(k_\parallel) \cdot \hat{\mathbf{x}}\} - \mathrm{Arg}\{\mathbf{p}_B(k_\parallel) \cdot \hat{\mathbf{x}}\} \tag{3.12}$$

at the ±X points ($k_\parallel = \pm\pi/d$).

3.7 Acknowledgments

This work was supported by the U.S. National Science Foundation under Grant No. NSF CHE-2118333 as well as through the use of advanced computational, storage, and networking infrastructure provided by the Hyak supercomputer system at the University of Washington.

3.8 Supporting Information

Monomer lattice response under longitudinal and transverse incident polarization; Transverse eigenvectors of finite homodimer lattice.

Chapter 4

PROBING THE POLARIZATION OF LOW-ENERGY EXCITATIONS IN 2D MATERIALS FROM ATOMIC CRYSTALS TO NANOPHOTONIC ARRAYS USING MOMENTUM-RESOLVED ELECTRON ENERGY LOSS SPECTROSCOPY

- Rossi, A. W., Bourgeois, M. R., Walton, C., Masiello, D. J. (2024). Probing the polarization of low-energy excitations in 2D materials from atomic crystals to nanophotonic arrays using momentum-resolved electron energy loss spectroscopy. *Nano Letters*, 24 (25), 7748-7756.

4.1 Abstract

Spectroscopies utilizing free electron beams as probes offer detailed information on the reciprocal space excitations of 2D materials such as graphene and transition metal dichalcogenide monolayers. Yet, despite the attention paid to such quantum materials, less consideration has been given to the electron-beam characterization of 2D periodic nanostructures such as photonic crystals, metasurfaces, and plasmon arrays, which can exhibit the same lattice and excitation symmetries as their atomic analogs albeit at drastically different length, momentum, and energy scales. Due to their lack of covalent bonding and influence of retarded electromagnetic interactions, important physical distinctions arise that complicate interpretation of scattering signals. Here we present a fully-retarded theoretical framework for describing the inelastic scattering of widefield electron beams from 2D materials and apply it to investigate the complementarity in sample excitation information gained in the measurement of a honeycomb plasmon array versus angle-resolved optical spectroscopy in comparison to single monolayer graphene.

4.2 Main Text

Historically, techniques employing low energy electrons, such as low energy electron diffraction (LEED), scanning tunneling microscopy (STM), high resolution electron energy-loss spectroscopy (HREELS), and photoemission spectroscopy (PES), have played a critical role in understanding a range of material properties, from local atomic structure [30–32, 170] to dispersion relations of materials hosting collective excitations [41, 171–177]. The isolation of graphene [178] and other 2D atomic crystals [179–181] has furthered the need for state-of-the-art characterization techniques where the excitonic [14–17], phononic [39, 42–44, 182, 183], and plasmonic [21, 34, 40, 47–50, 184, 185] excitations in these materials underlie important applications in optoelectronic devices [15, 21–23] and quantum information technologies [26]. Due to its atom scale spatial resolution and ability to measure broadband spectral responses, electron energy-loss spectroscopy (EELS) performed inside a scanning transmission electron microscope (STEM) has played an important role in characterizing such 2D materials at their native response scales [34–38]. However, the high spatial resolution offered by STEM-EELS relies on momentum space integration, limiting its use as a probe of reciprocal space excitations. By increasing the incident beam width, parallel beam momentum-resolved EELS (q-EELS) in a STEM or widefield q-EELS in a TEM overcome this challenge, offering sufficient momentum resolution to characterize the dispersive responses of graphene [39, 40] and other 2D materials [14, 38, 39]. Similarly, HREELS [41–50] and closely related variants [17, 185, 186] have recently demonstrated the ability to retrieve detailed excitation information of 2D materials.

Like 2D quantum materials, 2D periodic nanophotonic structures, such as photonic crystals, metasurfaces, and plasmon arrays, have been under intense study owing to their facilely tunable optical properties and role in the formation of new hybrid light-matter states via interaction with excitonic media in both weak and strong coupling regimes. Actively tunable array lasers [10–13], bound states in the continuum (BICs) [51–57], and exciton polariton structure, dynamics [58–63], and room temperature condensation [187, 188] represent examples that exploit the energy-momentum dispersion arising from the discrete space translational symmetry of the lattice [28, 127] to create coherent optical states or simulate complex quantum many-body physics. Measurements of these phenomena necessitate the use of characterization tools with simultaneously high energy, momentum, and polarization resolution. While optical-based probes and cathodoluminescence (CL) [189, 190] have been successful in characterizing such materials, the use of q-EELS has been limited to the study of photonic density of states in the vicinity of plasmonic thin film architectures [64] and crystal defects [65], despite its ability to probe sample excitations with high energy and momentum resolution that are inaccessible to light. Like STEM-EELS, a powerful tool for mapping single nanoparticle excitations [66–69], momentum-resolved EEL measurements using widefield electron beams have strong potential in the characterization of periodically structured nanophotonic materials [191], as exemplified by the routine use of q-EELS and HREELS to interrogate 2D atomic crystals.

Here we present a common theoretical framework for the interpretation of widefield q-EELS signals in the measurement of the broadband reciprocal space excitations in 2D periodic materials spanning from atomic to nanoscale and larger dimension. Described within our formalism is the energy-momentum dependence of the probing electron's polarization and relativistic kinematics, additionally illuminating the behavior of reflection scattering processes typical of HREELS across atomic and nanophotonic regimes. While well understood as a probe of 2D materials with Ångstrom-scale bond lengths, the $\gtrsim 100$ nm periodicity scale of 2D nanophotonic materials such as photonic crystals, metasurfaces, and plasmon arrays present a distinctly new physical regime where electromagnetic retardation effects prevail and companion widefield inelastic electron scattering observables must be interpreted accordingly. Through the lens of expanded selection rules appropriate to fully retarded light-matter interactions, we elucidate the conditions under which q-EELS can be adapted for measuring the broadband excitations of nanophotonic 2D materials with emphasis placed upon the evolution of the selection rules for scattering processes both within and beyond the first Brillouin zone (BZ), the excitation of optically dark transitions lying off of the light cone, and role of electron speed and collection geometry. The general complementarity in sample excitation information between widefield electrons and light is also highlighted. Throughout, contrast and comparison between the IR vibrational excitations of graphene and the optical-frequency excitations of a plasmonic honeycomb lattice are made to illustrate the utility of widefield EELS in probing 2D materials excitations spanning broadly across disparate spatial, momentum, and energy scales.

The schemes in Figs. 4.1a,b show a pair of generic widefield inelastic electron scattering events whereby an incoming free electron plane wave with wave vector $\mathbf{k}_i$ (blue) scatters to an outgoing plane wave with wave vector $\mathbf{k}_f$ (red) via interaction with a 2D periodic material sample. The linear momentum $\hbar\mathbf{q} = \hbar(\mathbf{k}_i - \mathbf{k}_f)$ lost by the probing electron is transferred into excited sample states, inducing the transition $|0\rangle \rightarrow |n\rangle$. Experimental conditions, such as detection of transmitted (Fig. 4.1a) versus reflected (Fig. 4.1b) electrons as well as the specific incident and collection angles involved, fix $\mathbf{q}$ (yellow), while the projection $\mathbf{q}_{\|}$ of $\mathbf{q}$ onto the xy sample plane can be manipulated by rotating the sample. Throughout, $\phi = 0°$ such that transverse recoils $\mathbf{q} \cdot \hat{\mathbf{x}}$ in the xz scattering plane are connected with reciprocal space excitations in the 2D-periodic samples with Bloch vectors $(\mathbf{K} \cdot \hat{\mathbf{x}})\hat{\mathbf{x}}$.

As representative 2D-periodic samples that support reciprocal space excitations in the low-loss regime, we consider graphene and a plasmonic honeycomb array (Fig. 4.1c), which support phonons and lattice plasmon polaritons (LPPs), respectively. The 2D atomic (nanoparticle) positions $\mathbf{x}_{\mathbf{n}\kappa} = \mathbf{x}_{\mathbf{n}} + \mathbf{r}_\kappa = n_1\mathbf{a}_1 + n_2\mathbf{a}_2 + \mathbf{r}_\kappa$ in the graphene (plasmonic array) case are situated on a honeycomb lattice, which is a hexagonal Bravais lattice described by primitive lattice vectors $\mathbf{a}_1$ and $\mathbf{a}_2$, with $|\mathbf{a}_1| = |\mathbf{a}_2| = a$ and $s = 2$ sites per unit cell labeled by κ. These sites are colored red and blue in Figs. 1a,b. While both honeycomb arrays share common real space and reciprocal space symmetry, the characteristic length scale is $a = 1.42$ Å for graphene, and $a = 460$ nm for the plasmonic array.

The Hamiltonian involving either class of 2D material can be partitioned as $\hat{H} = \hat{H}_0 + \hat{H}_{\text{int}}$, where $\hat{H}_0 = \hat{H}_s + \hat{H}_{\text{el}}$ is the sum of sample $\hat{H}_s$ and free electron $\hat{H}_{\text{el}}$ components, and $\hat{H}_{\text{int}}$ is the interaction Hamiltonian. Beginning from minimal coupling and working in the generalized Coulomb gauge [192], the interaction Hamiltonian is $\hat{H}_{\text{int}} = (e/2mc)[\hat{\mathbf{A}}\cdot\hat{\mathbf{p}}+\hat{\mathbf{p}}\cdot\hat{\mathbf{A}}]$, where m and $-e$ are the electron mass and charge, and $\hat{\mathbf{A}}$ and $\hat{\mathbf{p}}$ are the quantum mechanical operators associated with the vector potential of the target and the linear momentum of the free electron probe, respectively. The widefield double differential cross section (DDCS)

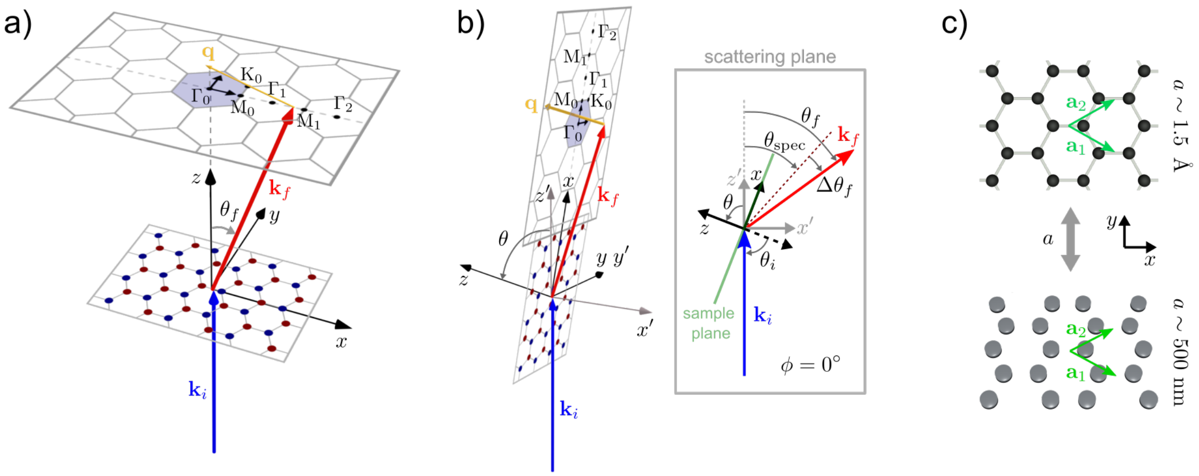

Figure 4.1: Probing reciprocal space excitations in 2D material systems with q-EELS. a) Scheme of q-EELS measurement under forward scattering conditions. Momentum transfers between initial $\mathbf{k}_i$ (blue) and final $\mathbf{k}_f$ (red) free electron states are dictated by the scattering angle θ_f and recoil momentum $\hbar\mathbf{q}$ (yellow) with projection $\mathbf{q}_{\|} = (\mathbf{q}\cdot\hat{\mathbf{x}})\hat{\mathbf{x}}$ oriented along the $\Gamma - \mathrm{M}$ direction of the sample. b) Scheme of q-EELS measurement under reflection scattering conditions, otherwise sharing the same kinematical parameters as in transmission. The inset defines the xz scattering plane relevant to both transmission and reflection geometries. The detection angle is θ_f in transmission and $\Delta\theta_f = \theta_f - \theta_{\mathrm{spec}}$ in reflection, where θ_{spec} is the specular angle. Lab (primed) and sample (unprimed) coordinates are distinguished, and the xz-scattering plane is always perpendicular to the 2D sample xy-plane. Beginning with coincident lab and sample axes as in (a), where only the sample axes are explicitly labeled, and collecting momentum recoils within the $x'z'$-plane, an arbitrary planar scattering configuration can be reached by (i) rotating the sample by angle ϕ about the z'-axis, followed by (ii) rotation by angle θ about the lab y'-axis. c) Graphene (upper) and a plasmonic array (lower) are examples of 2D periodic honeycomb lattices structured on the atomic and photonic length scales, respectively. a is the magnitude of the primitive vectors $\mathbf{a}_1$ and $\mathbf{a}_2$ spanning the real space array. In either case, point M_0 is located at $\mathbf{q}_{\|} = (2\pi/\sqrt{3}a, 0)$.

with fully-retarded probe-sample interactions becomes [79, 80]

$$\frac{\partial^2\sigma}{\partial E_{if}\partial\Omega_f} = \left(\frac{mL^3}{\pi\hbar^2}\right)^2\left(\frac{k_f}{k_i}\right)\int d\omega\, d\mathbf{x}d\mathbf{x}'\,\mathrm{Im}\Big[\mathbf{J}^*_{fi}(\mathbf{x})\cdot\bar{\mathbf{G}}(\mathbf{x},\mathbf{x}',\omega)\cdot\mathbf{J}_{fi}(\mathbf{x}')\Big]\delta(\omega-\varepsilon_{if}), \tag{4.1}$$

where L is the box quantization length, $E_{if} = \hbar\varepsilon_{if} = \hbar\varepsilon_i - \hbar\varepsilon_f$ is the loss energy, and $\hbar\varepsilon_{i/f} = \gamma_{i/f}mc^2$ with initial/final Lorentz contraction factors $\gamma_{i/f} = \big[1-(v_{i/f}/c)^2\big]^{-1/2}$. The transition current density produced as the probing electron transitions between incoming $\psi_i(\mathbf{x}) = L^{-3/2}e^{i\mathbf{k}_i\cdot\mathbf{x}}$ and outgoing $\psi_f(\mathbf{x}) = L^{-3/2}e^{i\mathbf{k}_f\cdot\mathbf{x}}$ plane wave states is $\mathbf{J}_{fi}(\mathbf{x}) = -(e\hbar/2mL^3)(2\mathbf{k}_i-\mathbf{q})e^{i\mathbf{q}\cdot\mathbf{x}}$, while $\bar{\mathbf{G}}(\mathbf{x},\mathbf{x}',\omega)$ is the dyadic Green's tensor characterizing the electromagnetic responses of the sample. Leveraging the plane wave form of $\mathbf{J}_{fi}(\mathbf{x})$, Eq. (4.1) can be recast as

$$\begin{aligned}\frac{\partial^2\sigma}{\partial E_{if}\partial\Omega_f} &= -\frac{1}{\pi}\left(\frac{mv_iL^2}{2\pi\hbar^2}\right)^2\left(\frac{k_f}{k_i}\right)\sum_{\kappa\kappa'}\mathrm{Im}\Big[\mathbf{E}^{0*}_{fi,\mathbf{q}\kappa}(\varepsilon_{if})\cdot\bar{\mathbf{\Pi}}_{\mathbf{q}\kappa\kappa'}(\varepsilon_{if})\cdot\mathbf{E}^{0}_{fi,\mathbf{q}\kappa'}(\varepsilon_{if})\Big]\\ &= -\frac{1}{\pi}\left(\frac{mv_iL^2}{2\pi\hbar^2}\right)^2\left(\frac{k_f}{k_i}\right)\sum_{\kappa}\mathrm{Im}\Big[\mathbf{E}^{0*}_{fi,\mathbf{q}\kappa}(\varepsilon_{if})\cdot\mathbf{p}_{n0,\mathbf{q}\kappa}(\varepsilon_{if})\Big]\end{aligned} \tag{4.2}$$

where

$$\mathbf{E}^0_{fi,\mathbf{q}\kappa} = \frac{2\pi ie\gamma_i}{k_iL^2\omega}\,\frac{(\omega/c)^2\bar{\mathbf{I}}-\mathbf{q}\mathbf{q}}{(\omega/c)^2-q^2}\cdot(2\mathbf{k}_i-\mathbf{q})e^{i\mathbf{q}\cdot\mathbf{r}_\kappa} \tag{4.3}$$

is the Fourier coefficient of the probe's vacuum transition field $\mathbf{E}^0_{fi}(\mathbf{x},\omega) = -4\pi i\omega\int d\mathbf{x}'\,\bar{\mathbf{G}}_0(\mathbf{x},\mathbf{x}',\omega)\cdot(L/v_i)\mathbf{J}_{fi}(\mathbf{x}')$ with free space Green's dyadic $\bar{\mathbf{G}}_0(\mathbf{x},\mathbf{x}',\omega) = (-1/4\pi\omega^2)[(\omega/c)^2\bar{\mathbf{I}}+\nabla\nabla]e^{i(\omega/c)|\mathbf{x}-\mathbf{x}'|}/|\mathbf{x}-\mathbf{x}'|$. The Fourier coefficient is related to the position- and frequency-dependent field, evaluated at $\mathbf{x} = (\mathbf{x}_{\mathbf{n}\kappa}, z=0)$ and $\omega = \varepsilon_{if}$, as $\mathbf{E}^0_{fi}(\mathbf{x}_{\mathbf{n}\kappa},\varepsilon_{if}) \equiv \mathbf{E}^0_{fi,\mathbf{n}\kappa}(\varepsilon_{if}) = \mathbf{E}^0_{fi,\mathbf{q}\kappa}e^{i\mathbf{q}\cdot\mathbf{x}_\mathbf{n}}$. Intrinsic excitations of the sample are encoded within the tensor-valued $\mathbf{q}$-dependent response function $\bar{\mathbf{\Pi}}_{\mathbf{q}\kappa\kappa'}(\varepsilon_{if})$, while the subset that are excited by the electron probe are characterized by the induced moment $\mathbf{p}_{n0,\mathbf{q}\kappa}(\varepsilon_{if}) = \sum_{\kappa'}\bar{\mathbf{\Pi}}_{\mathbf{q}\kappa\kappa'}(\varepsilon_{if})\cdot\mathbf{E}^0_{fi,\mathbf{q}\kappa'}(\varepsilon_{if})$.

The discrete translation symmetry shared by each structure necessitates periodic energy-momentum dispersion of both phonon and LPP quasiparticles excitations. In either class of 2D material, Bloch wave excitations with in-plane momentum $\hbar\mathbf{K}$ can be described by the equations of motion (SI)

$$-\omega^2\mathbf{u}_{\mathbf{K}\kappa} - i\eta\omega\mathbf{u}_{\mathbf{K}\kappa} + \sum_{\kappa'}\bar{\boldsymbol{\mathcal{D}}}_{\kappa\kappa'}(\mathbf{K},\omega)\cdot\mathbf{u}_{\mathbf{K}\kappa'} = Z_\kappa eM_\kappa^{-1}\mathbf{E}^0_{\mathbf{K}\kappa}, \tag{4.4}$$

where the displacement of the coordinate at lattice position $\mathbf{x}_{\mathbf{n}\kappa}$ is $\mathbf{u}_{\mathbf{n}\kappa} = \mathbf{u}_{\mathbf{K}\kappa} e^{i\mathbf{K}\cdot\mathbf{x}_{\mathbf{n}}} e^{-i\omega t}$. Electron beams serve as one example of a probe of reciprocal space lattice excitations where the in-plane recoil momentum $\hbar\mathbf{q}_{\|}$ is the Bloch momentum $\hbar\mathbf{K}$. However, propagating free space light can also drive lattice responses at specific $\mathbf{K}$ points corresponding to the projection $\mathbf{k}_{\|}$ of its wavevector $\mathbf{k}$ onto the sample plane. In either case, the induced moments are $\mathbf{p}_{n0,\mathbf{K}} = [Z_1 e\mathbf{u}_{\mathbf{K}1}, \ldots, Z_s e\mathbf{u}_{\mathbf{K}s}] = [(-\omega^2 - i\eta\omega)\bar{\bar{\mathbf{I}}} + \bar{\bar{\boldsymbol{\mathcal{D}}}}(\mathbf{K},\omega)]^{-1}[(Z_1 e)^2\mathbf{E}^0_{\mathbf{K}1}/M_1, \ldots, (Z_s e)^2\mathbf{E}^0_{\mathbf{K}s}/M_s] = \bar{\bar{\mathbf{\Pi}}}_{\mathbf{K}}(\omega)\mathbf{E}^0_{\mathbf{K}}$, where the $3s \times 1$ vector $\mathbf{E}^0_{\mathbf{K}} = [\mathbf{E}^0_{\mathbf{K}1}, \ldots, \mathbf{E}^0_{\mathbf{K}s}]$ represents the specific probe under consideration evaluated at each of the s sublattice sites. Double bars have been introduced to distinguish $3s \times 3s$ matrices from 3×3 matrices, which have a single bar, e.g., $\left[\bar{\bar{\mathbf{\Pi}}}_{\mathbf{K}}(\omega)\right]_{\kappa\kappa'} = \bar{\mathbf{\Pi}}_{\mathbf{K}\kappa\kappa'}(\omega)$, while the absence of a κ subscript indicates that a vector is $3s \times 1$.

Focusing first on atomic crystal phonons where the resonant IR wavelengths together with subnanometer bond lengths justify neglect of the finite speed of light, the generalized dynamical matrix $\bar{\boldsymbol{\mathcal{D}}}_{\kappa\kappa'}(\mathbf{K},\omega)$ reduces to the conventional dynamical matrix $\bar{\mathbf{D}}_{\kappa\kappa'}(\mathbf{K}) = \bar{\mathbf{F}}_{\kappa\kappa'}(\mathbf{K}) + \bar{\mathbf{C}}_{\kappa\kappa'}(\mathbf{K})$ [81], which accounts for the sum of covalent $\bar{\mathbf{F}}_{\kappa\kappa'}(\mathbf{K})$ and ionic $\bar{\mathbf{C}}_{\kappa\kappa'}(\mathbf{K})$ interactions (SI). We compute all electron-induced graphene excitations within the harmonic crystal approximation [81, 91] based upon Eq. (4.4) using an empirically-parameterized model [87, 88] for $\bar{\mathbf{F}}_{\kappa\kappa'}(\mathbf{q}_{\|})$ and $\mathbf{q}$-dependent effective charges $Z_\kappa(\mathbf{q}_{\|})$ along $\Gamma - \mathrm{M}$ from Ref. [39] (SI). Within the sample and scattering planes lie the longitudinal acoustic (LA) and optical (LO) phonons, while the transverse acoustic (TA) and optical (TO) phonons are polarized within the sample plane but are oriented perpendicular to the scattering plane. Oscillations of the z-directed acoustic (ZA) and optical (ZO) phonons are directed normal to the sample plane. Figs. 4.2a,b display the calculated energy-momentum dispersion $\hbar\omega_\lambda(\mathbf{K}')$ of the phonon eigenmodes (gray traces), where $\lambda = 1-6$ denotes the band indices, as well as the phononic responses induced under widefield (plane wave) electron excitation as encoded in the q-EELS DDCS collected in the transmission (panel a) and reflection (panel b) geometries, where momentum conservation requires $\mathbf{K} = \mathbf{q}_{\|} = (\mathbf{q}\cdot\hat{\mathbf{x}})\hat{\mathbf{x}} = \mathbf{K}' + \mathbf{G}$, with $\mathbf{G}$ a reciprocal lattice vector. At each $\mathbf{q}_{\|}$ point, the spectrum is independently normalized to the maximum DDCS value, as in Ref. [39]. For unnormalized q-EELS DDCS spectra, see Fig. S1. In Fig. 4.2a, the incident plane wave wave vector $\mathbf{k}_i$ of the electron probe is normal to the graphene surface ($\theta_i = 0°$) and its initial speed is $v_i = 0.3c$, which are

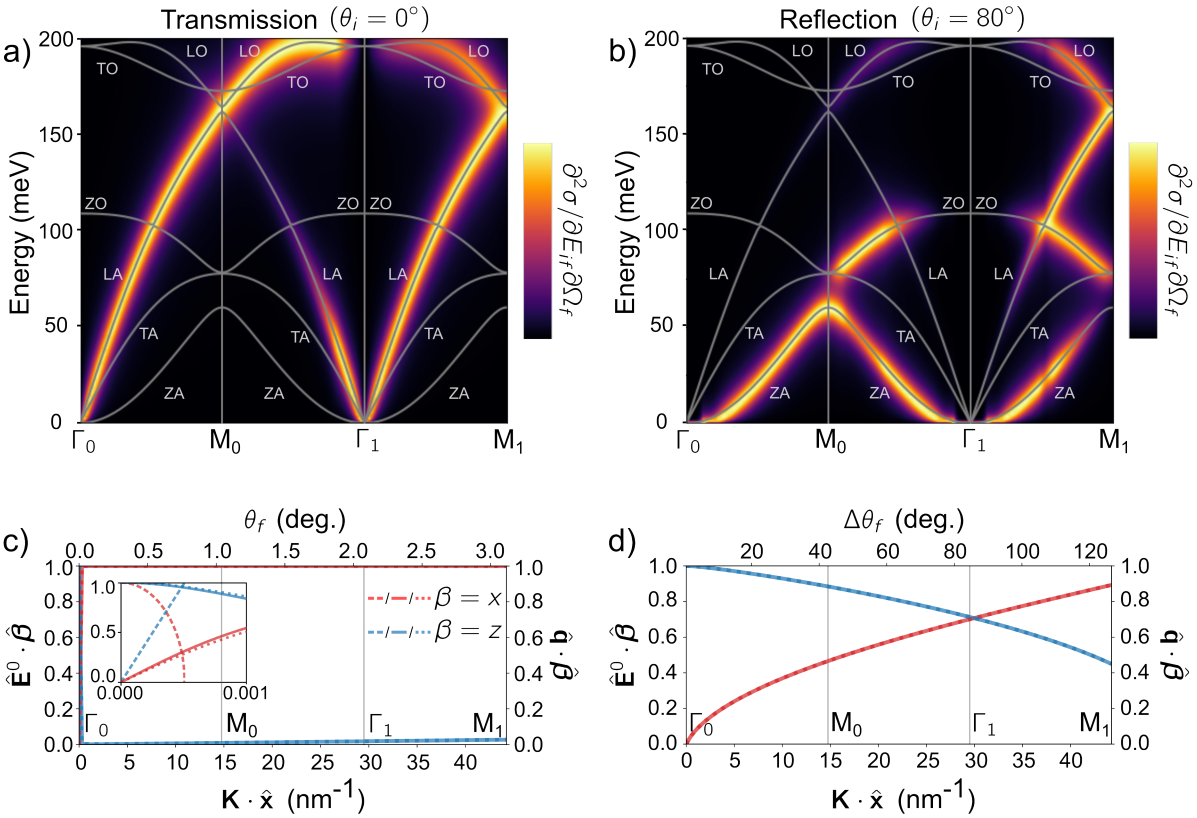

Figure 4.2: Energy-momentum dispersion of graphene phonons probed along the $\Gamma - \mathrm{M}$ direction. a) and b) display the q-EELS DDCS in the transmission and reflection geometries, respectively. Each spectrum at fixed $\mathbf{q}_{||}$ is independently normalized to the maximum DDCS value at that $\mathbf{q}_{||}$ point as in Ref.[39]. Gray traces indicate the dispersion of the graphene phonon eigenenergies. c) and d) show the normalized magnitude of the in-plane $\mathbf{E}^0_{fi} \cdot \hat{\mathbf{x}}$ (red) and out-of-plane $\mathbf{E}^0_{fi} \cdot \hat{\mathbf{z}}$ (blue) components of the electron's vacuum transition field at $E_{if} = 100$ meV versus $\mathbf{q}_{||}$ along $\Gamma_0 - \mathrm{M}_1$, computed in the fully-retarded (solid) and quasistatic (dotted) limits in transmission (c) and reflection (d) geometries. Note the scale difference between θ_f and $\Delta\theta_f$ in (c) and (d). The inset in c) shows the dispersion of $\mathbf{E}^0_{fi}$ as well as that of free space plane wave light $\mathbf{E}^0 = E_0\hat{\boldsymbol{\epsilon}}(\mathbf{k})$ in the immediate vicinity of the Γ_0 point, where the dashed lines represent the in-plane $\mathbf{E}^0 \cdot \hat{\mathbf{x}}$ (red) and out-of-plane $\mathbf{E}^0 \cdot \hat{\mathbf{z}}$ (blue) components of the incident optical field at $\hbar\omega = 100$ meV versus in-plane wave vector $\mathbf{k}_{||} = (\mathbf{k} \cdot \hat{\mathbf{x}})\hat{\mathbf{x}}$. In a) and c), the incident electron wave vector $\mathbf{k}_i$ is oriented normal to the sample plane ($\theta_i = 0°$) with initial velocity $v_i = 0.3c$. In b) and d), $\theta_i = 80°$ with respect to the surface normal in the xz scattering plane and $v_i = 0.01c$. All calculations include an empirical damping rate of $\eta = 20$ meV$/\hbar$ at zero temperature and a vacuum background.

parameters typical of q-EELS experiments performed in the transmission geometry [14, 39]. Reflection measurements, on the other hand, generally involve momentum transfers with a larger out-of-plane component (Figs. 4.1a,b) such that the DDCS is largest for low incident electron kinetic energies and large angles of incidence θ_i [42–44]. Thus, for the reflection calculations in Fig. 4.2b, we choose $\theta_i = 80^\circ$ from the surface normal and $v_i = 0.01c$, typical of HREELS experiments.

It is evident from Eq. (4.2) that the selection rule for electron beam excitation of a specific phonon mode $\boldsymbol{\xi}_\lambda$ at $\mathbf{q}_\|$ of energy $\hbar\varepsilon_{if}$ requires overlap of the electron's vacuum field $\mathbf{E}^{0*}_{fi,\mathbf{q}}$ in Eq. (4.3) with the induced phonon moment $\mathbf{p}_{n0}$ dominated by $\boldsymbol{\xi}_\lambda$ at $\mathbf{q}_\|$ and $\hbar\varepsilon_{if}$. However, in the quasistatic ($c \to \infty$) and dipole ($a \ll 2\pi c/\varepsilon_{if}$) limits relevant to graphene, the electron's transition field $\mathbf{E}^0_{fi,\mathbf{q}}(\mathbf{x}) \propto q^{-2}\mathbf{q}$, and the general induced phonon moments become the induced dipole moments, i.e., $\mathbf{p}_{n0} \to \mathbf{d}_{n0}$, so that the selection rule $\mathbf{E}^{0*}_{fi,\mathbf{q}} \cdot \mathbf{p}_{n0,\mathbf{q}}$ reduces to $\sum_\kappa \mathbf{q} \cdot \mathbf{d}_{n0,\mathbf{q}\kappa} = \sum_\kappa \mathbf{q}_\| \cdot \mathbf{d}^\|_{n0,\mathbf{q}\kappa} + q_z d^z_{n0,\mathbf{q}\kappa}$. Based upon the dipole limit of the scattering form factor of a single Coulombically bound target electron, $\langle n|e^{i\mathbf{q}\cdot\mathbf{x}}|0\rangle \approx \langle n|1 + i\mathbf{q}\cdot\mathbf{x} + \cdots|0\rangle \propto \mathbf{q}\cdot\mathbf{d}_{n0}$ [193], this result is expected as electromagnetic retardation effects are negligible for graphene. The $\sum_\kappa \mathbf{q}\cdot\mathbf{d}_{n0,\mathbf{q}\kappa}$ selection rule is also related to that invoked to rationalize HREELS and q-EELS phonon measurements [39, 194, 195].

While the $\sum_\kappa \mathbf{q}\cdot\mathbf{d}_{n0,\mathbf{q}\kappa}$ selection rule explains the absence of the TO and TA bands in the spectra presented in Fig. 4.2 on grounds of symmetry, the degree to which accessible bands contribute to the DDCS spectra inside (and outside) the first BZ can be more clearly understood by considering the top line of Eq. (4.2). In particular, the DDCS is proportional to $|\mathbf{E}^0_{fi,\mathbf{q}}|^2\,\mathrm{Im}\left[\hat{\mathbf{E}}^{0*}_{fi,\mathbf{q}} \cdot \bar{\bar{\boldsymbol{\Pi}}}_\mathbf{q} \cdot \hat{\mathbf{E}}^0_{fi,\mathbf{q}}\right]$, showing that the characteristics of the transition field largely dictate how strongly each tensor component of $\bar{\bar{\boldsymbol{\Pi}}}_\mathbf{q}$ contributes to the DDCS. Although the eigenmode dispersion is periodic in reciprocal space, the momentum dependence of the effective charge $Z(\mathbf{q})$ causes $\bar{\bar{\boldsymbol{\Pi}}}_{\mathbf{K}'+\mathbf{G}} \neq \bar{\bar{\boldsymbol{\Pi}}}_{\mathbf{K}'}$. The dispersions in $\mathbf{q}_\|$ of the electron's field $\mathbf{E}^0_{fi}$ (solid red/blue traces) as well as that of its limiting quasistatic form $\mathbf{E}^0_{fi} \propto \mathbf{q}$ (dotted red/blue traces) are displayed in Figs. 4.2c,d for both transmission and reflection geometries, clearly showing the reduction of the former to the latter in the quasistatic limit appropriate to graphene. Notably, in transmission, the probe is strongly x-polarized except in the immediate vicinity of Γ_0, explaining the preferential excitation of both LA and LO phonons at both small and large momenta, as recently observed in q-EELS measurements of individual freestanding graphene monolayers [39].

In contrast, the probe's polarization in the reflection geometry (Fig. 4.2d) evolves from predominantly z-polarized in the first BZ to predominantly x-polarized in the second BZ. This crossover in polarization content of the electron's field elucidates the computed DDCS in Fig. 4.2b, where primary excitation of ZA and ZO phonons at low momenta [42, 43] give way to the additional excitation of both LA and LO phonons outside of the first BZ. Taken together, these results contrast the different information contained within q-EELS and HREELS measurements of graphene performed at IR energies in the first two BZs. For comparison, optical excitation via propagating free space light is strongly limited in the IR by the light cone boundary, where $\mathbf{K} = |\mathbf{k}|\hat{\mathbf{x}} \sim 10^{-3}$ nm^{-1} (see dashed red/blue traces in the inset of Fig. 4.2c).

Sharing the same hexagonal lattice structure as graphene but with a lattice constant of $a = 460$ nm, Fig. 4.3 considers a 2D plasmonic honeycomb array composed of 100 nm diameter × 60 nm high silver nanodisks. In contrast to graphene, the large lattice constant and optical excitation frequencies of the array renders the entire BZ accessible to optical excitation [12]. Displayed in Fig. 4.3a is the angle-resolved optical extinction cross section $\sigma_{\text{ext}}(\mathbf{k},\omega) = (4\pi\omega/c)\text{Im}\big[\sum_{\kappa}\mathbf{E}^{0*}_{\mathbf{k}\kappa}\cdot\mathbf{p}_{n0,\mathbf{k}\kappa}/|\mathbf{E}^{0*}_{\mathbf{k}\kappa}|^2\big]$, where $\mathbf{E}^{0}_{\mathbf{k}\kappa} = E_0\hat{\boldsymbol{\epsilon}}(\mathbf{k})e^{i\mathbf{k}\cdot\mathbf{r}_\kappa}$ is the Fourier coefficient of the stimulating optical plane wave field with wave vector $\mathbf{k}$, while the fully retarded q-EELS DDCS (Eq. (4.2)) is shown in Fig. 4.3b, both within the first BZ. The inelastic electron scattering spectra are computed in the forward scattering geometry with $\mathbf{k}_i$ oriented along the z-axis ($\theta_i = 0°$) and $v_i = 0.7c$. Both optical and electron beam LPP spectra are calculated from Eq. (4.4) using the method of coupled dipoles where the multipolar plasmon moments $\mathbf{p}_{n0}$ in each silver nanodisk are approximated by individual point electric dipole moments $\mathbf{d}_{n0}$ [5, 7] with anisotropic polarizability evaluated using tabulated dielectric data for silver [196] (SI). Unlike for graphene, site-to-site coupling in nanoparticle arrays is mediated by long-range, causal interactions between nanophotonic antenna modes localized to each nanoscale scattering element. As a consequence, the generalized dynamical matrix $\bar{\boldsymbol{\mathcal{D}}}_{\kappa\kappa'}(\mathbf{K},\omega)$ for LPPs encodes the individual nanoantenna resonances as well as the retarded dipole-dipole interactions between sites (SI). The white traces in Figs. 4.3a,b

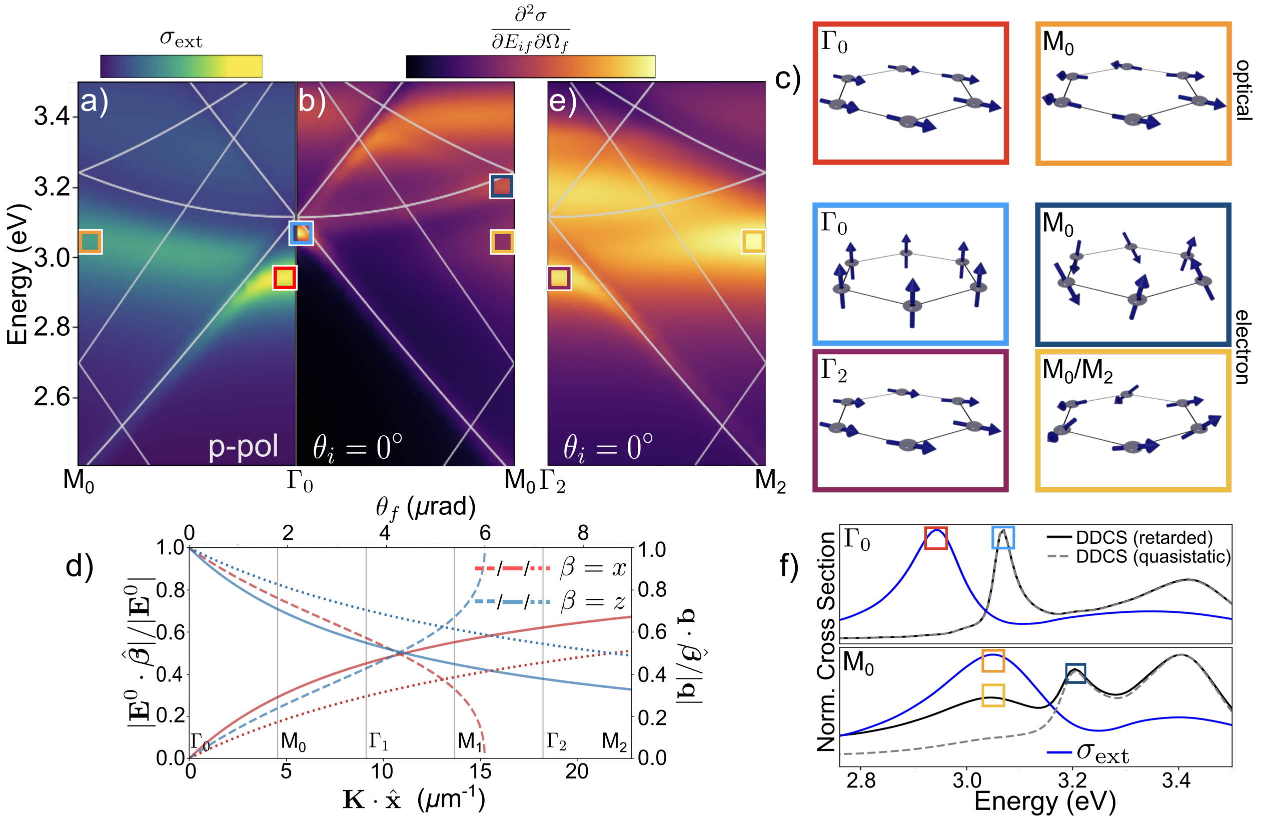

Figure 4.3: Energy-momentum dispersion of LPPs along the $\Gamma - \mathrm{M}$ direction in a honeycomb plasmonic array composed of 100 nm wide × 60 nm high silver nanodisks separated by 460 nm. The localized surface plasmon energies of each isolated nanodisk are 3.13 eV and 3.36 eV in the x and z directions, respectively. a) Normalized optical extinction cross section under p-polarized excitation as a function of incident wave vector $\mathbf{k}_{\|}$ in the first BZ. b) Normalized q-EELS DDCS calculated in the transmission geometry versus recoil wave vector $\mathbf{q}_{\|}$ in the first BZ. The electron's incident wave vector $\mathbf{k}_i$ is oriented normal to the sample surface with an initial velocity of $v_i = 0.7c$. c) Induced LPP polarizations extracted at the boxed points in the optical extinction and q-EELS DDCS spectra. d) Polarization dispersion of the electron's vacuum transition field $\mathbf{E}^0_{fi}$ (solid red/blue) and of the free space plane wave optical field $\mathbf{E}^0$ (dashed red/blue) contrasted against that of the electron's vacuum field $\mathbf{E}^0_{fi} \propto \mathbf{q}$ in the quasistatic limit (dotted red/blue) along the $\Gamma_0 - \mathrm{M}_2$ direction, all computed at 3 eV. e) q-EELS DDCS under same conditions as b) along $\Gamma_2 - \mathrm{M}_2$. The white traces in (a), (b), and (e) are the photonic dispersion of the empty honeycomb lattice. f) Normalized momentum-resolved extinction (blue traces) and retarded/quasistatic DDCS spectra (black/gray-dashed traces) at Γ_0 and M_0 points from (a) and (b). All calculations use a vacuum background.

denote the empty lattice photon dispersion in the reduced zone scheme [122].

The honeycomb lattice LPPs are photonic analogs of the acoustic (in-phase) and optical (out-of-phase) transverse (TA, TO), longitudinal (LA, LO), and z-directed (ZA, ZO) phonon modes of graphene. Under p-polarization, optical extinction (Fig. 4.3a) reveals the in-plane (x-polarized) in-phase LPP at Γ_0, while the electron DDCS (Fig. 4.3b) probes the complementary out-of-plane (z-polarized) in-phase LPP at the same reciprocal space point, as seen by the color-coded induced moment plots in Fig. 4.3c. The induced dipoles exhibit the expected in-phase and out-of-phase polarizations between sites within the unit cell at the high-symmetry points shown in Figs. 4.3a,b. The complementary behavior exhibited by photon and electron probes in Figs. 4.3a,b is generic and can again be understood by examining the general dispersion of the electron's vacuum transition field $\mathbf{E}_{fi}^{0}$ (solid blue/red traces) versus that of plane wave light $\mathbf{E}^{0}$ (solid black/gray traces) shown in Fig. 4.3d. In moving from the first to second BZ, the p-polarized optical field $\mathbf{E}^{0}$ switches from dominantly x-polarized to dominantly z-polarized at the light cone edge near M_1, while $\mathbf{E}_{fi}^{0}$ from Eq. (4.3) is predominantly polarized in the z direction in the first BZ, but evolves to be largely x-polarized at larger $\mathbf{K} = \mathbf{q}_{\|}$. Indeed the computed optical extinction spectrum in Fig. 4.3a shows clear signatures of the x-polarized in-phase and out-of-phase LPPs with increasing $\mathbf{k}_{\|}$ in the first BZ. Near the light cone edge, the z-polarized in-phase LPP becomes evident in $\sigma_{\mathrm{ext}}(\mathbf{k}, \omega)$, however, the z-polarized out-of-phase LPP is not apparent (Fig. S2a). The evolution of $\sigma_{\mathrm{ext}}(\mathbf{k}, \omega)$ under s- and p-polarized excitation as $\mathbf{k}_{\|}$ traverses the full boundary of the irreducible BZ is shown in Fig. S3a,b. Oppositely, but reflecting the crossover behavior in $\mathbf{E}_{fi}^{0}$ polarization at larger $\mathbf{q}_{\|}$ values in Fig. 4.3d, the electron probe excites primarily the z-polarized out-of-phase LPP at M_0 as well as both x-polarized out-of-phase and in-phase LPPs at $\mathrm{M}_0/\mathrm{M}_2$ and Γ_2, respectively, in the third BZ (Fig. 4.3e), a region inaccessible to free space optical excitation. The $\mathbf{q}_{\|}$ value where x- and z-polarized $\mathbf{E}_{fi}^{0}$ cross over can be tuned across multiple BZs in the transmission geometry by varying the primary kinetic energy of the probing electron (Fig. S4). In the reflection geometry typical of HREELS, and as opposed to optical excitation, the electron's transition field is strongly z-polarized across many BZs (Fig. S5).

In contrast to the near indistinguishability of quasistatic and fully-retarded transition fields under the conditions presented in Figs. 4.2c,d for graphene, Fig. 4.3d displays noticeable differences in $\mathbf{E}^0_{fi}$ arising from the finite speed of light. The consequences of these differences are evident in Fig. 4.3f, which displays normalized momentum-resolved optical (blue traces) and electron beam spectra at Γ_0 and M_0, where both fully retarded (black traces) and quasistatic (dashed gray traces) descriptions of the electron's vacuum transition field are adopted. While the normalized DDCS spectra are indistinguishable at the Γ_0 point, where the quasistatic and fully-retarded fields in Fig. 4.3d coincide, it is evident from the M_0 point spectra that a quasistatic description of the electron's field fails to fully capture the electron's ability to excite the x-polarized out-of-phase LPP in the first BZ at ~ 3.05 eV. As compared to the quasistatic case, a fully retarded description of the electron's field involves a larger ratio of x- to z-polarized $\mathbf{E}^0_{fi}$ components, leading to stronger excitation of the x-polarized out-of-phase LPP. This differing evolution of the probe polarization with increasing $\mathbf{q}_{||}$ and resulting complementarity in selection rules in comparison to optical excitation is generic to widefield inelastic electron scattering processes involving any nanophotonic 2D periodic material.

While of considerable utility in the investigation of 2D atomic materials, spectroscopies derived from the inelastic scattering of widefield free electron beams have found less consideration as probes of 2D periodic nanostructures. Here, we have presented a fully-retarded theoretical approach to describe the low energy inelastic scattering of widefield electron beams from 2D periodic materials spanning from atomic-scale quantum materials to nanophotonic array structures beyond the non-recoil approximation. Through inclusion of the relativistic kinematics appropriate to the forward and reflection geometries typical of q-EELS and HREELS measurements, we have investigated the reciprocal space excitations native to a plasmonic honeycomb lattice under both inelastic electron scattering and angle-resolved optical extinction spectroscopies, and compared these observables to the momentum-resolved phonon excitation spectrum of monolayer graphene. Generically, we find important differences arise in the selection rules between 2D atomic and nanophotonic materials under optical- and electron-based probes, leading to complementary behavior in their polarization-dependent responses both inside and outside of the BZ. These differences, together with a breakdown of the quasistatic approximation, thus require consideration of fully retarded light-matter interactions and expanded selection rules to properly interpret inelastic electron scattering signals from 2D periodic materials. Beyond the examples highlighted, the presented theory might be utilized to investigate other material excitations [9, 185, 197–199] with symmetry selection based on free electron wavefront shaping [77, 79, 80].

4.3 Acknowledgments

All work was supported by the U.S. Department of Energy (DOE), Office of Science, Office of Basic Energy Sciences (BES), Materials Sciences and Engineering Division under Award No. DOE BES DE-SC0022921.

4.4 Supporting Information

Additional details related to the employed graphene phonon model, two-dimensional lattice plasmon polariton response matrix, additional graphene and lattice plasmon dispersion diagrams, and the incident electron speed dependence of the transition field.

Chapter 5

STRATEGY FOR DIRECT DETECTION OF CHIRAL PHONONS WITH PHASE-STRUCTURED FREE ELECTRONS.

- Bourgeois, M. R., Rossi, A. W., Masiello, D. J. (2025). Strategy for direct detection of chiral phonons with phase-structured free electrons. *Physical Review Letters*, 134, 026902.

5.1 Abstract

Chiral phonons possessing valley pseudo angular momentum (PAM) underlie a diversity of quantum phenomena of fundamental and applied importance, but are challenging to probe directly. We show that deficiencies of typical momentum-resolved electron energy loss measurements that make it impossible to distinguish the PAM of chiral phonons can be overcome by introducing pinwheel free electron states with well-defined PAM. Transitions between such states generate 2D periodic arrays of in-plane field vortices with polarization textures tailored to selectively couple to desired chiral mode symmetries.

5.2 Main Text

Chirality plays a central role in nearly all aspects of physics, chemistry, and biology. At large length scales, chiral gravitational waves have been considered as sources of circularly polarized contributions to the cosmic microwave background [200], while at short length scales chirality dictates molecular interactions and organizations underpinning biological processes. In condensed matter physics, chirality and spin-momentum locking are at the heart of the menagerie of identified Hall effects, as well as stable [201, 202] and transient free space [203, 204] and evanescent [197, 198, 205–207] topological electromagnetic field textures. Following the report [208] of helicity-resolved Raman scattering experiments from transition-metal dichalcogenide (TMD) atomic layers, it was predicted [9] that two-dimensional (2D) atomic crystals with hexagonal symmetry can host chiral phonons with well-defined pseudo angular momentum (PAM) arising from discrete rotational crystal symmetry. Direct experimental evidence of chiral phonons was subsequently reported based on transient infrared circular dichroism measurements of a monolayer TMD [199], generating significant interest in the potential for leveraging chiral phonons to achieve novel material properties that are sensitive to low-energy spin-selective excitations. Beyond 2D hexagonal lattices, chiral phonons have been identified in other 2D [209–214] and 3D [215, 216] crystalline systems, as well as in bio-organic molecules [217]. Chiral phonons have also been recently identified as participants in various exotic condensed matter processes including anomalous thermal Hall conductivity [218] and the chiral-phonon-activated spin Seebeck effect [219], among others [220, 221]. Despite the high-level of current interest in chiral phonons, their experimental detection has been largely limited to optical Raman scattering measurements, with spatial resolution and linear momentum limited by the photon wavelength, and direct detection remains an outstanding challenge impeding further progress [222].

Meanwhile, instrumental advances during the past decade in aberration correction, monochromation, and detector technologies have made it possible to perform vibrational spectroscopy inside a scanning transmission electron microscope (STEM) [35–38, 223]. In particular, momentum-resolved electron energy loss (q-EEL) spectroscopy [14, 36, 39, 224], and the related high-resolution EEL spectroscopy (HREELS) technique [44, 225], have been used to measure the energy-momentum dispersion of phonons in mono- and few-layer 2D atomic crystals. While these measurements have demonstrated the ability of inelastic free electron scattering to complement other phonon measurement techniques, such as inelastic neutron and x-ray scattering, the absence of an obvious electron polarization degree of freedom has hindered the spin-selective detection of chiral phonons using free electrons. However, the transverse phase shaping and coherent detection schemes that were originally developed for core-loss EEL spectroscopy and that enabled magnetic circular dichroism measurements in the TEM [226–228] have been recently adapted to the low loss regime. By selectively monitoring inelastic scattering of free electrons between states with tailored transverse phase profiles, energy loss processes involving desired target mode symmetries [75] and OAM states [74, 76] have been demonstrated, and optical polarization analogs in free electron scattering have been identified [77, 96]. The full potential of these measurement schemes is currently being explored, while the transverse phase shaping and selection technologies underlying them are actively under development [229][230–234].

In this Letter we provide a strategy for leveraging inelastic scattering of transversely phase shaped free electrons to achieve direct detection of chiral phonons within a STEM. We introduce pinwheel free electron states composed of a small number of phased plane wave components that share the same reciprocal space three-fold discrete rotational symmetry as chiral phonons in hexagonal monolayer 2D atomic crystals at the K and K$'$ points, which introduces a new PAM degree of freedom to the probing electrons. In analogy to previous work on OAM-resolved EEL spectroscopy [74, 76–78, 96, 235, 236], pre- and post-selection of the transverse free electron states enables tracking of PAM exchange between pinwheel free electrons and the sample. We trace the utility of the identified phase-shaped free electron transitions to the topological spin textures of their associated transition electric fields, which can be tailored to selectively couple to chiral phonons of the same symmetry and PAM. Compared to light-based probes, inelastic electron scattering offers the potential for superior spatial resolution, in addition to an often simpler interpretation since the Brillouin zone (BZ) edges can be accessed directly. This work informs current and future efforts to detect and characterize chiral phonons using inelastic free electron scattering, and identifies specific experimental geometries and parameters to achieve detection.

As a model 2D atomic crystal with hexagonal symmetry that lacks inversion symmetry, we consider chiral phonons in monolayer hexagonal boron nitride (hBN) situated in the xy plane as depicted in Fig. 5.1a. Eigenenergies $\hbar\omega_\lambda(\mathbf{k}_\|)$ and eigenvectors $\boldsymbol{\xi}_\lambda(\mathbf{k}_\|)$ of the six hBN phonon bands, indexed by λ, are computed within the harmonic crystal approximation [81] with force constants taken from the literature [87, 88, 237]. The gray lines in Fig. 5.1b show the eigenenergies as a function of $\mathbf{k}_\|$ within the first BZ along $\mathrm{K}' - \Gamma - \mathrm{K}$. In contrast to graphene, the lack of inversion symmetry within the 2D plane and the fact that time reversal symmetry is broken at the K and K$'$ points leads to non-degenerate in-plane valley phonon modes at the K and K$'$ reciprocal space points with well-defined PAM [9]. Real-

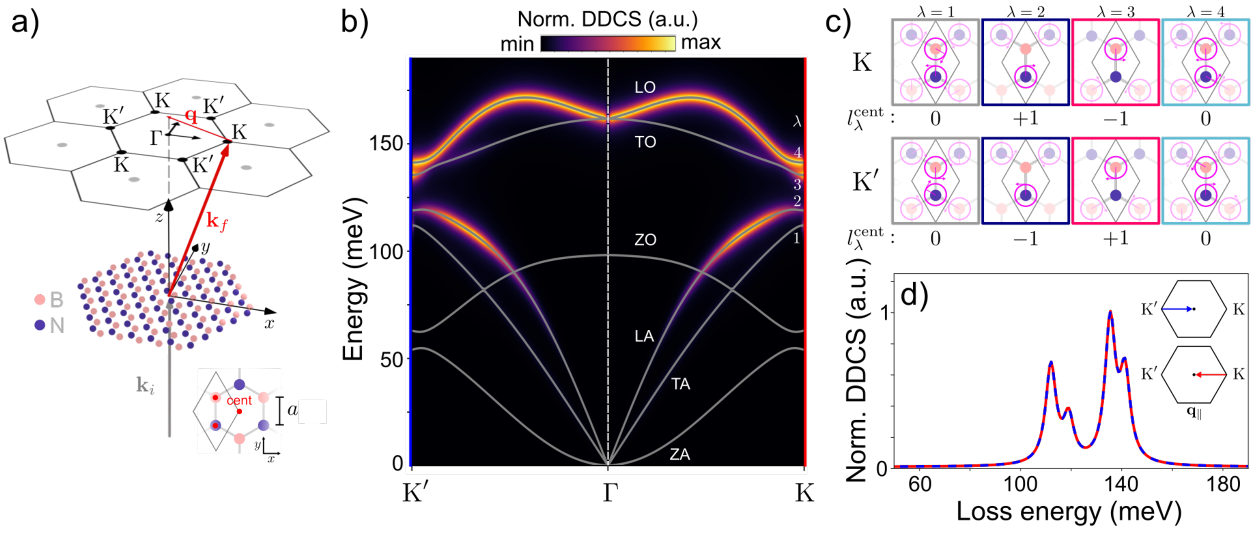

Figure 5.1: hBN phonons and q-EEL spectroscopy. a) Scheme of q-EEL process involving momentum transfer between initial $\mathbf{k}_i$ (gray) and final $\mathbf{k}_f$ (red) free electron states. The recoil momentum $\hbar\mathbf{q}$ has projection $\mathbf{q}_\parallel = (\mathbf{q}\cdot\hat{\mathbf{x}})\hat{\mathbf{x}}$ onto the 2D sample situated in the xy plane. The three C_3 axes (C_3^{B}, C_3^{N}, and C_3^{cent}) associated with hBN are indicated by red markers in the lower inset.

b) Calculated hBN phonon eigenmode dispersion (gray) along $\mathrm{K}'-\Gamma-\mathrm{K}$ and normalized DDCS (color map). c) Real-space in-plane phonon eigenmodes at K and K′. Pink circles indicate circular motion of sublattices, while arrows show the direction of rotation. The PAM $l_\lambda^{\mathrm{cent}}$ is noted below each panel with respect to C_3^{cent}. d) Lineouts of the DDCS spectra at K and K′ from panel (b). All calculations include an empirical damping rate of $\eta = 5$ meV$/\hbar$ at zero temperature and a vacuum background.

space motion of the four in-plane phonon eigenmodes ($\lambda = 1 - 4$), at the K and K$'$ points are shown in Fig. 5.1c. Below each image is listed the total PAM l_λ^{cent} with respect to the C_3^{cent} rotation axis marked in red at the center of the hexagon shown in the panel (a) inset. Additional details regarding the PAM of in-plane phonons, including definition of PAM relative to other C_3 axes, is detailed in [238]. The lowest ($\lambda = 1$) and highest ($\lambda = 4$) energy in-plane modes involve opposing circular motion on both sublattices, with total PAM $l_\lambda^{\text{cent}} = 0$. For the other two in-plane modes ($\lambda = 2, 3$), while one sublattice remains motionless, the other executes circular motion, the handedness of which ultimately determines whether the PAM $l_\lambda^{\text{cent}} = \pm 1$. The depicted phonons exhibit spin-momentum locking in that the z-oriented spin associated with each sublattice (equivalent to handedness of circular motion) changes sign under linear momentum reversal, i.e., K $\leftrightarrow$ K$'$.

For an incoming probing electron with speed v_i, the state-resolved loss rate describing inelastic scattering at first order from the 2D atomic crystal at loss energy $\hbar\omega_{if}$ is [91]

$$w_{fi}^{\text{loss}} = \frac{2}{\hbar}\Big(\frac{v_i}{L}\Big)^2 \frac{L^3}{\Omega_0}\,\text{Im}\sum_\lambda \sum_{\mathbf{k}}^{\text{BZ}} \frac{|\tilde{\mathcal{F}}_\lambda(\mathbf{k})|^2}{\omega_\lambda^2 - \omega_{if}(\omega_{if} + i\eta)}, \tag{5.1}$$

where L^3 defines the probing electron's quantization volume, Ω_0 is the unit cell volume, and $\mathbf{k}$ is within the first BZ. The quantity $\tilde{\mathcal{F}}_\lambda(\mathbf{k}) = \sum_{\mathbf{G}} \sum_\kappa \boldsymbol{\xi}_{\lambda\kappa}^* \cdot M_\kappa^{-1/2} \cdot e\bar{\mathbf{Z}}_\kappa(\mathbf{k}+\mathbf{G}) \cdot \mathbf{E}_{fi,\mathbf{k}+\mathbf{G}\kappa}^0$ involves the atomic masses M_κ and effective charges eZ_κ of each sublattice, indexed by κ, and $\mathbf{G}$ denotes a reciprocal lattice vector. $\mathbf{E}_{fi,\mathbf{k}+\mathbf{G}\kappa}^0$ is the Fourier coefficient of the quasistatic transition electric field $\mathbf{E}_{fi}^0(\mathbf{k}) = -i\mathbf{k}(4\pi/k^2)\,\rho_{fi}(\mathbf{k})$, where $\rho_{fi}(\mathbf{k})$ is the Fourier transform of the charge density $\rho_{fi}(\mathbf{x}) = -e\psi_f^*(\mathbf{x})\psi_i(\mathbf{x})$ associated with the free electron transition from initial state $\psi_i(\mathbf{x})$ to final state $\psi_f(\mathbf{x})$. A phenomenological damping parameter η is introduced to give spectral features finite width.

Fig. 5.1a shows a generic wide field inelastic electron scattering event as typically measured by q-EELS whereby an incoming free electron plane wave with wave vector $\mathbf{k}_i$ (gray) scatters to an outgoing plane wave with wave vector $\mathbf{k}_f$ (red) via interaction with the atomic crystal. In the low loss energy range considered, the linear momentum $\hbar\mathbf{q} = \hbar(\mathbf{k}_i - \mathbf{k}_f)$ lost by the probing electron is transferred into excited phonons with Bloch vector $\mathbf{k}_\parallel$. The

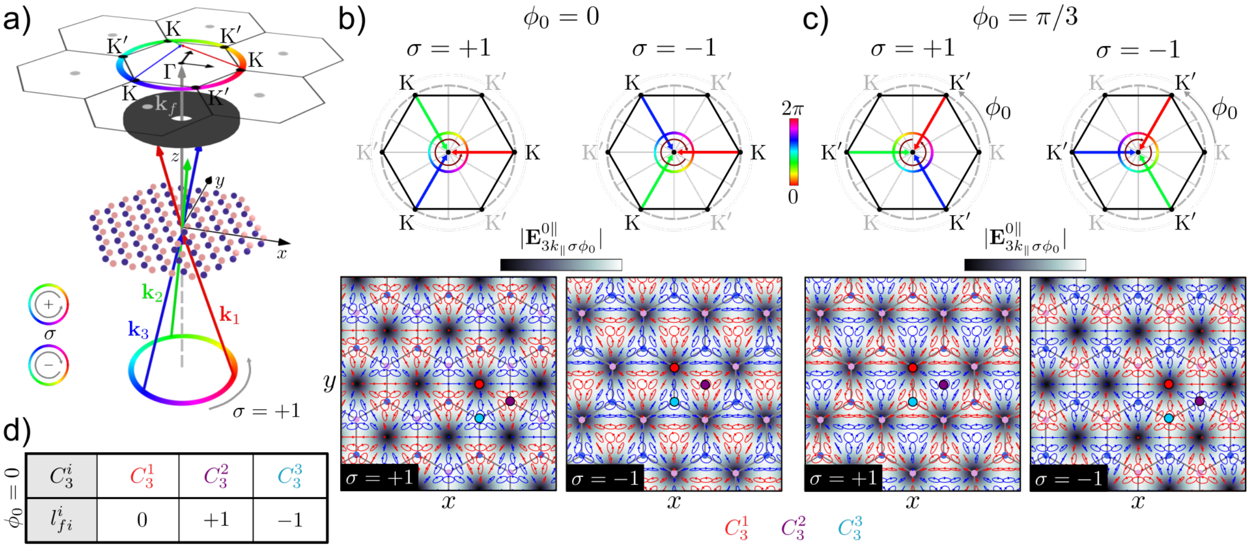

Figure 5.2: Transition electric fields involving three-fold pinwheel states. a) Scheme showing a transition from the $|P = 3, k_\|, \sigma = +1, \phi_0\rangle$ pinwheel state to $|\mathbf{k}_f^\| = \mathbf{0}\rangle$. b) and c) show in-plane magnitudes (color maps) and polarization textures (polarization ellipses) of $\mathbf{E}^{0\|}_{3k_\|\sigma\phi_0}(\mathbf{x}_\|, z = 0)$ associated with transitions $|P = 3, k_\| = \mathrm{K}, \sigma = \pm 1, \phi_0\rangle \rightarrow |\mathbf{k}_f^\| = \mathbf{0}\rangle$ at $\phi_0 = 0$ and $\phi_0 = \pi/3$, respectively. Red (blue) polarization ellipses indicate anticlockwise (clockwise) elliptical polarization rotation, and $\mathbf{R}_0 = -a/2\ \hat{\mathbf{y}}$. d) Total PAM l^i_{fi} of the transition field relative to the C_3^i ($i = 1, 2, 3$) rotation centers marked in panel (b) for $\phi_0 = 0$.

transition field associated with this situation is [238]

$$\mathbf{E}^0_{\mathbf{q},\mathbf{k}+\mathbf{G}\kappa} = \frac{4\pi i e}{L^3}\frac{L}{v_i}\frac{\mathbf{k}+\mathbf{G}}{|\mathbf{k}+\mathbf{G}|^2}\, e^{i(\mathbf{k}+\mathbf{G})\cdot\mathbf{r}_\kappa}\delta_{\mathbf{k}+\mathbf{G},\mathbf{q}}, \tag{5.2}$$

which is linearly polarized along the recoil direction $\hat{\mathbf{q}}$. The rate of phonon mode excitation is dictated by $\tilde{\mathcal{F}}_\lambda(\mathbf{q}) \propto \boldsymbol{\xi}^*_{\lambda\kappa} \cdot \mathbf{E}^0_{\mathbf{q},\mathbf{k}+\mathbf{G}\kappa} \propto \boldsymbol{\xi}^*_{\lambda\kappa} \cdot \hat{\mathbf{q}}$. As a consequence, the linearly polarized transition field couples identically to circularly polarized in-plane phonons, and it is not possible to distinguish the PAM of the phonon modes at K and K′ points from q-EEL spectra alone. Indeed, spectral lineouts of the double differential cross section (DDCS) [3, 193] at the K and K′ points from Fig. 5.1b are shown in Fig. 5.1d to be indistinguishable.

It is perhaps natural to consider employing prototypical free electron states that carry well-defined units of intrinsic OAM, e.g., Bessel and Laguerre-Gauss beams [70, 71, 239]. Previous works have demonstrated the ability to monitor OAM exchange between target sample and probing electron through careful pre- and post-selection of the OAM state of the free electrons [74, 76–78, 96, 235, 236]. However, this strategy is also problematic in the present case, since the reciprocal space wave function densities of these free electron states are azimuthally symmetric, leading to the inability to selectively probe the K or K′ points. To circumvent this challenge, we introduce pinwheel initial states $|P\, k_{\parallel}\, \sigma\, \phi_0\rangle$ of the free electron probe defined as

$$\psi_{Pk_{\parallel}\sigma\phi_0}(\mathbf{x}) = \frac{1}{\sqrt{P}} \sum_{j=1}^{P} e^{\sigma i \phi_j} L^{-3/2} e^{i\mathbf{k}_j\cdot\mathbf{x}}, \tag{5.3}$$

which are composed of P phased plane wave components with identical in-plane projection $k_{\parallel} = |\mathbf{k}_{\parallel}|$ and phases $\phi_j = (2\pi/P)j + \phi_0$ winding either counterclockwise ($\sigma = +1$) or clockwise ($\sigma = -1$). The constituent wave vectors for such an incident state are $\mathbf{k}_j^i = (k_{\parallel}^i \cos\phi_j,\, k_{\parallel}^i \sin\phi_j,\, k_z^i)$, with $k_i^2 = k_z^{i2} + k_{\parallel}^{i2}$. For 60 keV probing electrons typical of STEM EEL spectroscopy, the plane waves contributing to the pinwheel superposition states require convergence angles of $\theta_c \sim 13.5$ mrad for $k_{\parallel}$ at the hBN K/K′ points, while relative phases may be imprinted using techniques to shape transverse free electron wave functions currently under development [229][230–234].

By preparing an incoming pinwheel state and post-selecting the on-axis plane wave state with $\mathbf{k}_{\parallel}^f = \mathbf{0}$, as depicted in Fig. 5.2a using a spatial filter in the Fourier plane, the measured inelastic scattering process will be composed of P phased momentum recoils with $\mathbf{q}_{j\parallel} = \mathbf{k}_{j\parallel}^i$, and the transition field has the form [238]

$$\mathbf{E}^0_{Pk_{\parallel}\sigma\phi_0,\mathbf{k}+\mathbf{G}\kappa} = \frac{4\pi i e}{L^3}\frac{L}{v_i}\frac{1}{\sqrt{P}} \sum_{j=1}^{P} \frac{\mathbf{q}_j}{|\mathbf{q}_j|^2} e^{\sigma i \phi_j} e^{i(\mathbf{k}+\mathbf{G})\cdot(\mathbf{r}_\kappa - \mathbf{R}_0)} \delta_{\mathbf{k}+\mathbf{G},\mathbf{q}_j}. \tag{5.4}$$

Here, $\mathbf{R}_0$ dictates the displacement of the transition field interference pattern in the xy plane relative to some arbitrarily placed origin, which we take as the center of a real-space unit cell. In close analogy to topological electromagnetic vorticies created by interfering free space [203, 204] and evanescent [197, 198, 205–207] electromagnetic waves with controlled geometric phase, the in-plane polarization of the transition field $\mathbf{E}^{0\|}_{Pk_\|\sigma\phi_0}(\mathbf{x})$ consists of a 2D periodic array of field vorticies. The presently discussed topological field textures are distinguished from those previously reported in that the transition field is sourced by the charge density associated with the probing free electron transition, leading to field texture periodicity on the $\sim$ Å length scale. For the case $P = 3$ and $k_\| = \mathrm{K}, \mathrm{K}'$, the phased momentum transfers have the same three-fold rotational reciprocal space symmetry as the K and K′ phonons [9, 199], and the real space polarization array has hexagonal symmetry with unit cell dimensions matching those of the atomic crystal as presented in Fig. 5.2b for $\phi_0 = 0$. Superimposed above the 2D $|\mathbf{E}^{0\|}_{3k_\|\sigma\phi_0}(\mathbf{x}_\|, z = 0)|$ maps are polarization ellipses colored red (blue) to indicate anticlockwise (clockwise) polarization rotation. In close analogy to the situation encountered for valley phonons in 2D atomic crystals with hexagonal symmetry, the in-plane transition field has well-defined PAM $l^i_{fi} \in \{-1, 0, +1\}$ relative to any of the three distinct C^i_3 $(i = 1, 2, 3)$ rotation centers marked with colored dots in Figs. 5.2b,c [238]. Reversing the winding direction of the plane wave phases by $\sigma = +1 \leftrightarrow \sigma = -1$ leads to a spatial shift of the field nodes relative to the atomic crystal sites. As a consequence, l^i_{fi} does not depend on the value of σ, and l^i_{fi} is tabulated in Fig. 5.2d for $\phi_0 = 0$. The transition fields shown in Fig. 2b,c exhibit spin-momentum locking in the sense that simultaneous exchange of $\sigma = +1 \leftrightarrow \sigma = -1$ and $\phi_0 = 0 \leftrightarrow \phi_0 = \pi/3$, which is equivalent to $\mathrm{K} \leftrightarrow \mathrm{K}'$, yields the same spatial in-plane field intensity profile, with regions of clockwise and anticlockwise polarization rotation interchanged. This property reflects the fact that $l^i_{fi} \to -l^i_{fi}$ when $\phi_0 = 0 \to \pi/3$ [238].

The ability of the identified free electron transitions to generate electric fields that mirror the spin texture and spin-momentum locking of the hBN chiral phonons makes it possible to leverage the former to directly probe the latter. In particular, spatially scanning the transition field relative to the atomic crystal by changing $\mathbf{R}_0$ leads to either alignment, or varying degrees of misalignment, of the three C_3 axes of the transition field with those of the atomic crystal. When the two groups of C_3 axes are aligned, the PAM of both the transition field and the phonons can be simultaneously well-defined relative to a common origin, and coupling occurs between transition and phonon displacement fields with equal

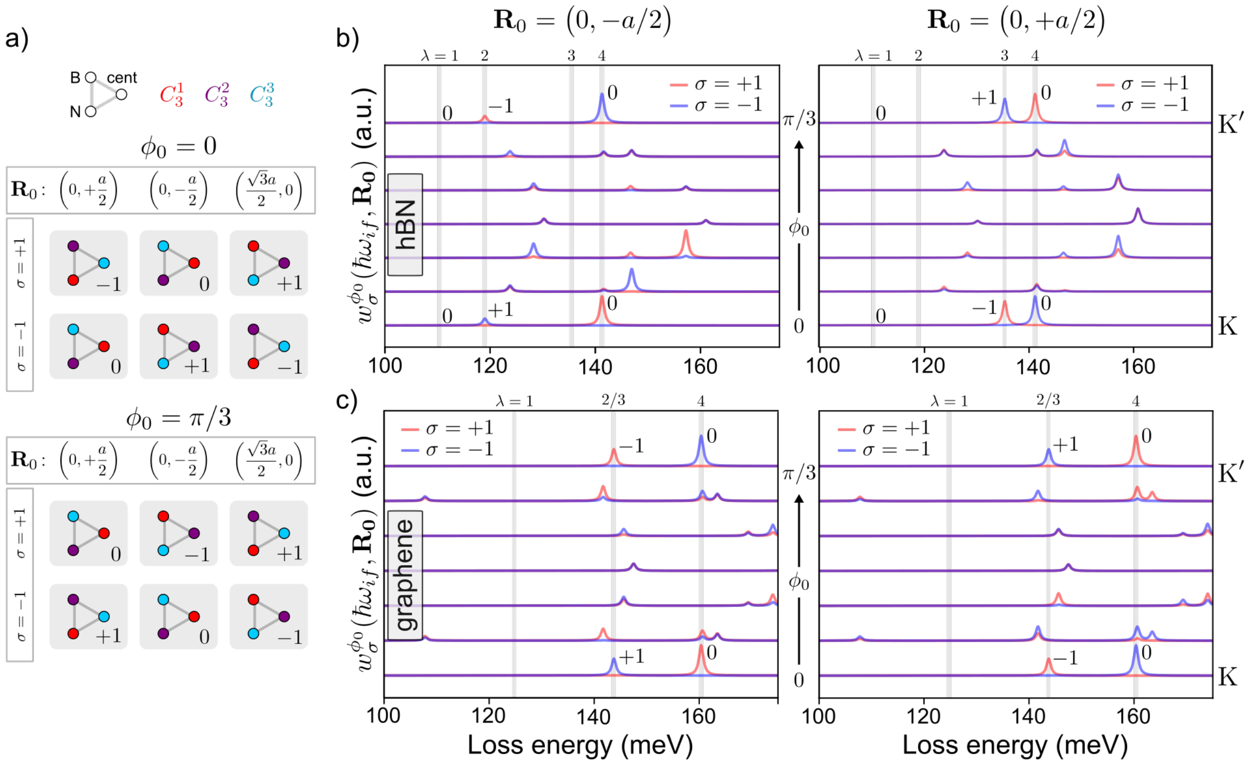

Figure 5.3: Chiral phonon discrimination with phase shaped electrons. a) Configuration tables specifying the identities of co-located atomic crystal and transition field C_3 axes for $\mathbf{R}_0 = \{(0, \pm a/2), (\sqrt{3}a/2, 0)\}$, $\sigma = \pm 1$, and $\phi_0 = \{0, \pi/3\}$. Circles at the vertices of each triangle represent B, N, and center (cent) atomic crystal positions, while circle color indicates which of the transition field C_3^i axes resides at each site. The integer to the lower right of each diagram indicates l_{fi}^{cent}. b) Calculated transition rates $w_\sigma^{\phi_0}(\hbar\omega_{if}, \mathbf{R}_0)$ for incoming pinwheel states transitioning to the on-axis plane wave state as a function of loss energy and $0 \leq \phi_0 \leq \pi/3$ for an hBN monolayer with $\mathbf{R}_0 = (0, \pm a/2)$. Red (blue) traces indicate $\sigma = +1$ ($\sigma = -1$). Integers adjacent to spectral features at K/K′ indicate the l_{fi}^{cent} from (a) relevant to each peak. c) Same as (b), but for monolayer graphene. All calculations assume a vacuum background environment and zero temperature. An empirical phonon damping rate of $\eta = 1$ meV/$\hbar$ is included.

PAM as required by PAM conservation. Conversely, when the transition field and atomic crystal C_3 axes are misaligned, the PAMs of the phonon branches cease to be well-defined relative to the C_3 axis of the probe, and exchange of intrinsic and extrinsic PAM occurs.

When $\mathbf{R}_0 \in \{(0, \pm a/2), (\sqrt{3}a/2, 0)\}$, the transition field C_3^i and atomic crystal rotation center positions coincide, with the particular value of i at each site dictated by the other parameters characterizing the transition field, i.e., $\sigma = \pm 1$ and $\phi_0 \in \{0, \pi/3\}$. The possible configurations of co-located C_3 axes are pictorially represented in Fig. 5.3a. For example, when $\mathbf{R}_0 = (0, -a/2)$, $\sigma = +1$, and $\phi_0 = 0$, it is the C_3^1 transition field axis at the location of the C_3^{cent} atomic crystal rotation center. Therefore, since $l_{fi}^1 = 0$, this transition field couples only to valley phonons with PAM $l_\lambda^{\text{cent}} = 0$. However, for $\mathbf{R}_0 = (0, -a/2)$, $\sigma = -1$, and $\phi_0 = 0$, C_3^2 coincides with C_3^{cent}, and phonons with PAM $l_\lambda^{\text{cent}} = +1$ are excited. This is precisely the behavior exhibited by the corresponding state- and energy-resolved transition rates $w_\sigma^{\phi_0}(\hbar\omega_{if}, \mathbf{R}_0)$ presented in Fig. 5.3b for hBN, which are evaluated using Eqs. (5.1) and (5.4). Red and blue traces correspond to $\sigma = +1$ and $\sigma = -1$, respectively. For $\mathbf{R}_0 = (0, -a/2)$ and $\phi_0 = 0$, the red trace shows features at the energies of modes $\lambda = 1$ and $\lambda = 4$, which have PAM $l_\lambda^{\text{cent}} = 0$, while the blue trace exhibits a single peak at mode $\lambda = 2$ with $l_\lambda^{\text{cent}} = +1$. Meanwhile, for $\mathbf{R}_0 = (0, +a/2)$ and $\phi_0 = 0$, in agreement with PAM conservation considerations encoded into the table in Fig. 5.3a, the $\sigma = +1$ and $\sigma = -1$ transition fields couple to valley phonons with PAM $l_\lambda^{\text{cent}} = -1$ and $l_\lambda^{\text{cent}} = 0$, respectively. Using $l_{fi}^{\text{cent}} \to -l_{fi}^{\text{cent}}$ when $\phi_0 = 0 \to \pi/3$, and $l_\lambda^{\text{cent}} \to -l_\lambda^{\text{cent}}$ when $\mathrm{K} \to \mathrm{K}'$, the spectra in Fig. 5.3b at $\phi_0 = \pi/3$ can likewise be rationalized in terms of PAM conservation. Therefore, given the ability to perform the identified pre- and post-selected pinwheel state measurements with control over $\mathbf{R}_0$, σ, and ϕ_0, it possible to perform energy-, valley, and PAM-resolved inelastic free electron scattering measurements capable of accessing valley phonons at the BZ corners directly.

As a point of comparison, Fig. 5.3c considers monolayer graphene, where the presence of parity symmetry requires modes $\lambda = 2, 3$ to be degenerate at the K/K' valleys. Although eigenvectors $\boldsymbol{\xi}_{\lambda=2,3}(\mathbf{k}_\parallel = \mathrm{K}/\mathrm{K}')$ can be defined with well-defined parity, parity and PAM operators do not commute. Nevertheless, linear combinations of the parity states can be taken to construct eigenvectors in this degenerate space with well-defined PAM. These particular eigenvectors have the same symmetries as those encountered for hBN, i.e., $\boldsymbol{\xi}_{\lambda=2}$ and $\boldsymbol{\xi}_{\lambda=3}$ exhibit circular motion of carbon atoms on one or the other atomic sites, respectively, while the other atom remains stationary at its equilibrium position. As a consequence, at the K valleys, these degenerate modes have total PAM $l^{\text{cent}}_{\lambda=2} = +1$ and $l^{\text{cent}}_{\lambda=3} = -1$. Critically, Figs. 5.3b,c show that by comparing the PAM-resolved loss spectra measured at $\mathbf{R}_0 = (0, \pm a/2)$ and $\sigma = \pm 1$, it is possible to directly assess non-degeneracy of valley phonon modes with PAM $l^{\text{cent}}_{\lambda} = \pm 1$ introduced in the absence of parity symmetry. Spatial maps of $w^{\phi_0}_{\sigma}(\hbar\omega_{if}, \mathbf{R}_0)$ for hBN and graphene and $\mathbf{R}_0$ varied throughout the real-space unit cell are presented in the SM [238].

Chiral phonons with valley pseudospin degrees of freedom and well-defined PAM underlie a diversity of fundamental condensed matter physics phenomena, material properties, and downstream technologies exploiting unidirectional and lossless phonon propagation in the infrared. However, direct characterization of chiral phonons has remained an outstanding challenge [222] owing to the small linear momentum of light and the absence of obvious polarization degrees of freedom of massive particles. Here we show how pre- and post-selection of pinwheel free electron states during inelastic scattering overcomes these limitations and introduces a new PAM degree of freedom enabling tracking of PAM exchange between probe and sample. By tailoring such pinwheel states to generate 2D periodic arrays of in-plane field vortices with Å-scale polarization textures, we introduce a strategy for direct and selective detection of phonon spin textures of the desired chiral mode symmetries at the K/K′ valleys using phase-structured free electrons. Other material systems hosting chiral phonons with various composition, symmetry, and dimensionality could be characterized using generalizations of the proposed inelastic scattering measurements.

5.3 Acknowledgments

All work was supported by the U.S. Department of Energy (DOE), Office of Science, Office of Basic Energy Sciences (BES), Materials Sciences and Engineering Division under Award No. DOE BES DE-SC0022921.

BIBLIOGRAPHY

[1] Matthew Hershey, Haihua Liu, Xiaofei Guo, Andrew W. Rossi, Marc R. Bourgeois, Benjamin D. Clark, Thomas E. Gage, Ilke Arslan, David J. Masiello, and Dayne F. Swearer. Probing plasmonic near-fields in oxide-modified aluminum nanocubes using photon-induced near-field electron microscopy. *ACS Photonics*, 12(11):6002–6010, 2025.

[2] Marc R. Bourgeois, Andrew W. Rossi, and David J. Masiello. Strategy for direct detection of chiral phonons with phase-structured free electrons. *Phys. Rev. Lett.*, 134(2):026902, 2025.

[3] Andrew W. Rossi, Marc R. Bourgeois, Caleb Walton, and David J. Masiello. Probing the polarization of low-energy excitations in 2D materials from atomic crystals to nanophotonic arrays using momentum-resolved electron energy loss spectroscopy. *Nano Lett.*, 24(25):7748–7756, 2024.

[4] Vishal Kumar, Andrew W. Rossi, Zachary R. Lawson, Robert D. Neal, Jordan A. Hachtel, Svetlana Neretina, David J. Masiello, and Jon P. Camden. Infrared near-field spectroscopy of gold nanotriangle fabry-pérot resonances. *J. Phys. Chem. C*, 127(14):6777–6784, 2023.

[5] Marc R. Bourgeois, Andrew W. Rossi, Siamak Khorasani, and David J. Masiello. Optical control over thermal distributions in topologically trivial and non-trivial plasmon lattices. *ACS Photonics*, 9(11):3656–3667, 2022.

[6] David A. Garfinkel, Vasudevan Iyer, Robyn Seils, Grace Pakeltis, Marc R. Bourgeois, Andrew W. Rossi, Clay Klein, Benjamin J. Lawrie, David J. Masiello, and Philip D. Rack. Visualizing electric and magnetic field coupling in au-nanorod trimer structures via stimulated electron energy gain and cathodoluminescence spectroscopy: Implications for meta-atom imaging. *ACS Appl. Nano Mater.*, 5(2):1798–1807, 2022.

[7] Marc R Bourgeois, Andrew W Rossi, Matthieu Chalifour, Charles Cherqui, and David J Masiello. Lattice kerker effect with plasmonic oligomers. *J. Phys. Chem. C*, 125(34):18817–18826, 2021.

[8] Zhengguang Lu, Tonghang Han, Yuxuan Yao, Aidan P Reddy, Jixiang Yang, Junseok Seo, Kenji Watanabe, Takashi Taniguchi, Liang Fu, and Long Ju. Fractional quantum anomalous hall effect in multilayer graphene. *Nature*, 626(8000):759–764, 2024.

[9] Lifa Zhang and Qian Niu. Chiral phonons at high-symmetry points in monolayer hexagonal lattices. *Phys. Rev. Lett.*, 115(11):115502, 2015.

[10] Ankun Yang, Thang B Hoang, Montacer Dridi, Claire Deeb, Maiken H Mikkelsen, George C Schatz, and Teri W Odom. Real-time tunable lasing from plasmonic nanocavity arrays. *Nat. Commun.*, 6:6939, 2015.

[11] R. Guo, M. Nečada, T. K. Hakala, A. I. Väkeväinen, and P. Törmä. Lasing at k points of a honeycomb plasmonic lattice. *Phys. Rev. Lett.*, 122:013901, 2019.

[12] Xitlali G Juarez, Ran Li, Jun Guan, Thaddeus Reese, Richard D Schaller, and Teri W Odom. M-point lasing in hexagonal and honeycomb plasmonic lattices. *ACS Photonics*, 9(1):52–58, 2022.

[13] Kazuyoshi Hirose, Yong Liang, Yoshitaka Kurosaka, Akiyoshi Watanabe, Takahiro Sugiyama, and Susumu Noda. Watt-class high-power, high-beam-quality photonic-crystal lasers. *Nat. Photonics*, 8(5):406–411, 2014.

[14] Jinhua Hong, Ryosuke Senga, Thomas Pichler, and Kazu Suenaga. Probing exciton dispersions of freestanding monolayer WSe_2 by momentum-resolved electron energy-loss spectroscopy. *Phys. Rev. Lett.*, 124(8):087401, 2020.

[15] Kin Fai Mak and Jie Shan. Photonics and optoelectronics of 2d semiconductor transition metal dichalcogenides. *Nat. Photonics*, 10(4):216–226, 2016.

[16] Jason S Ross, Sanfeng Wu, Hongyi Yu, Nirmal J Ghimire, Aaron M Jones, Grant Aivazian, Jiaqiang Yan, David G Mandrus, Di Xiao, Wang Yao, and Xiaodong Xu.

Electrical control of neutral and charged excitons in a monolayer semiconductor. *Nat. Commun.*, 4(1):1474, 2013.

[17] Anshul Kogar, Melinda S. Rak, Sean Vig, Ali A. Husain, Felix Flicker, Young Il Joe, Luc Venema, Greg J. MacDougall, Tai C. Chiang, Eduardo Fradkin, Jasper van Wezel, and Peter Abbamonte. Signatures of exciton condensation in a transition metal dichalcogenide. *Science*, 358(6368):1314–1317, 2017.

[18] N Sethulakshmi, Avanish Mishra, Pulickel M Ajayan, Yoshiyuki Kawazoe, Ajit K Roy, Abhishek K Singh, and Chandra Sekhar Tiwary. Magnetism in two-dimensional materials beyond graphene. *Mater. Today*, 27:107–122, 2019.

[19] Magnetic Gibertini, Maciej Koperski, Alberto F Morpurgo, and Konstantin S Novoselov. Magnetic 2D materials and heterostructures. *Nat. Nanotech.*, 14(5):408–419, 2019.

[20] Guillaume Baffou, Pascal Berto, Esteban Bermúdez Ureña, Romain Quidant, Serge Monneret, Julien Polleux, and Hervé Rigneault. Photoinduced heating of nanoparticle arrays. *ACS Nano*, 7(8):6478–6488, 2013.

[21] Jianing Chen, Michela Badioli, Pablo Alonso-González, Sukosin Thongrattanasiri, Florian Huth, Johann Osmond, Marko Spasenović, Alba Centeno, Amaia Pesquera, Philippe Godignon, Amaia Zurutuza Elorza, Nicolas Camara, F Javier García de Abajo, Rainer Hillenbrand, and Frank H L Koppens. Optical nano-imaging of gate-tunable graphene plasmons. *Nature*, 487(7405):77–81, 2012.

[22] Ming Liu, Xiaobo Yin, Erick Ulin-Avila, Baisong Geng, Thomas Zentgraf, Long Ju, Feng Wang, and Xiang Zhang. A graphene-based broadband optical modulator. *Nature*, 474(7349):64–67, 2011.

[23] Francesco Bonaccorso, Zhipei Sun, Tawfique Hasan, and AC Ferrari. Graphene photonics and optoelectronics. *Nat. Photonics*, 4(9):611–622, 2010.

[24] Seba Sara Varghese, Saino Hanna Varghese, Sundaram Swaminathan, Krishna Kumar Singh, and Vikas Mittal. Two-dimensional materials for sensing: graphene and beyond. *Electronics*, 4(3):651–687, 2015.

[25] Jie You, Yukun Luo, Jie Yang, Jianghua Zhang, Ke Yin, Ke Wei, Xin Zheng, and Tian Jiang. Hybrid/integrated silicon photonics based on 2D materials in optical communication nanosystems. *Laser Photonics Rev.*, 14(12):2000239, 2020.

[26] Xiaolong Liu and Mark C Hersam. 2D materials for quantum information science. *Nat. Rev. Mater.*, 4(10):669–684, 2019.

[27] Neil W Ashcroft and ND Mermin. *Solid State Physics*. Holt-Saunders, 1976.

[28] Charles Cherqui, Marc R Bourgeois, Danqing Wang, and George C Schatz. Plasmonic surface lattice resonances: theory and computation. *Acc. Chem. Res.*, 52(9):2548–2558, 2019.

[29] Francisco Freire-Fernández, Sang-Min Park, Max JH Tan, and Teri W Odom. Plasmonic lattice lasers. *Nat. Rev. Mater.*, pages 1–13, 2025.

[30] DK Saldin and PL De Andres. Holographic leed. *Phys. Rev. Lett.*, 64(11):1270, 1990.

[31] RJ Hamers. Atomic-resolution surface spectroscopy with the scanning tunneling microscope. *Annu. Rev. Phys. Chem.*, 40(1):531–559, 1989.

[32] Robert A Wolkow. Direct observation of an increase in buckled dimers on si(001) at low temperature. *Phys. Rev. Lett.*, 68(17):2636, 1992.

[33] Ondrej L Krivanek, Matthew F Chisholm, Valeria Nicolosi, Timothy J Pennycook, George J Corbin, Niklas Dellby, Matthew F Murfitt, Christopher S Own, Zoltan S Szilagyi, Mark P Oxley, et al. Atom-by-atom structural and chemical analysis by annular dark-field electron microscopy. *Nature*, 464(7288):571–574, 2010.

[34] Wu Zhou, Jaekwang Lee, Jagjit Nanda, Sokrates T Pantelides, Stephen J Pennycook, and Juan-Carlos Idrobo. Atomically localized plasmon enhancement in monolayer graphene. *Nat. Nanotechnol.*, 7(3):161–165, 2012.

[35] Ondrej L Krivanek, Tracy C Lovejoy, Niklas Dellby, Toshihiro Aoki, R W Carpenter, Peter Rez, Emmanuel Soignard, Jiangtao Zhu, Philip E Batson, Maureen J Lagos, Ray F Egerton, and Peter A Crozier. Vibrational spectroscopy in the electron microscope. *Nature*, 514(7521):209–212, 2014.

[36] Christian Dwyer, T Aoki, Peter Rez, SLY Chang, TC Lovejoy, and OL Krivanek. Electron-beam mapping of vibrational modes with nanometer spatial resolution. *Phys. Rev. Lett.*, 117(25):256101, 2016.

[37] Maureen J Lagos, Andreas Trügler, Ulrich Hohenester, and Philip E Batson. Mapping vibrational surface and bulk modes in a single nanocube. *Nature*, 543(7646):529–532, 2017.

[38] Fredrik S Hage, Rebecca J Nicholls, Jonathan R Yates, Dougal G McCulloch, Tracy C Lovejoy, Niklas Dellby, Ondrej L Krivanek, Keith Refson, and Quentin M Ramasse. Nanoscale momentum-resolved vibrational spectroscopy. *Sci. Adv.*, 4(6):eaar7495, 2018.

[39] Ryosuke Senga, Kazu Suenaga, Paolo Barone, Shigeyuki Morishita, Francesco Mauri, and Thomas Pichler. Position and momentum mapping of vibrations in graphene nanostructures. *Nature*, 573(7773):247–250, 2019.

[40] C. Kramberger, R. Hambach, C. Giorgetti, M. H. Rümmeli, M. Knupfer, J. Fink, B. Büchner, Lucia Reining, E. Einarsson, S. Maruyama, F. Sottile, K. Hannewald, V. Olevano, A. G. Marinopoulos, and T. Pichler. Linear plasmon dispersion in single-wall carbon nanotubes and the collective excitation spectrum of graphene. *Phys. Rev. Lett.*, 100(19):196803, 2008.

[41] Antonio Politano, Antonio Raimondo Marino, and Gennaro Chiarello. Phonon dispersion of quasi-freestanding graphene on pt(111). *J. Phys.-Condens. Mat.*, 24(10):104025, 2012.

[42] Antonio Politano, Fernando de Juan, Gennaro Chiarello, and Herbert A Fertig. Emer-

gence of an out-of-plane optical phonon (zo) kohn anomaly in quasifreestanding epitaxial graphene. *Phy. Rev. Lett.*, 115(7):075504, 2015.

[43] Antonio Politano. Spectroscopic investigations of phonons in epitaxial graphene. *Crit. Rev. Solid State*, 42(2):99–128, 2017.

[44] Jiade Li, Jiangxu Li, Jilin Tang, Zhiyu Tao, Siwei Xue, Jiaxi Liu, Hailin Peng, Xing-Qiu Chen, Jiandong Guo, and Xuetao Zhu. Direct observation of topological phonons in graphene. *Phys. Rev. Lett.*, 131(11):116602, 2023.

[45] Antonio Politano. On the fate of high-resolution electron energy loss spectroscopy (hreels), a versatile probe to detect surface excitations: Will the Phoenix rise again? *Phys. Chem. Chem. Phys.*, 23(46):26061–26069, 2021.

[46] Jiade Li, Li Wang, Yani Wang, Zhiyu Tao, Weiliang Zhong, Zhibin Su, Siwei Xue, Guangyao Miao, Weihua Wang, Hailin Peng, Jiandong Guo, and Xuetao Zhu. Observation of the nonanalytic behavior of optical phonons in monolayer hexagonal boron nitride. *Nat. Commun.*, 15(1):1938, 2024.

[47] A. Politano, V. M. Silkin, I. A. Nechaev, M. S. Vitiello, L. Viti, Z. S. Aliev, M. B. Babanly, G. Chiarello, P. M. Echenique, and E. V. Chulkov. Interplay of surface and dirac plasmons in topological insulators: The case of bi_2se_3. *Phys. Rev. Lett.*, 115:216802, 2015.

[48] A. Kogar, S. Vig, A. Thaler, M. H. Wong, Y. Xiao, D. Reig-i Plessis, G. Y. Cho, T. Valla, Z. Pan, J. Schneeloch, R. Zhong, G. D. Gu, T. L. Hughes, G. J. MacDougall, T.-C. Chiang, and P. Abbamonte. Surface collective modes in the topological insulators Bi_2Se_3 and $Bi_{0.5}Sb_{1.5}Te_{3-x}Se_x$. *Phys. Rev. Lett.*, 115:257402, 2015.

[49] Antonio Politano, Gennaro Chiarello, Barun Ghosh, Krishanu Sadhukhan, Chia-Nung Kuo, Chin Shan Lue, Vittorio Pellegrini, and Amit Agarwal. 3D Dirac Plasmons in the Type-II Dirac Semimetal $PtTe_2$. *Phys. Rev. Lett.*, 121:086804, 2018.

[50] Siwei Xue, Maoyuan Wang, Yong Li, Shuyuan Zhang, Xun Jia, Jianhui Zhou, Youguo

Shi, Xuetao Zhu, Yugui Yao, and Jiandong Guo. Observation of nodal-line plasmons in zrsis. *Phys. Rev. Lett.*, 127:186802, 2021.

[51] Bo Zhen, Chia Wei Hsu, Ling Lu, A Douglas Stone, and Marin Soljačić. Topological nature of optical bound states in the continuum. *Phys. Rev. Lett.*, 113(25):257401, 2014.

[52] Shaimaa I Azzam, Vladimir M Shalaev, Alexandra Boltasseva, and Alexander V Kildishev. Formation of bound states in the continuum in hybrid plasmonic-photonic systems. *Phys. Rev. Lett.*, 121(25):253901, 2018.

[53] Yao Liang, Kirill Koshelev, Fengchun Zhang, Han Lin, Shirong Lin, Jiayang Wu, Baohua Jia, and Yuri Kivshar. Bound states in the continuum in anisotropic plasmonic metasurfaces. *Nano Lett.*, 20(9):6351–6356, 2020.

[54] Jun Guan, Laxmi Kishore Sagar, Ran Li, Danqing Wang, Golam Bappi, Weijia Wang, Nicolas Watkins, Marc R. Bourgeois, Larissa Levina, Fengjia Fan, Sjoerd Hoogland, Oleksandr Voznyy, Joao Martins de Pina, Richard D. Schaller, George C. Schatz, Edward H. Sargent, and Teri W. Odom. Quantum dot-plasmon lasing with controlled polarization patterns. *ACS Nano*, 14(3):3426–3433, 2020.

[55] Yao Liang, Han Lin, Shirong Lin, Jiayang Wu, Weibai Li, Fei Meng, Yunyi Yang, Xiaodong Huang, Baohua Jia, and Yuri Kivshar. Hybrid anisotropic plasmonic metasurfaces with multiple resonances of focused light beams. *Nano Lett.*, 21(20):8917–8923, 2021.

[56] Son Tung Ha, Yuan Hsing Fu, Naresh Kumar Emani, Zhenying Pan, Reuben M Bakker, Ramón Paniagua-Domínguez, and Arseniy I Kuznetsov. Directional lasing in resonant semiconductor nanoantenna arrays. *Nat. Nanotechnol.*, 13(11):1042–1047, 2018.

[57] Sughra Mohamed, Jie Wang, Heikki Rekola, Janne Heikkinen, Benjamin Asamoah, Lei Shi, and Tommi K Hakala. Controlling topology and polarization state of lasing photonic bound states in continuum. *Laser Photonics Rev.*, 16(7):2100574, 2022.

[58] Wenjing Liu, Zhurun Ji, Yuhui Wang, Gaurav Modi, Minsoo Hwang, Biyuan Zheng, Volker J Sorger, Anlian Pan, and Ritesh Agarwal. Generation of helical topological exciton-polaritons. *Science*, 370(6516):600–604, 2020.

[59] Marc R Bourgeois, Elliot K Beutler, Siamak Khorasani, Nicole Panek, and David J Masiello. Nanometer-scale spatial and spectral mapping of exciton polaritons in structured plasmonic cavities. *Phys. Rev. Lett.*, 128(19):197401, 2022.

[60] Yueyang Chen, Shengnan Miao, Tianmeng Wang, Ding Zhong, Abhi Saxena, Colin Chow, James Whitehead, Dario Gerace, Xiaodong Xu, Su-Fei Shi, and Arka Majumdar. Metasurface integrated monolayer exciton polariton. *Nano Lett.*, 20(7):5292–5300, 2020.

[61] A. I. Väkeväinen, R. J. Moerland, H. T. Rekola, A.-P. Eskelinen, J.-P. Martikainen, D.-H. Kim, and P. Törmä. Plasmonic surface lattice resonances at the strong coupling regime. *Nano Lett.*, 14(4):1721–1727, 2014.

[62] L Shi, TK Hakala, HT Rekola, J-P Martikainen, RJ Moerland, and Päivi Törmä. Spatial coherence properties of organic molecules coupled to plasmonic surface lattice resonances in the weak and strong coupling regimes. *Phys. Rev. Lett.*, 112(15):153002, 2014.

[63] Denis G Baranov, Martin Wersall, Jorge Cuadra, Tomasz J Antosiewicz, and Timur Shegai. Novel nanostructures and materials for strong light-matter interactions. *ACS Photonics*, 5(1):24–42, 2018.

[64] Prashant Shekhar, Marek Malac, Vaibhav Gaind, Neda Dalili, Al Meldrum, and Zubin Jacob. Momentum-resolved electron energy loss spectroscopy for mapping the photonic density of states. *ACS Photonics*, 4(4):1009–1014, 2017.

[65] Hikaru Saito, Hugo Lourenço-Martins, Noémie Bonnet, Xiaoyan Li, Tracy C Lovejoy, Niklas Dellby, Odile Stéphan, Mathieu Kociak, and Luiz Henrique Galvão Tizei. Emergence of point defect states in a plasmonic crystal. *Phys. Rev. B*, 100(24):245402, 2019.

[66] PE Batson. A new surface plasmon resonance in clusters of small aluminum spheres. *Ultramicroscopy*, 9(3):277–282, 1982.

[67] Jaysen Nelayah, Mathieu Kociak, Odile Stéphan, F Javier García de Abajo, Marcel Tencé, Luc Henrard, Dario Taverna, Isabel Pastoriza-Santos, Luis M Liz-Marzán, and Christian Colliex. Mapping surface plasmons on a single metallic nanoparticle. *Nat. Phys.*, 3(5):348–353, 2007.

[68] F J García de Abajo. Optical excitations in electron microscopy. *Rev. Mod. Phys.*, 82(1):209, 2010.

[69] Charles Cherqui, Niket Thakkar, Guoliang Li, Jon P Camden, and David J Masiello. Characterizing localized surface plasmons using electron energy-loss spectroscopy. *Annu. Rev. Phys. Chem.*, 67:331–357, 2016.

[70] Masaya Uchida and Akira Tonomura. Generation of electron beams carrying orbital angular momentum. *Nature*, 464(7289):737–739, 2010.

[71] Johan Verbeeck, He Tian, and Peter Schattschneider. Production and application of electron vortex beams. *Nature*, 467(7313):301–304, 2010.

[72] Benjamin J McMorran, Amit Agrawal, Ian M Anderson, Andrew A Herzing, Henri J Lezec, Jabez J McClelland, and John Unguris. Electron vortex beams with high quanta of orbital angular momentum. *Science*, 331(6014):192–195, 2011.

[73] G M Vanacore, G Berruto, I Madan, E Pomarico, P Biagioni, R J Lamb, D McGrouther, O Reinhardt, I Kaminer, B Barwick, H Larocque, V Grillo, E Karimi, F J García de Abajo, and F Carbone. Ultrafast generation and control of an electron vortex beam via chiral plasmonic near fields. *Nat. Mater.*, 18(6):573–579, 2019.

[74] A Asenjo-Garcia and F J García de Abajo. Dichroism in the interaction between vortex electron beams, plasmons, and molecules. *Phys. Rev. Lett.*, 113(6):066102, 2014.

[75] Giulio Guzzinati, Armand Béché, Hugo Lourenço-Martins, Jérôme Martin, Mathieu Kociak, and Jo Verbeeck. Probing the symmetry of the potential of localized surface plasmon resonances with phase-shaped electron beams. *Nat. Commun.*, 8(1):1–8, 2017.

[76] Matteo Zanfrognini, Enzo Rotunno, Stefano Frabboni, Alicia Sit, Ebrahim Karimi, Ulrich Hohenester, and Vincenzo Grillo. Orbital angular momentum and energy loss characterization of plasmonic excitations in metallic nanostructures in tem. *ACS Photonics*, 6(3):620–627, 2019.

[77] Hugo Lourenço-Martins, Davy Gérard, and Mathieu Kociak. Optical polarization analogue in free electron beams. *Nat. Phys.*, 17(5):598–603, 2021.

[78] Marc R Bourgeois, Austin G Nixon, Matthieu Chalifour, Elliot K Beutler, and David J Masiello. Polarization-resolved electron energy gain nanospectroscopy with phase-structured electron beams. *Nano Lett.*, 22(17):7158–7165, 2022.

[79] Marc R. Bourgeois, Austin G. Nixon, Matthieu Chalifour, and David J. Masiello. Optical polarization analogs in inelastic free-electron scattering. *Sci. Adv.*, 9(51):eadj6038, 2023.

[80] Austin G. Nixon, Matthieu Chalifour, Marc R. Bourgeois, Michael Sanchez, and David J. Masiello. Inelastic scattering of transversely structured free electrons from nanophotonic targets: Theory and computation. *Phys. Rev. A*, 109:043502, 2024.

[81] Martin T Dove. *Introduction to Lattice Dynamics*. Cambridge University Press, 1993.

[82] Alexei A Maradudin. *Theory of Lattice Dynamics in the Harmonic Approximation*. Academic Press, 1971.

[83] Georg Kresse and Jürgen Hafner. Ab initio molecular dynamics for liquid metals. *Phys. Rev. B*, 47(1):558, 1993.

[84] Georg Kresse and Jürgen Furthmüller. Efficiency of ab-initio total energy calculations

for metals and semiconductors using a plane-wave basis set. *Comput. Mater. Sci.*, 6(1):15–50, 1996.

[85] Paolo Giannozzi, Stefano Baroni, Nicola Bonini, Matteo Calandra, Roberto Car, Carlo Cavazzoni, Davide Ceresoli, Guido L Chiarotti, Matteo Cococcioni, Ismaila Dabo, et al. Quantum espresso: a modular and open-source software project for quantum-simulations of materials. *J. Phys. Condens. Matter.*, 21(39):395502, 2009.

[86] Paolo Giannozzi, Oliviero Andreussi, Thomas Brumme, Oana Bunau, M Buongiorno Nardelli, Matteo Calandra, Roberto Car, Carlo Cavazzoni, Davide Ceresoli, Matteo Cococcioni, et al. Advanced capabilities for materials modelling with quantum espresso. *J. Phys. Condens. Matter.*, 29(46):465901, 2017.

[87] Alexey Bosak, Michael Krisch, Marcel Mohr, Janina Maultzsch, and Christian Thomsen. Elasticity of single-crystalline graphite: Inelastic x-ray scattering study. *Phys. Rev. B*, 75(15):153408, 2007.

[88] KH Michel and B Verberck. Theory of the evolution of phonon spectra and elastic constants from graphene to graphite. *Phys. Rev. B*, 78(8):085424, 2008.

[89] Anton Souslov, Andrea J Liu, and Tom C Lubensky. Elasticity and response in nearly isostatic periodic lattices. *Phys. Rev. Lett.*, 103(20):205503, 2009.

[90] Kai Sun, Anton Souslov, Xiaoming Mao, and Tom C Lubensky. Surface phonons, elastic response, and conformal invariance in twisted kagome lattices. *Proc. Natl. Acad. Sci. U.S.A.*, 109(31):12369–12374, 2012.

[91] Ulrich Hohenester, Andreas Trügler, Philip E Batson, and Maureen J Lagos. Inelastic vibrational bulk and surface losses of swift electrons in ionic nanostructures. *Phys. Rev. B*, 97(16):165418, 2018.

[92] Oliviero Bistoni, Paolo Barone, Emmanuele Cappelluti, Lara Benfatto, and Francesco Mauri. Giant effective charges and piezoelectricity in gapped graphene. *2D Materials*, 6(4):045015, 2019.

[93] C-Yu Wang, S Sharma, EKU Gross, and JK Dewhurst. Dynamical born effective charges. *Phys. Rev. B*, 106(18):L180303, 2022.

[94] Paolo Fachin, Francesco Macheda, Paolo Barone, and Francesco Mauri. Nearly quantized born effective charges as probes for the topological phase transition in the haldane and kane-mele models. *Phys. Rev. B*, 110(20):L201405, 2024.

[95] John D. Jackson. *Classical Electrodynamics Third Edition*. John Wiley & Sons, Inc., 1999.

[96] Marc R. Bourgeois, Austin G. Nixon, Matthieu Chalifour, and David J. Masiello. Optical polarization analogs in inelastic free-electron scattering. *Sci. Adv.*, 9(51):eadj6038, 2023.

[97] Jingjing Qiu and Wei David Wei. Surface plasmon-mediated photothermal chemistry. *J. Phys. Chem. C*, 118(36):20735–20749, 2014.

[98] Linyou Cao, David N Barsic, Alex R Guichard, and Mark L Brongersma. Plasmon-assisted local temperature control to pattern individual semiconductor nanowires and carbon nanotubes. *Nano Lett.*, 7(11):3523–3527, 2007.

[99] Diego Mateo, Jose Luis Cerrillo, Sara Durini, and Jorge Gascon. Fundamentals and applications of photo-thermal catalysis. *Chem. Soc. Rev.*, 50(3):2173–2210, 2021.

[100] Carmen Vázquez-Vázquez, Belén Vaz, Vincenzo Giannini, Moisés Pérez-Lorenzo, Ramon A Alvarez-Puebla, and Miguel A Correa-Duarte. Nanoreactors for simultaneous remote thermal activation and optical monitoring of chemical reactions. *J. Am. Chem. Soc.*, 135(37):13616–13619, 2013.

[101] Nan Zhou, Xianfan Xu, Aaron T Hammack, Barry C Stipe, Kaizhong Gao, Werner Scholz, and Edward C Gage. Plasmonic near-field transducer for heat-assisted magnetic recording. *Nanophotonics*, 3(3):141–155, 2014.

[102] Feng Cheng, Chuangtang Wang, Zhaoxian Su, Xinjun Wang, Ziqiang Cai, Nian X

Sun, and Yongmin Liu. All-optical manipulation of magnetization in ferromagnetic thin films enhanced by plasmonic resonances. *Nano Lett.*, 20(9):6437–6443, 2020.

[103] Janez Dolinšek, M Feuerbacher, M Jagodič, Z Jagličić, M Heggen, and K Urban. A thermal memory cell. *J. Appl. Phys.*, 106(4):043917, 2009.

[104] Run Hu, Shiyao Huang, Meng Wang, Liliang Zhou, Xiayao Peng, and Xiaobing Luo. Binary thermal encoding by energy shielding and harvesting units. *Phys. Rev. Appl.*, 10(5):054032, 2018.

[105] Raj Manik and Ajit Behera. Thermal encoding using shape memory alloy. *Mater. Today-Proc.*, 33:5709–5713, 2020.

[106] Yangbo Wu, Zhibo Qu, Ahmed Osman, Wei Cao, Ali Z Khokhar, Jordi Soler Penades, Otto L Muskens, Goran Z Mashanovich, and Milos Nedeljkovic. Mid-infrared nanometallic antenna assisted silicon waveguide based bolometers. *ACS Photonics*, 6(12):3253–3260, 2019.

[107] Xiang-Tian Kong, Larousse Khosravi Khorashad, Zhiming Wang, and Alexander O Govorov. Photothermal circular dichroism induced by plasmon resonances in chiral metamaterial absorbers and bolometers. *Nano Lett.*, 18(3):2001–2008, 2018.

[108] Xiaohua Huang, Prashant K Jain, Ivan H El-Sayed, and Mostafa A El-Sayed. Plasmonic photothermal therapy (pptt) using gold nanoparticles. *Lasers Med. Sci.*, 23(3):217–228, 2008.

[109] Moustafa RK Ali, Yue Wu, and Mostafa A El-Sayed. Gold-nanoparticle-assisted plasmonic photothermal therapy advances toward clinical application. *J. Phys. Chem. C*, 123(25):15375–15393, 2019.

[110] Guangyu Qiu, Zhibo Gai, Yile Tao, Jean Schmitt, Gerd A Kullak-Ublick, and Jing Wang. Dual-functional plasmonic photothermal biosensors for highly accurate severe acute respiratory syndrome coronavirus 2 detection. *ACS Nano*, 14(5):5268–5277, 2020.

[111] Guillaume Baffou and Romain Quidant. Thermo-plasmonics: using metallic nanostructures as nano-sources of heat. *Laser Photonics Rev.*, 7(2):171–187, 2013.

[112] Guillaume Baffou, Frank Cichos, and Romain Quidant. Applications and challenges of thermoplasmonics. *Nat. Mater.*, 19(9):946–958, 2020.

[113] Gregory V Hartland. Optical studies of dynamics in noble metal nanostructures. *Chem. Rev.*, 111(6):3858–3887, 2011.

[114] Alexander O Govorov, Wei Zhang, Timur Skeini, Hugh Richardson, Jaebeom Lee, and Nicholas A Kotov. Gold nanoparticle ensembles as heaters and actuators: melting and collective plasmon resonances. *Nanoscale Rese. Lett.*, 1(1):84–90, 2006.

[115] Liselotte Jauffred, Akbar Samadi, Henrik Klingberg, Poul Martin Bendix, and Lene B Oddershede. Plasmonic heating of nanostructures. *Chem. Rev.*, 119(13):8087–8130, 2019.

[116] Guillaume Baffou, Romain Quidant, and F J García de Abajo. Nanoscale control of optical heating in complex plasmonic systems. *ACS Nano*, 4(2):709–716, 2010.

[117] Zachary J Coppens, Wei Li, D Greg Walker, and Jason G Valentine. Probing and controlling photothermal heat generation in plasmonic nanostructures. *Nano Lett.*, 13(3):1023–1028, 2013.

[118] Larousse Khosravi Khorashad, Lucas V Besteiro, Zhiming Wang, Jason Valentine, and Alexander O Govorov. Localization of excess temperature using plasmonic hot spots in metal nanostructures: combining nano-optical antennas with the fano effect. *J. Phys. Chem. C*, 120(24):13215–13226, 2016.

[119] Christopher L Baldwin, Nicholas W Bigelow, and David J Masiello. Thermal signatures of plasmonic fano interferences: toward the achievement of nanolocalized temperature manipulation. *J. Phys. Chem. Lett.*, 5(8):1347–1354, 2014.

[120] Ujjal Bhattacharjee, Claire A West, Seyyed Ali Hosseini Jebeli, Harrison J Goldwyn, Xiang-Tian Kong, Zhongwei Hu, Elliot K Beutler, Wei-Shun Chang, Katherine A

Willets, Stephan Link, et al. Active far-field control of the thermal near-field via plasmon hybridization. *ACS Nano*, 13(8):9655–9663, 2019.

[121] Seyyed Ali Hosseini Jebeli, Claire A West, Stephen A Lee, Harrison J Goldwyn, Connor R Bilchak, Zahra Fakhraai, Katherine A Willets, Stephan Link, and David J Masiello. Wavelength-dependent photothermal imaging probes nanoscale temperature differences among subdiffraction coupled plasmonic nanorods. *Nano Lett.*, 21(12):5386–5393, 2021.

[122] Rui Guo, Tommi K Hakala, and Päivi Törmä. Geometry dependence of surface lattice resonances in plasmonic nanoparticle arrays. *Phys. Rev. B*, 95(15):155423, 2017.

[123] S. Zou, N. Janel, and G. C. Schatz. Silver nanoparticle array structures that produce remarkably narrow plasmon lineshapes. *J. Chem. Phys.*, 120:10871–10875, 2004.

[124] Vasyl G Kravets, Andrei V Kabashin, William L Barnes, and Alexander N Grigorenko. Plasmonic surface lattice resonances: a review of properties and applications. *Chem. Rev.*, 118(12):5912–5951, 2018.

[125] AD Humphrey and WL Barnes. Plasmonic surface lattice resonances in arrays of metallic nanoparticle dimers. *J. Opt.*, 18(3):035005, 2016.

[126] Alastair D Humphrey, Nina Meinzer, Timothy A Starkey, and William L Barnes. Surface lattice resonances in plasmonic arrays of asymmetric disc dimers. *ACS Photonics*, 3(4):634–639, 2016.

[127] S. Baur, S. Sanders, and A. Manjavacas. Hybridization of lattice resonances. *ACS Nano*, 12:1618–1629, 2018.

[128] Ran Li, Marc R Bourgeois, Charles Cherqui, Jun Guan, Danqing Wang, Jingtian Hu, Richard D Schaller, George C Schatz, and Teri W Odom. Hierarchical hybridization in plasmonic honeycomb lattices. *Nano Lett.*, 19(9):6435–6441, 2019.

[129] Ling Lu, John D Joannopoulos, and Marin Soljačić. Topological photonics. *Nat. Photonics*, 8(11):821–829, 2014.

[130] Marie S Rider, Álvaro Buendía, Diego R Abujetas, Paloma A Huidobro, José A Sánchez-Gil, and Vincenzo Giannini. Advances and prospects in topological nanoparticle photonics. *ACS Photonics*, 9(5):1483–1499, 2022.

[131] E. M. Purcell and C. R. Pennypacker. Scattering and absorption of light by nonspherical dielectric grains. *Astrophys. J.*, 186:705–714, 1973.

[132] Bruce T Draine and Piotr J Flatau. Discrete-dipole approximation for scattering calculations. *J. Opt. Soc. Am. A*, 11(4):1491–1499, 1994.

[133] K. Lance Kelly, Eduardo Coronado, Lin Lin Zhao, and George C. Schatz. The optical properties of metal nanoparticles: The influence of size, shape, and dielectric environment. *J. Phys. Chem. B*, 107(3):668–677, 2003.

[134] Khaled Metwally, Serge Mensah, and Guillaume Baffou. Isosbestic thermoplasmonic nanostructures. *ACS Photonics*, 4(6):1544–1551, 2017.

[135] DS Citrin. Plasmon-polariton transport in metal-nanoparticle chains embedded in a gain medium. *Opt. Lett.*, 31(1):98–100, 2006.

[136] Young-Ah Lucy Lee, Zeynab Mousavikhamene, Abhishek Kottaram Amrithanath, Suzanne M Neidhart, Sridhar Krishnaswamy, George C Schatz, and Teri W Odom. Programmable self-regulation with wrinkled hydrogels and plasmonic nanoparticle lattices. *Small*, 18(1):2103865, 2022.

[137] V. A. Markel. Coupled-dipole approach to scattering of light from a one-dimensional periodic dipole structure. *J. Mod. Opt.*, 40:2281–2291, 1993.

[138] Guillaume Baffou, Romain Quidant, and Christian Girard. Thermoplasmonics modeling: A green's function approach. *Phys. Rev. B*, 82(16):165424, 2010.

[139] S. R. Pocock, X. Xiao, P. A. Huidobro, and V. Giannini. Topological plasmonic chain with retardation and radiative effects. *ACS Photonics*, 5:2271–2279, 2018.

[140] Dezhuan Han, Yun Lai, Jian Zi, Zhao-Qing Zhang, and Che Ting Chan. Dirac spectra and edge states in honeycomb plasmonic lattices. *Phys. Rev. Lett.*, 102(12):123904, 2009.

[141] Alexander Poddubny, Andrey Miroshnichenko, Alexey Slobozhanyuk, and Yuri Kivshar. Topological majorana states in zigzag chains of plasmonic nanoparticles. *ACS Photonics*, 1(2):101–105, 2014.

[142] Ivan S Sinev, Ivan S Mukhin, Alexey P Slobozhanyuk, Alexander N Poddubny, Andrey E Miroshnichenko, Anton K Samusev, and Yuri S Kivshar. Mapping plasmonic topological states at the nanoscale. *Nanoscale*, 7(28):11904–11908, 2015.

[143] Li Wang, Ruo-Yang Zhang, Meng Xiao, Dezhuan Han, Che Ting Chan, and Weijia Wen. The existence of topological edge states in honeycomb plasmonic lattices. *New J. Phys.*, 18(10):103029, 2016.

[144] Dafei Jin, Thomas Christensen, Marin Soljačić, Nicholas X Fang, Ling Lu, and Xiang Zhang. Infrared topological plasmons in graphene. *Phys. Rev. Lett.*, 118(24):245301, 2017.

[145] Felix Bleckmann, Zlata Cherpakova, Stefan Linden, and Andrea Alberti. Spectral imaging of topological edge states in plasmonic waveguide arrays. *Phys. Rev. B*, 96(4):045417, 2017.

[146] Weifeng Zhang, Xianfeng Chen, and Fangwei Ye. Plasmonic topological insulators for topological nanophotonics. *Opt. Lett.*, 42(20):4063–4066, 2017.

[147] Pingping Qiu, Rui Liang, Weibin Qiu, Houbo Chen, Junbo Ren, Zhili Lin, Jia-Xian Wang, Qiang Kan, and Jiao-Qing Pan. Topologically protected edge states in graphene plasmonic crystals. *Opt. Express*, 25(19):22587–22594, 2017.

[148] W_P Su, JR Schrieffer, and Ao J Heeger. Solitons in polyacetylene. *Phys. Rev. Lett.*, 42(25):1698, 1979.

[149] Charles A Downing and Guillaume Weick. Topological plasmons in dimerized chains of nanoparticles: robustness against long-range quasistatic interactions and retardation effects. *Eur. Phys. J. B*, 91(10):253, 2018.

[150] VM Martinez Alvarez, JE Barrios Vargas, Matias Berdakin, and LEF Foa Torres. Topological states of non-hermitian systems. *Eur. Phys. J. Spec. Top.*, 227(12):1295–1308, 2018.

[151] François Fernique and Guillaume Weick. Plasmons in two-dimensional lattices of near-field coupled nanoparticles. *Phys. Rev. B*, 102(4):045420, 2020.

[152] Mengyao Li, Dmitry Zhirihin, Maxim Gorlach, Xiang Ni, Dmitry Filonov, Alexey Slobozhanyuk, Andrea Alù, and Alexander B Khanikaev. Higher-order topological states in photonic kagome crystals with long-range interactions. *Nat. Photonics*, 14(2):89–94, 2020.

[153] Simon R Pocock, Paloma A Huidobro, and Vincenzo Giannini. Bulk-edge correspondence and long-range hopping in the topological plasmonic chain. *Nanophotonics*, 8(8):1337–1347, 2019.

[154] J Zak. Berry's phase for energy bands in solids. *Phys. Rev. Lett.*, 62(23):2747, 1989.

[155] Craig F Bohren and Donald R Huffman. *Absorption and scattering of light by small particles*. John Wiley & Sons, 2008.

[156] Simon Lieu. Topological phases in the non-hermitian su-schrieffer-heeger model. *Phys. Rev. B*, 97(4):045106, 2018.

[157] Shunyu Yao and Zhong Wang. Edge states and topological invariants of non-hermitian systems. *Phys. Rev. Lett.*, 121(8):086803, 2018.

[158] BX Wang and CY Zhao. Topological phonon polaritons in one-dimensional non-hermitian silicon carbide nanoparticle chains. *Phys. Rev. B*, 98(16):165435, 2018.

[159] BX Wang and CY Zhao. Terahertz topological plasmon polaritons for robust temperature sensing. *Phys. Rev. Mater.*, 4(7):075201, 2020.

[160] BX Wang and CY Zhao. Topological photonic states in one-dimensional dimerized ultracold atomic chains. *Phys. Rev. A*, 98(2):023808, 2018.

[161] Ching Hua Lee and Ronny Thomale. Anatomy of skin modes and topology in non-hermitian systems. *Phys. Rev. B*, 99(20):201103, 2019.

[162] Annika Ott and Svend-Age Biehs. Radiative heat flux through a topological su-schrieffer-heeger chain of plasmonic nanoparticles. *Phys. Rev. B*, 102(11):115417, 2020.

[163] Ankun Yang, Alexander J Hryn, Marc R Bourgeois, Won-Kyu Lee, Jingtian Hu, George C Schatz, and Teri W Odom. Programmable and reversible plasmon mode engineering. *Proc. Natl. Acad. Sci. U. S. A.*, 113(50):14201–14206, 2016.

[164] Danqing Wang, Marc R Bourgeois, Won-Kyu Lee, Ran Li, Dhara Trivedi, Michael P Knudson, Weijia Wang, George C Schatz, and Teri W Odom. Stretchable nanolasing from hybrid quadrupole plasmons. *Nano Lett.*, 18(7):4549–4555, 2018.

[165] A. B. Evlyukhin, C. Reinhardt, U. Zywietz, and B. N. Chichkov. Collective resonances in metal nanoparticle arrays with dipole-quadrupole interactions. *Phys. Rev. B*, 85:245411, 2012.

[166] Charles Cherqui, Nicholas W. Bigelow, Alex Vaschillo, Harrison Goldwyn, and David J. Masiello. Combined tight-binding and numerical electrodynamics understanding of the stem/eels magneto-optical responses of aromatic plasmon-supporting metal oligomers. *ACS Photonics*, 1(10):1013–1024, 2014.

[167] Paul A Gabrys, Leonardo Z Zornberg, and Robert J Macfarlane. Programmable atom equivalents: atomic crystallization as a framework for synthesizing nanoparticle superlattices. *Small*, 15(26):1805424, 2019.

[168] Nicholas J Greybush, Iñigo Liberal, Ludivine Malassis, James M Kikkawa, Nader Engheta, Christopher B Murray, and Cherie R Kagan. Plasmon resonances in self-assembled two-dimensional au nanocrystal metamolecules. *ACS nano*, 11(3):2917–2927, 2017.

[169] Honghua U Yang, Jeffrey D'Archangel, Michael L Sundheimer, Eric Tucker, Glenn D Boreman, and Markus B Raschke. Optical dielectric function of silver. *Phys. Rev. B*, 91(23):235137, 2015.

[170] E Bauer. Low energy electron microscopy. *Rep. Prog. Phys.*, 57(9):895, 1994.

[171] Michael Endlich, Henrique P. C. Miranda, Alejandro Molina-Sánchez, Ludger Wirtz, and Jörg Kröger. Moiré-induced replica of graphene phonons on ir(111). *Ann. Phys.*, 526(9-10):372–380, 2014.

[172] Susanne Siebentritt, Roland Pues, Karl-Heinz Rieder, and Alexander M Shikin. Surface phonon dispersion in graphite and in a lanthanum graphite intercalation compound. *Phys. Rev. B*, 55(12):7927, 1997.

[173] T Aizawa, R Souda, S Otani, Y Ishizawa, and C Oshima. Anomalous bond of monolayer graphite on transition-metal carbide surfaces. *Phys. Rev. Lett.*, 64(7):768, 1990.

[174] F Moresco, M Rocca, T Hildebrandt, and M Henzler. Plasmon confinement in ultrathin continuous ag films. *Phys. Rev. Lett.*, 83(11):2238, 1999.

[175] H Petek and S Ogawa. Femtosecond time-resolved two-photon photoemission studies of electron dynamics in metals. *Prog. Surf. Sci.*, 56(4):239–310, 1997.

[176] Bogdan Diaconescu, Karsten Pohl, Luca Vattuone, Letizia Savio, Philip Hofmann, Vyacheslav M Silkin, Jose M Pitarke, Eugene V Chulkov, Pedro M Echenique, Daniel Farías, and Mario Rocca. Low-energy acoustic plasmons at metal surfaces. *Nature*, 448(7149):57–59, 2007.

[177] Aaron Bostwick, Taisuke Ohta, Thomas Seyller, Karsten Horn, and Eli Rotenberg. Quasiparticle dynamics in graphene. *Nat. Phys.*, 3(1):36–40, 2007.

[178] Kostya S Novoselov, Andre K Geim, Sergei V Morozov, De-eng Jiang, Yanshui Zhang, Sergey V Dubonos, Irina V Grigorieva, and Alexandr A Firsov. Electric field effect in atomically thin carbon films. *Science*, 306(5696):666–669, 2004.

[179] Kostya S Novoselov, Da Jiang, F Schedin, TJ Booth, VV Khotkevich, SV Morozov, and Andre K Geim. Two-dimensional atomic crystals. *Proc. Natl. Acad. Sci. U.S.A.*, 102(30):10451–10453, 2005.

[180] Michael Naguib, Murat Kurtoglu, Volker Presser, Jun Lu, Junjie Niu, Min Heon, Lars Hultman, Yury Gogotsi, and Michel W Barsoum. Two-dimensional nanocrystals produced by exfoliation of ti_3alc_2. *Adv. Mater.*, 23(37):4248–4253, 2011.

[181] Han Liu, Adam T Neal, Zhen Zhu, Zhe Luo, Xianfan Xu, David Tománek, and Peide D Ye. Phosphorene: an unexplored 2d semiconductor with a high hole mobility. *ACS Nano*, 8(4):4033–4041, 2014.

[182] J Maultzsch, S Reich, C Thomsen, H Requardt, and P Ordejón. Phonon dispersion in graphite. *Phys. Rev. Lett.*, 92(7):075501, 2004.

[183] M Mohr, J Maultzsch, Edib Dobardžić, S Reich, I Milošević, M Damnjanović, A Bosak, M Krisch, and C Thomsen. Phonon dispersion of graphite by inelastic x-ray scattering. *Phys. Rev. B*, 76(3):035439, 2007.

[184] G X Ni, A S McLeod, Z Sun, L Wang, L Xiong, K W Post, S S Sunku, B-Y Jiang, J Hone, C R Dean, M M Fogler, and D N Basov. Fundamental limits to graphene plasmonics. *Nature*, 557(7706):530–533, 2018.

[185] Ali A. Husain, Edwin W. Huang, Matteo Mitrano, Melinda S. Rak, Samantha I. Rubeck, Xuefei Guo, Hongbin Yang, Chanchal Sow, Yoshiteru Maeno, Bruno Uchoa, Tai C. Chiang, Philip E. Batson, Philip W. Phillips, and Peter Abbamonte. Pines' demon observed as a 3d acoustic plasmon in sr_2ruo_4. *Nature*, 621(7977):66–70, 2023.

[186] Sean Vig, Anshul Kogar, Matteo Mitrano, Ali A. Husain, Vivek Mishra, Melinda S. Rak, Luc Venema, Peter D. Johnson, Genda D. Gu, Eduardo Fradkin, Michael R. Norman, and Peter Abbamonte. Measurement of the dynamic charge response of materials using low-energy, momentum-resolved electron energy-loss spectroscopy (M-EELS). *SciPost Phys.*, 3:026, 2017.

[187] T. K. Hakala, Moilanen A. J., A. I. Väkeväinen, R. Guo, J.-P. Martikainen, K. S. Daskalakis, H. T. Rekola, A. Julku, and P. Törmä. Bose-einstein condensation in a plasmonic lattice. *Nat. Phys.*, 14:739–744, 2018.

[188] Anton Matthijs Berghuis, Gabriel W Castellanos, Shunsuke Murai, Jose Luis Pura, Diego R Abujetas, Erik van Heijst, Mohammad Ramezani, José A Sánchez-Gil, and Jaime Gómez Rivas. Room temperature exciton–polariton condensation in silicon metasurfaces emerging from bound states in the continuum. *Nano Lett.*, 23:5603–5609, 2023.

[189] K. Takeuchi and N. Yamamoto. Visualization of surface plasmon polariton waves in two-dimensional plasmonic crystal by cathodoluminescence. *Opt. Express*, 19(13):12365–12374, 2011.

[190] Hikaru Saito, Daichi Yoshimoto, Yuto Moritake, Taeko Matsukata, Naoki Yamamoto, and Takumi Sannomiya. Valley-polarized plasmonic edge mode visualized in the near-infrared spectral range. *Nano Lett.*, 21(15):6556–6562, 2021.

[191] Albert Polman, Mathieu Kociak, and F Javier García de Abajo. Electron-beam spectroscopy for nanophotonics. *Nat. Mater.*, 18(11):1158–1171, 2019.

[192] Roy J Glauber and M Lewenstein. Quantum optics of dielectric media. *Phys. Rev. A*, 43(1):467, 1991.

[193] J. J. Sakurai. *Modern Quantum Mechanics*. Benjamin/Cummings Publishing Company, 1985.

[194] Fernando de Juan, Antonio Politano, Gennaro Chiarello, and Herbert A Fertig. Symmetries and selection rules in the measurement of the phonon spectrum of graphene and related materials. *Carbon*, 85:225–232, 2015.

[195] RJ Nicholls, FS Hage, DG McCulloch, QM Ramasse, Keith Refson, and JR Yates. Theory of momentum-resolved phonon spectroscopy in the electron microscope. *Phys. Rev. B*, 99(9):094105, 2019.

[196] P. B. Johnson and R. W. Christy. Optical constants of the noble metals. *Phys. Rev. B*, 6:4370–4379, 1972.

[197] Yanan Dai, Zhikang Zhou, Atreyie Ghosh, Roger SK Mong, Atsushi Kubo, Chen-Bin Huang, and Hrvoje Petek. Plasmonic topological quasiparticle on the nanometre and femtosecond scales. *Nature*, 588(7839):616–619, 2020.

[198] Timothy J Davis, David Janoschka, Pascal Dreher, Bettina Frank, Frank-J Meyer zu Heringdorf, and Harald Giessen. Ultrafast vector imaging of plasmonic skyrmion dynamics with deep subwavelength resolution. *Science*, 368(6489):eaba6415, 2020.

[199] Hanyu Zhu, Jun Yi, Ming-Yang Li, Jun Xiao, Lifa Zhang, Chih-Wen Yang, Robert A Kaindl, Lain-Jong Li, Yuan Wang, and Xiang Zhang. Observation of chiral phonons. *Science*, 359(6375):579–582, 2018.

[200] Keisuke Inomata and Marc Kamionkowski. Chiral photons from chiral gravitational waves. *Phys. Rev. Lett.*, 123(3):031305, 2019.

[201] Usama Al Khawaja and Henk Stoof. Skyrmions in a ferromagnetic Bose-Einstein condensate. *Nature*, 411(6840):918–920, 2001.

[202] XZ Yu, W Koshibae, Y Tokunaga, K Shibata, Y Taguchi, N Nagaosa, and Y Tokura. Transformation between meron and skyrmion topological spin textures in a chiral magnet. *Nature*, 564(7734):95–98, 2018.

[203] Sijia Gao, Fiona C Speirits, Francesco Castellucci, Sonja Franke-Arnold, Stephen M Barnett, and Jörg B Götte. Paraxial skyrmionic beams. *Phys. Rev. A*, 102(5):053513, 2020.

[204] Yijie Shen, Yaonan Hou, Nikitas Papasimakis, and Nikolay I Zheludev. Supertoroidal light pulses as electromagnetic skyrmions propagating in free space. *Nat. Commun.*, 12(1):5891, 2021.

[205] S Tsesses, E Ostrovsky, K Cohen, B Gjonaj, NH Lindner, and G Bartal. Optical

skyrmion lattice in evanescent electromagnetic fields. *Science*, 361(6406):993–996, 2018.

[206] Luping Du, Aiping Yang, Anatoly V Zayats, and Xiaocong Yuan. Deep-subwavelength features of photonic skyrmions in a confined electromagnetic field with orbital angular momentum. *Nat. Phys.*, 15(7):650–654, 2019.

[207] Atreyie Ghosh, Sena Yang, Yanan Dai, and Hrvoje Petek. The spin texture topology of polygonal plasmon fields. *ACS Photonics*, 10(1):13–23, 2023.

[208] Shao-Yu Chen, Changxi Zheng, Michael S Fuhrer, and Jun Yan. Helicity-resolved Raman scattering of MoS_2, $MoSe_2$, WS_2, and WSe_2 atomic layers. *Nano Lett.*, 15(4):2526–2532, 2015.

[209] Hao Chen, Wei Zhang, Qian Niu, and Lifa Zhang. Chiral phonons in two-dimensional materials. *2D Mater.*, 6(1):012002, 2018.

[210] Hao Chen, Weikang Wu, Shengyuan A Yang, Xiao Li, and Lifa Zhang. Chiral phonons in kagome lattices. *Phys. Rev. B*, 100(9):094303, 2019.

[211] Nishchay Suri, Chong Wang, Yinhan Zhang, and Di Xiao. Chiral phonons in moiré superlattices. *Nano Lett.*, 21(23):10026–10031, 2021.

[212] Qianqian Wang, Si Li, Jiaojiao Zhu, Hao Chen, Weikang Wu, Weibo Gao, Lifa Zhang, and Shengyuan A Yang. Chiral phonons in lattices with C_4 symmetry. *Phys. Rev. B*, 105(10):104301, 2022.

[213] Tiantian Zhang and Shuichi Murakami. Chiral phonons and pseudoangular momentum in nonsymmorphic systems. *Phys. Rev. Research*, 4(1):L012024, 2022.

[214] J Fransson. Chiral phonon induced spin polarization. *Phys. Rev. Research*, 5(2):L022039, 2023.

[215] Hao Chen, Weikang Wu, Jiaojiao Zhu, Shengyuan A Yang, and Lifa Zhang. Propagating chiral phonons in three-dimensional materials. *Nano Lett.*, 21(7):3060–3065, 2021.

[216] Kyosuke Ishito, Huiling Mao, Yusuke Kousaka, Yoshihiko Togawa, Satoshi Iwasaki, Tiantian Zhang, Shuichi Murakami, Jun-ichiro Kishine, and Takuya Satoh. Truly chiral phonons in α-HgS. *Nat. Phys.*, 19(1):35–39, 2023.

[217] Hiroki Ueda, Mirian García-Fernández, Stefano Agrestini, Carl P Romao, Jeroen van den Brink, Nicola A Spaldin, Ke-Jin Zhou, and Urs Staub. Chiral phonons in quartz probed by x-rays. *Nature*, pages 1–5, 2023.

[218] G Grissonnanche, S Thériault, A Gourgout, M-E Boulanger, E Lefrançois, A Ataei, F Laliberté, M Dion, J-S Zhou, S Pyon, T Takayama, H. Takagi, N Doiron-Leyraud, and L Taillefer. Chiral phonons in the pseudogap phase of cuprates. *Nat. Phys.*, 16(11):1108–1111, 2020.

[219] Kyunghoon Kim, Eric Vetter, Liang Yan, Cong Yang, Ziqi Wang, Rui Sun, Yu Yang, Andrew H Comstock, Xiao Li, Jun Zhou, Lifa Zhang, Wei You, Dali Sun, and Jun Liu. Chiral-phonon-activated spin Seebeck effect. *Nat. Mater.*, 22(3):322–328, 2023.

[220] Seung Gyo Jeong, Jiwoong Kim, Ambrose Seo, Sungkyun Park, Hu Young Jeong, Young-Min Kim, Valeria Lauter, Takeshi Egami, Jung Hoon Han, and Woo Seok Choi. Unconventional interlayer exchange coupling via chiral phonons in synthetic magnetic oxide heterostructures. *Sci. Adv.*, 8(4):eabm4005, 2022.

[221] Hao Chen, Weikang Wu, Jiaojiao Zhu, Zhengning Yang, Weikang Gong, Weibo Gao, Shengyuan A Yang, and Lifa Zhang. Chiral phonon diode effect in chiral crystals. *Nano Lett.*, 22(4):1688–1693, 2022.

[222] Tingting Wang, Hong Sun, Xiaozhe Li, and Lifa Zhang. Chiral phonons: Prediction, verification, and application. *Nano Lett.*, 24(15):4311–4318, 2024.

[223] Jordan A Hachtel, Jingsong Huang, Ilja Popovs, Santa Jansone-Popova, Jong K Keum, Jacek Jakowski, Tracy C Lovejoy, Niklas Dellby, Ondrej L Krivanek, and Juan Carlos Idrobo. Identification of site-specific isotopic labels by vibrational spectroscopy in the electron microscope. *Science*, 363(6426):525–528, 2019.

[224] Andrew O'Hara, Benjamin Plotkin-Swing, Niklas Dellby, Juan Carlos Idrobo, Ondrej L Krivanek, Tracy C Lovejoy, and Sokrates T Pantelides. High-temperature phonons in h-BN: momentum-resolved vibrational spectroscopy and theory. *arXiv preprint arXiv:2310.13813*, 2023.

[225] Jiade Li, Li Wang, Yani Wang, Zhiyu Tao, Weiliang Zhong, Zhibin Su, Siwei Xue, Guangyao Miao, Weihua Wang, Hailin Peng, Jiandong Guo, and Xuetao Zhu. Observation of the nonanalytic behavior of optical phonons in monolayer hexagonal boron nitride. *Nat. Commun.*, 15(1):1938, 2024.

[226] J Yuan and N K Menon. Magnetic linear dichroism in electron energy loss spectroscopy. *J. Appl. Phys.*, 81(8):5087–5089, 1997.

[227] C Hébert and P Schattschneider. A proposal for dichroic experiments in the electron microscope. *Ultramicroscopy*, 96(3):463–468, 2003.

[228] P Schattschneider, S Rubino, C Hébert, J Rusz, J Kuneš, P Novák, E Carlino, M Fabrizioli, G Panaccione, and G Rossi. Detection of magnetic circular dichroism using a transmission electron microscope. *Nature*, 441(7092):486–488, 2006.

[229] T Niermann, J Verbeeck, and M Lehmann. Creating arrays of electron vortices. *Ultramicroscopy*, 136:165–170, 2014.

[230] Chu-Ping Yu, Francisco Vega Ibañez, Armand Béché, and Johan Verbeeck. Quantum wavefront shaping with a 48-element programmable phase plate for electrons. *SciPost Phys.*, 15(6):223, 2023.

[231] Armin Feist, Sergey V. Yalunin, Sascha Schäfer, and Claus Ropers. High-purity free-electron momentum states prepared by three-dimensional optical phase modulation. *Phys. Rev. Res.*, 2:043227, 2020.

[232] Ivan Madan, Veronica Leccese, Adam Mazur, Francesco Barantani, Thomas LaGrange, Alexey Sapozhnik, Phoebe M Tengdin, Simone Gargiulo, Enzo Rotunno, Jean-Christophe Olaya, Ido Kaminer, Vincenzo Grillo, F Javier García de Abajo,

Fabrizio Carbone, and Giovanni Maria Vanacore. Ultrafast transverse modulation of free electrons by interaction with shaped optical fields. *ACS Photonics*, 9(10):3215–3224, 2022.

[233] Tyler R Harvey, Jordan S Pierce, Amit K Agrawal, Peter Ercius, Martin Linck, and Benjamin J McMorran. Efficient diffractive phase optics for electrons. *New J. Phys.*, 16(9):093039, 2014.

[234] Shai Tsesses, Raphael Dahan, Kangpeng Wang, Tomer Bucher, Kobi Cohen, Ori Reinhardt, Guy Bartal, and Ido Kaminer. Tunable photon-induced spatial modulation of free electrons. *Nat. Mater.*, 22(3):345–352, 2023.

[235] Sophia Lloyd, Mohamed Babiker, and Jun Yuan. Quantized orbital angular momentum transfer and magnetic dichroism in the interaction of electron vortices with matter. *Phys. Rev. Lett.*, 108(7):074802, 2012.

[236] Wei Cai, Ori Reinhardt, Ido Kaminer, and F J García de Abajo. Efficient orbital angular momentum transfer between plasmons and free electrons. *Phys. Rev. B*, 98(4):045424, 2018.

[237] KH Michel and B Verberck. Theory of elastic and piezoelectric effects in two-dimensional hexagonal boron nitride. *Phys. Rev. B*, 80(22):224301, 2009.

[238] Supplemental Material includes a description of the employed harmonic crystal hBN and graphene phonon models, derivations of main equations, spatial maps of PAM-resolved EELS, and pseudoangular momentum considerations.

[239] K Y Bliokh, I P Ivanov, G Guzzinati, L Clark, R Van Boxem, A Béché, R Juchtmans, M A Alonso, P Schattschneider, F Nori, and J Verbeeck. Theory and applications of free-electron vortex states. *Phys. Rep.*, 690:1–70, 2017.